EXPLORING EXOTIC SUPERCONDUCTING ORDER IN LA-BASED CUPRATE MATERIALS USING JOSEPHSON INTERFEROMETRY

BY

DAVID ROBERT HAMILTON

DISSERTATION

Submitted in partial fulfillment of the requirements
for the degree of Doctor of Philosophy in Physics
in the Graduate College of the
University of Illinois at Urbana-Champaign, 2019

Urbana, Illinois

Doctoral Committee:

Professor Nadya Mason, Chair
Professor Dale Van Harlingen, Director of Research
Professor Eduardo Fradkin
Assistant Professor Jeffrey Filippini

Abstract

Josephson junctions are especially useful devices for studying exotic superconducting materials, because the transmission of superconductivity through a junction depends on the difference in phase of the superconducting order parameter across the junction. We present the results of two measurements which involve the fabrication of Josephson junctions on unconventional high-temperature superconductors to study the physical processes which govern novel superconducting states within these materials. The first experiment involves measuring the current-phase relation (CPR) of $La_{2-x}Ba_xCuO_4$ (LBCO)-Au-Nb Josephson junctions. Using two independent measurement methods, we observe a clear $\sin(2\phi)$ component of the CPR, a signature of pair-density wave (PDW) order. This component is strongest at x=0.125 doping, where PDW order is believed to be strongest, and increases in magnitude with temperature as conventional superconductivity is suppressed. Likewise, at x=0.155 doping, where PDW order is not expected to dominate, the CPR primarily contains the conventional $\sin(\phi)$ term. Together, these results provide strong support to the prediction that charge, spin and superconducting order intertwine to form a pair-density wave state in LBCO near x=1/8 doping. In the second experiment, we perform Josephson interferometry measurements of the superconducting order parameter of $La_{2x}Sr_xCuO_4$ (LSCO) in the heavily overdoped (x>0.25) regime. Combining experimental measurements and simulations of $I_c(\Phi)$, we find evidence for granular superconductivity and circulating currents in LSCO near criticality.

To Christine.

Acknowledgments

I am grateful to many different people for the help, community, and friendship they have shared with me during the completion of this thesis work. I would first like to thank my wife Christine for her constant support and companionship over the last six years. I am also thankful to my family, especially my parents Dan and Rochelle, for their unwavering encouragement and assistance. I regret that I never had that chance to meet my great uncle Arthur Paskin, who researched superconductivity at Brookhaven Labs. I imagine that we could have had many interesting discussions.

I would like to acknowledge my advisor, Dale, for his guidance, insight and inspiration throughout my graduate studies. I owe a lot to the DVH group for teaching me everything I needed to know about experimental methods, fabrication and cryogenics. Chris English was the first to take me under his wing, and Juan would later train me on many of the crystal fabrication and measurement techniques used in this thesis. Adam Weis' expertise on cuprate materials was often helpful, and Erik trained me on the ^{3}He system which was used for many of my measurements. I am also grateful to Can, Gilbert, Guang, Kenny, Jessica, and Tony for many useful discussions, and making the lab a supportive envionment in general. I have only known Faren a short time, but I thank her for her enthusiasm and initiative with regards to continuing the work on LSCO. These experiments could not have been done without our sample growers, led by Genda Gu, Masaki Fujita and Greg MacDougall. I also appreciate the advice I received from Lance Cooper while navigating through the process of completing my degree. Additionally, I would like to thank my committee members: Nadya Mason, Eduardo Fradkin and Jeff Filippini, for taking the time to read and evaluate this thesis.

Outside of the lab, I have many more to thank for their friendship and kindness. I appreciate John, Liz, Zach, Peter, Raquel, Shantel, Vince and Mark White for always being willing to share their time with my wife and I after a long work week. The local FGC has additionally been a solid source for community and support for me during my last few years in Urbana, particularly Alex, Cory, Joe, Vanessa, Eben, and Adam. Jon, Huy and Matt were always excellent hosts whenever I made the trip back to San Diego. Lastly, I'm thankful to Kyle, William and Kyle Williams for including me in many fulfilling creative collaborations.

This work was supported in part by the NSF grant DMR1710437. I acknowledge the use of the device fabrication and materials characterization facilities of the Materials Research Laboratory at UIUC.

Table of Contents

List of Figures

List of Abbreviations

BCS	Bardeen, Cooper, Schrieffer
BSCCO	$Bi_2Sr_2Ca_{n-1}Cu_nO_{2n+4+x}$
CDW	Charge density wave
CPR	Current-phase relation
FFT	Fast Fourier Transform
G-L	Ginzburg-Landau
H_c	Critical field
I_c	Critical current
IV	Current-voltage
JJ	Josephson junction
LBCO	$La_{2-x}Ba_xCuO_4$
LDOS	Local Density of States
LESCO	$La_{2-x-y}Eu_ySr_xCuO_4$
LSCO	$La_{2x}Sr_xCuO_4$
LTT	Low temperature tetragonal
MPMS	Magnetic Property Measurement System
MRL	Frederick Seitz Materials Research Laboratory
OP	Order parameter
PDW	Pair-density wave
SDW	Spin density wave
SC	Superconducting
SQUID	Superconducting Quantum Interference Device
T_c	Critical temperature
VSM	Vibrating Sample Magnetometer
YBCO	$YBa_2Cu_3O_{7x}$

Chapter 1

Background

1.1 History of superconductivity, BCS and G-L theories

In 1908, Dutch physicist Heike Kamerlingh Onnes was the first to produce liquid helium, achieving temperatures colder than any other place on Earth at the time. [2, 3] Studying the physics of materials at these historically low temperatures, Onnes went on to discover that the electrical resistance of mercury goes to zero at T=4.2K. [1, 4] Since this initial experimental observation of superconductivity in Hg, a wide variety of materials have been observed to undergo a superconducting transition below some critical temperature (T_c). A material in a superconducting state will behave as a perfect conductor and, as as Meissner and Ochsenfeld discovered in 1933, will also behave as a perfect diamagnet. [5] In the presence of a sufficiently large field $H_c(T)$, superconductivity can be suppressed entirely in a material. As T approaches T_c, H_c approaches zero.

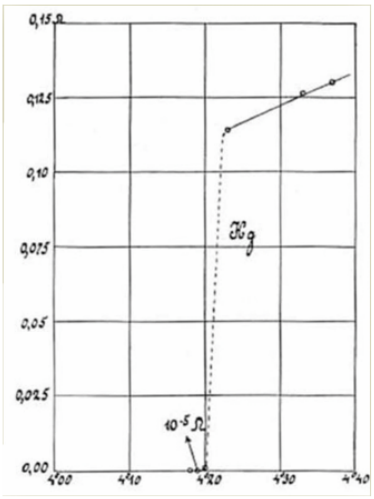

Figure 1.1: First observation of superconductivity. Resistance of Hg drops to zero at 4.2K. From [1]

A microscopic theoretical description of superconductivity would not come until Bardeen, Cooper and Schrieffer (BCS) published their theory of superconductivity in 1957 [6, 7]. The BCS theory builds on the proposal by Frölich that lattice vibrations lead to a net attractive interaction between electrons of similar energies in the lattice. [8]. Cooper in 1956 went on to show that in the presence of such a net attractive potential, it can be energetically favorable for pairs of electrons in a lattice to form a bound state, now known as a Cooper pair. [9] In BCS theory, the ground state wave function of a superconductor is constructed as a many-body state containing all possible configurations of paired states containing electrons with opposite spin and momentum, **k↑, -k↓**. BCS theory predicts that the density of states near the fermi level has an energy gap Δ, such that an energy of 2Δ is required to break a Cooper pair. In this model

the gap is temperature dependent, and vanishes entirely at T_c. As Cooper pairs propagate through a lattice, scattering excitations which are small compared to the gap energy become forbidden, preventing the onset of electrical resistance. Calculations using BCS theory have also accurately reproduced other observed phenomena related to superconductivity, such as the temperature dependence of specific heat and penetration depth.

The BCS ground state is a coherent state, in which all Cooper pairs in the material condense to the same quantum state with a well-defined phase ϕ. This is well aligned with the earlier theory of Ginzburg and Landau (GL), which represented the onset of superconductivity as a second-order phase transition with a complex order parameter $\psi(\mathbf{r}) = |\psi(\mathbf{r})|e^{i\phi}$, a complex pseudo-wave function. [10] $|\psi(\mathbf{r})|^2 = n_s(\mathbf{r})$ represents the number density of superconducting electrons in the system. In the context of the BCS model, $n_s(\mathbf{r}) = 2n_c(\mathbf{r})$, where $n_c(\mathbf{r})$ is the number density of Cooper pairs in the system. The G-L equations depend on two characteristic length scales: the coherence length ξ, which represents the scale of spatial variations of the order parameter, and the penetration depth λ, which determines the distance a magnetic field can penetrate into a superconductor. [11]

After BCS theory was published, Gor'kov showed that G-L theory, a phenomenological model, was in fact a limiting case of BCS theory at temperatures near T_c under certain conditions. [12, 13] Additionally, $|\psi(\mathbf{r})|$ was found to be proportional to the gap parameter $\Delta(\mathbf{r})$. While BCS theory applies to systems in which Δ is spatially homogeneous, such as many pure metals, G-L theory can be used to model the behavior of non-uniform superconducting materials, such as metallic alloys or ceramic oxides. The former class of materials are referred to as type-I superconductors, and the latter as type-II. $\lambda << \xi$ for a typical type-I superconductor, while the opposite is true for type-II.

1.2 Type-II Superconductors and High T_c materials

While type-I superconductivity will completely screen out external fields until it is destroyed by a critical field H_c, type-II superconductivity at intermediate fields ($T > H_{c1}$) will form a mixed state, where some flux penetrates the superconductor in the form of vortices carrying a single flux quantum, $\Phi_0 = hc/2e$, yet superconductivity persists elsewhere in the material. [14] Abrikosov explained this in terms of G-L theory by noting that when the surface energy at the superconductor-normal interface is negative, it become energetically favorable for these vortex filaments to form. Hence, the sign of this surface energy differentiates type-I and type-II superconductors. At sufficiently high fields ($T>H_{c2}$), superconductivity is destroyed as in a type-I superconductor. In this regime, the vortices become numerous enough to fill most of the volume of

the superconductor, causing a transition to the normal state. Abrikosov's theory not only explained previous observations of type-II materials allowing nonzero field to penetrate in the superconducting state, but also predicted future experiments which would directly image vortices in these materials.[15, 16, 17]

Although type-I superconductivity has a theoretical maximum T_c of roughly 40K which can be derived from properties of the electron-phonon interaction, superconducting transitions in type-II superconductors have been observed at much higher temperatures. [18] The 1986 discovery of superconductivity at T=35K in $La_{2-x}Ba_xCuO_4$ (LBCO) spurred a wave of development of cuprate materials which superconduct at high temperature, such as the subsequent synthesis of $YBa_2Cu_3O_{7-x}$ (YBCO), with a T_c of 93K and $Bi_2Sr_2Ca_{n-1}Cu_nO_{2n+4+x}$ (BSCCO), with a T_c of up to 108K. [19, 20, 21] As of this writing, $HgBa_2Ca_2Cu_3O_8$ currently holds the record for the material with highest measured T_c at ambient pressure, while recent measurements of LaH_{10} at 170 GPa have yielded T_cs as high as 250K. [22, 23] Materials with a higher T_c naturally have a lower cooling requirement to reach a superconducting state, which translates to cheaper and less expensive cryogenic equipment. A yet-undiscovered room temperature superconductor could make technology that utilizes superconductivity far more practical for everyday use, such as lossless power transmission lines, superconducting magnets and motors, and Josephson junction-based devices such as qubits and SQUID magnetometers.

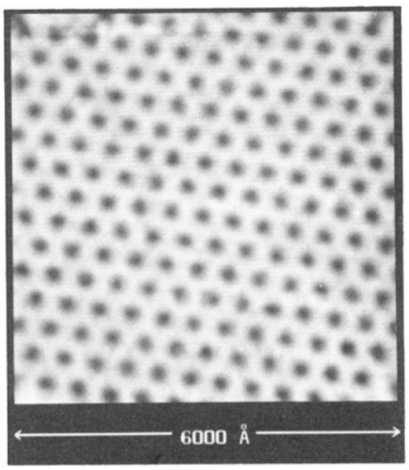

Figure 1.2: Imaged vortices in type-II superconductor NbSe2 obtained via STM experiments. From [15].

Despite the great interest in and the many applications of high-T_c materials, there is not yet a definitive theoretical model which describes the microscopic behavior of type-II superconductivity. Further characterizing the anomalous behavior of high temperature superconductors could help guide the synthesis of new materials with higher T_c. This thesis uses Josephson interferometry techniques to explore exotic superconducting states in high-T_c cuprate materials, specifically the pair-density wave state predicted to exist in LBCO at x=1/8 doping and disordered d-wave superconductivity in strongly overdoped $La_{2x}Sr_xCuO_4$ (LSCO).

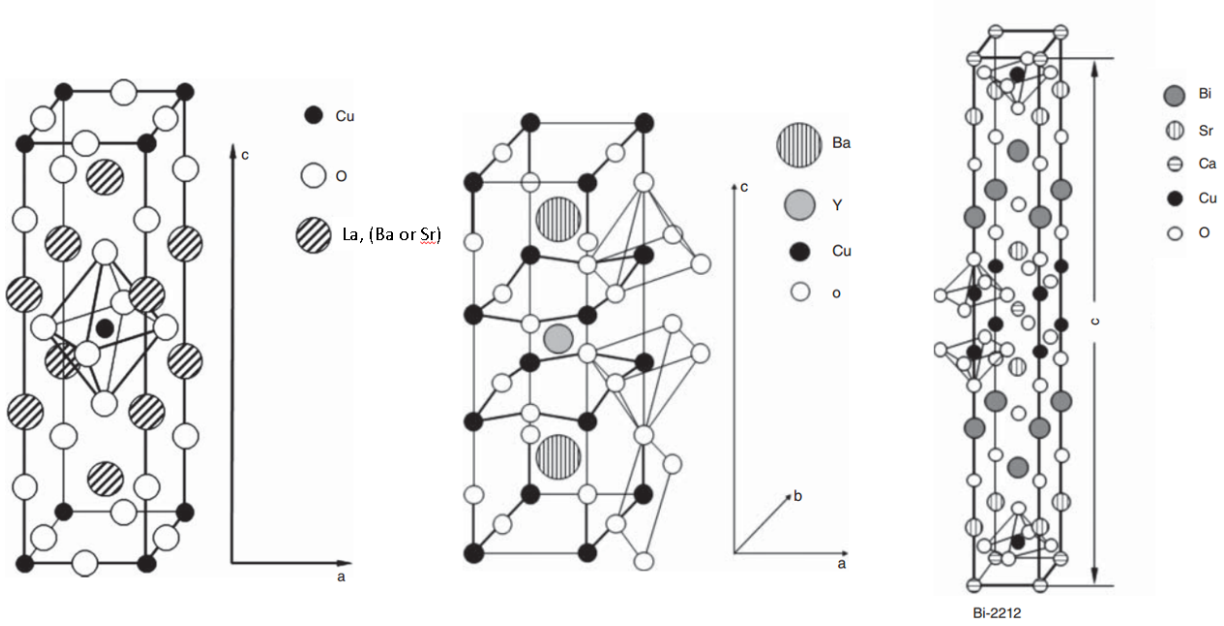

Figure 1.3: Left to right: crystal structure of tetragonal LBCO/LSCO, orthorhombic YBCO, and tetragonal BSCCO. From [24].

1.3 Normal State Properties and Phases of Cuprate Superconductors

The crystal structure of a typical cuprate superconductors is similar to that of a perovskite material. A cuprate unit cell consists of multiple square CuO_2 lattice planes, oriented along the crystal ab-plane, and separated by additional metal oxide layers containing other elements.[24] The physical and electronic properties of these materials depend strongly on doping, which can be controlled by substitution of elements in the lattice, or adjusting the oxygen content in the material. For example, partially replacing trivalent La with the divalent alkaline earth Ba or Sr introduces charge carriers into the material via hole doping. [25]

1.3.1 Mott Insulator

In the absence of doping, a cuprate superconductor exhibits Mott insulator behavior, a phase in which a material becomes electrically insulating and gains antiferromagnetic order despite having a band structure consistent with a metal. [28] In this regime, the repulsive energy U between electrons or holes is much greater than the hopping energy t, which allows carriers to travel between sites. For instance, in $LaCuO_2$, there is a single hole in the d shell per unit cell within each CuO_2 plane, and these holes repel each other strongly enough to inhibit conduction. Per the phase diagram in Fig. 1.4, in the hole doped cuprates, the

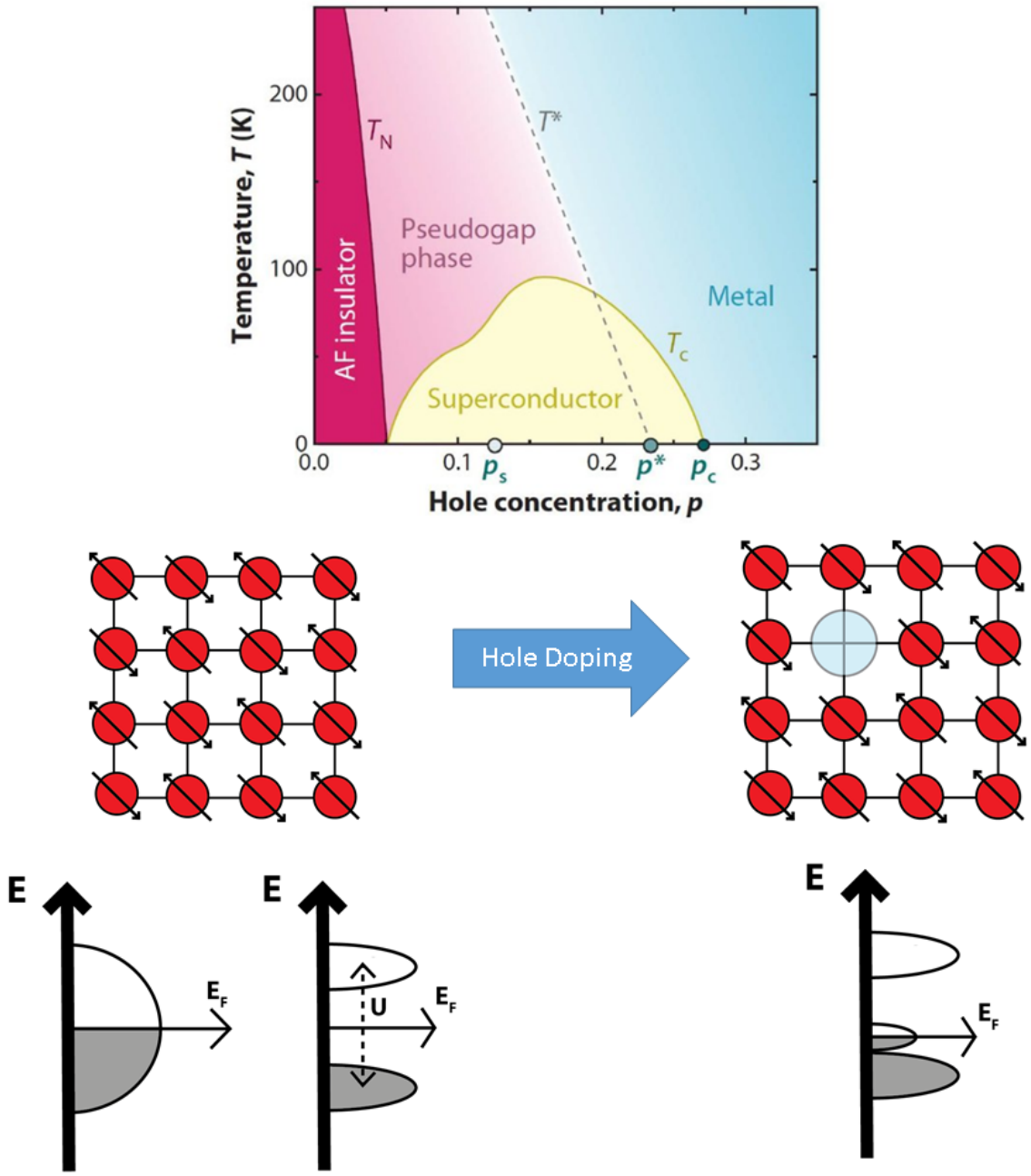

Figure 1.4: Top: Schematic phase diagram of a cuprate superconductor. As hole doping increases, the material transitions from an antiferromagnetic insulating (Mott) state into the pseudogap and superconducting regions. From [26] Mid left: Lattice representing a CuO_2 plane. Each site contains a single hole in the d-band. Bottom left: electron-electron repulsion (U) effectively splits the half filled d-band into two sub-bands, and the material behaves as an insulator. Mid right: the addition of holes into the lattice shifts E_F and creates additional allowed states close to the lower Hubbard band. With sufficient doping, the insulating behavior is suppressed.[27]

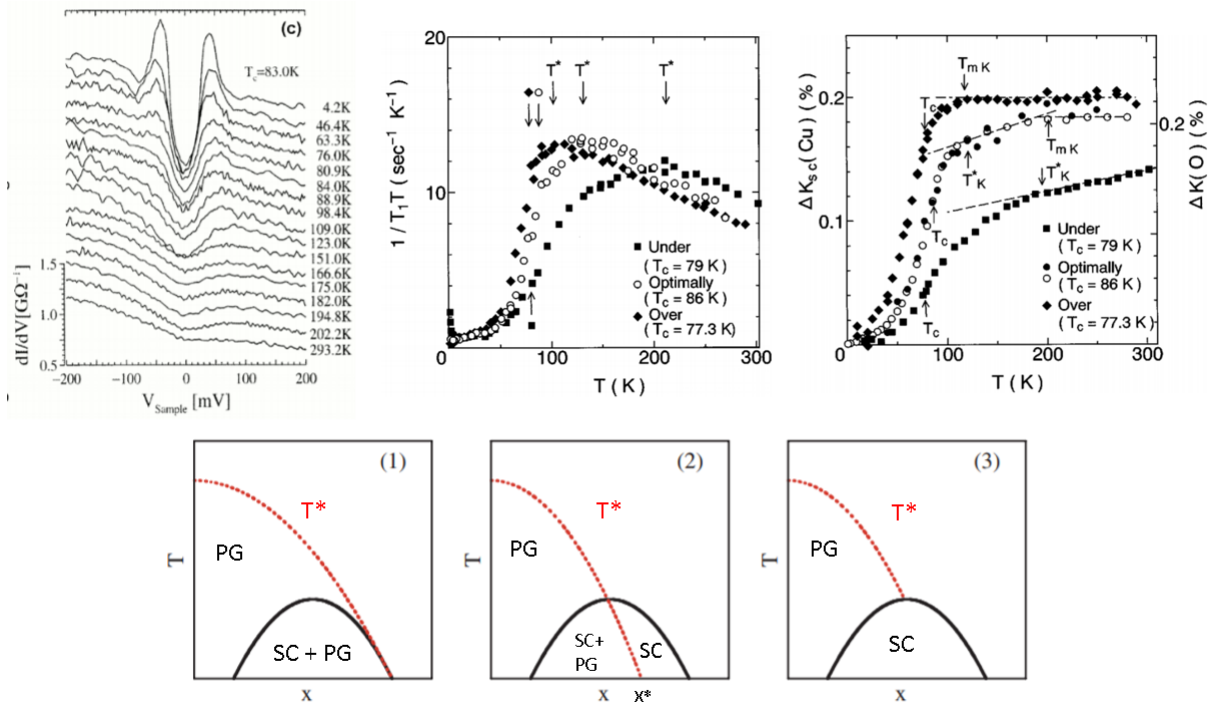

Figure 1.5: Top Left: Tunneling spectroscopy of BSCCO shows a gap feature which persists well above T_c. From [31]. Top mid: Peak in relaxation rate at T* is a signatures of pseudogap onset seen in NMR experiments on BSCCO. From [32]. Top right: T dependence of Knight shift, linked to the onset of spin singlet pairing. Also from [32]. Bottom: Three schematic phase diagrams of the pseudogap phase vs T, doping, adapted from [33]. (1): Phase diagram of the model which states the pseudogap and SC phase coexist over the entire SC dome. (2): Pseudogap coexists with SC up to a critical doping x*, a quantum critical point. (3): Pseudogap terminates at T_c, and does not coexist with SC.

Néel temperature T_N of the antiferromagnetic insulating phase drops sharply with doping, and is suppressed entirely at dopings as small as x=0.02. In the electron doped regime, the Mott insulator state can persist at dopings as large as x=0.15. One explanation for this asymmetry comes from considering second- and third-neighbor hopping terms in the t-J model, which have different signs for electron and hole doping.[29, 30] In this thesis, we will primarily concern ourselves with phenomena in the hole doping regime.

1.3.2 The Pseudogap

At temperatures below T* in the underdoped regime, a cuprate enters the pseudogap phase, in which the density of states becomes partially suppressed at the Fermi level.[33] However, the onset of the pseudogap generally occurs at a temperature T* higher than T_c, and this gap exists independently of a superconducting state. This behavior can be seen clearly in scanning tunneling spectroscopy measurements, in which the density of states at zero bias remains depleted well above T_c, the gap amplitude gradually decreasing

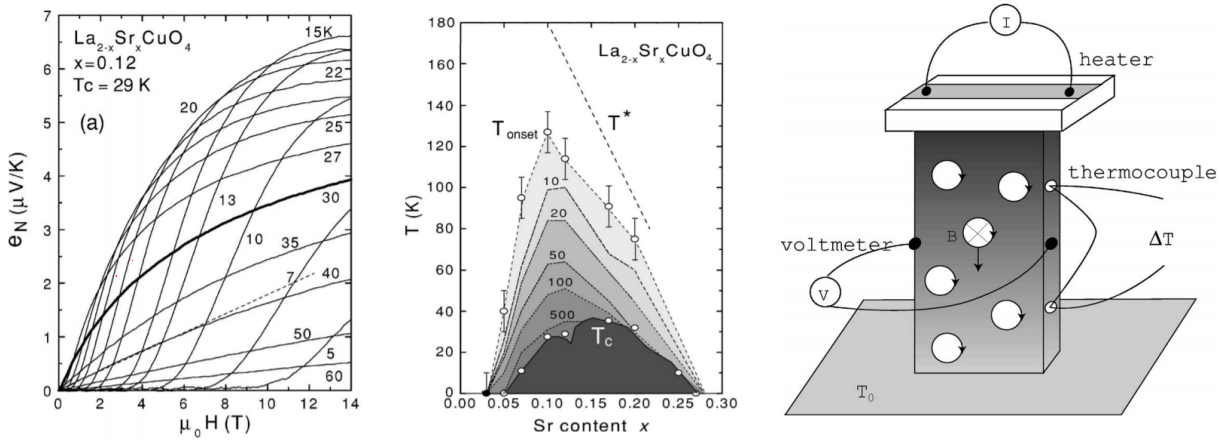

Figure 1.6: Left: Vortex-like excitations appear at lower fields at higher T. Past T_c, the signature of vortex motion becomes gradually weaker. Mid: Phase diagram of Nernst effect. Right: Setup of Nernst effect measurement. From [36].

with temperature. [31] Likewise, nuclear magnetic resonance measurements of BSCCO identified a doping dependent peak in normalized relaxation rate at T*, similar to the peak in relaxation rate near T_c in superconducting materials due to the BCS energy gap. [32, 34]

In addition to the gap feature, there is also evidence for the existence of pairing in the pseudogap region. A decrease in the Knight shift was observed at at a T^*_K that depends on doping, which can be compared to the change in Knight shift of a BCS superconductor near T_c which occurs as electrons condense into Cooper pairs and enter a spin-singlet state with no net spin. [32, 35]. This transition takes place continuously through T_c, implying that the pseuodgap could be a precursor to superconductivity, in which pairs begin to pre-form at T^*_K and enter a coherent superconducting state at T_c.[33] However, it is still an open question whether the pseudogap is merely a precursor to superconductivity which terminates at T_c or a distinct phase which coexists or competes with superconductivity below T_c over part of the phase diagram.

The pseudogap is also home to vortex-like excitations above T_c, as shown by Nernst effect experiments. [36] This measurement involves the application of a thermal gradient to a crystal of a high-T_c material. If vortices are present, this thermal gradient causes a net flow of vortices from hot to cold regions, producing a voltage across the crystal. The Nernst signal, linked to the motion of vortices, is detectable above a T-dependent field at temperatures below T_c. As reflected in the phase diagram in Fig. 1.6, the Nernst signal appears to drop continuously with T, until disappearing at a doping-dependent T_{onset}. However, this onset temperature appears below T*, and follows more closely the shape of the superconducting dome than the pseudogap transition.

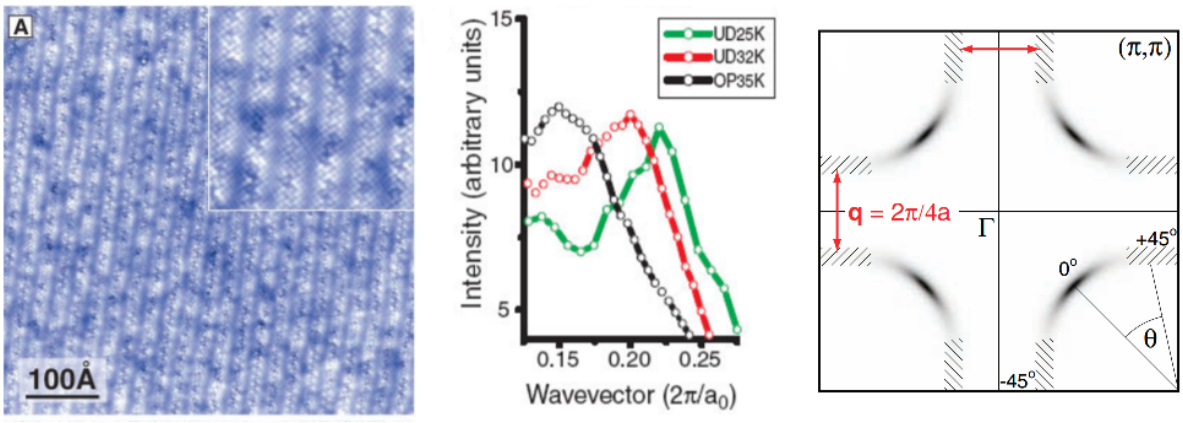

Figure 1.7: Left: LDOS modulations in BSCCO from [37] show the onset of charge stripes. Mid: As hole doping is reduced, the stripe wave vector of charge order in BSCCO is enhanced. From [38]. Right: Fermi surfce of $Ca_{2-x}Na_xCuO_2Cl_2$ shows nested regions with a nesting wave vector $|q| = 2\pi/4a_0$. This can generate CDW order. From [39].

1.3.3 Charge ordering

Charge and spin ordering are especially notable phenomena in high T_c cuprate materials, which take place within both the pseudogap and superconducting regimes. Charge order was first detected through local density of states (LDOS) measurements performed via scanneling tunneling microscopy, which revealed modulations in the LDOS oriented along copper-oxide bond directions which had 4-unit cell periodicity. [37] Later studies showed that the periodicity of these modulations increased with hole density, consistent with a charge-density wave (CDW) generated by fermi surface nesting. [38] Such nesting had previously been observed in ARPES measurements of underdoped cuprate materials both above and below T_c. [39]

There is significant interest in the question of whether the CDW state is a competing order with superconductivity, because these phases both use the same conduction electrons. In [40], X-ray diffraction of YBCO appears to show that the strength of CDW appears to decrease below T_c, but remains more robust in the application of a field, which suppresses superconductivity. In contrast, Hall effect measurements in [41] trace the onset of CDW and SC order versus pressure in YBCO at a doping where a local minimum in the superconducting dome that coincides with a maximum in the CDW transition temperature. Here, as pressure is increased, T_c increases markedly while CDW order is suppressed only slightly, which complicates the picture that SC is suppressed by CDW at this doping. In materials such as LBCO, CDW order is believed to intertwine with superconductivity and magnetic order to produce anomalous physics, which we will describe in greater detail in section 1.4.3.

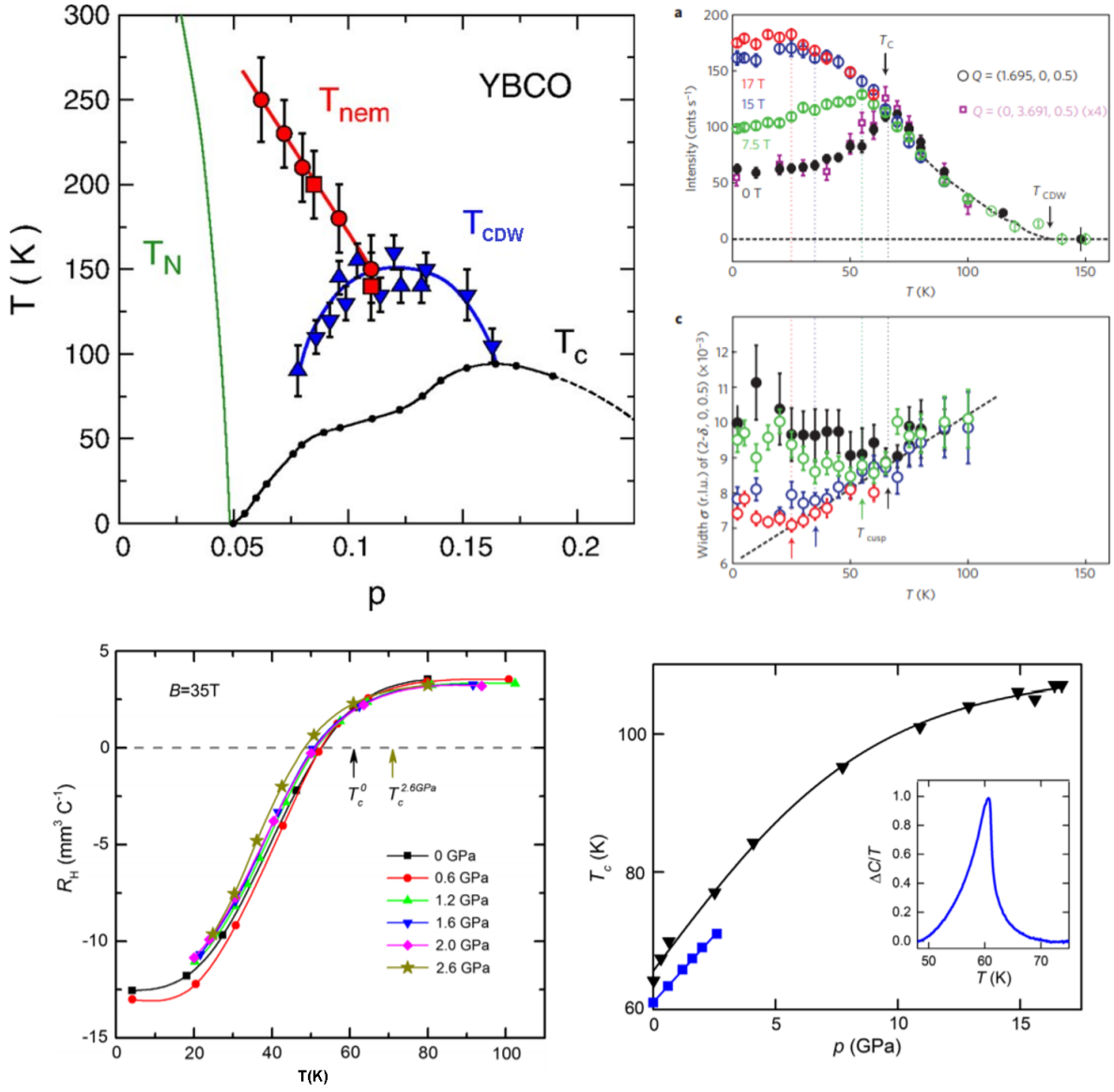

Figure 1.8: Top left: Phase diagram of YBCO from [42] shows an onset of CDW which occurs as T_c is slightly suppressed. Top right: Evidence suggesting competing orders. CDW peak intensity weakens below T_c, but increasing field weakens SC, and counters the suppression of CDW order. [40]
Bottom: Evidence contradicting the competing orders picture. Increasing pressure does not strongly affect CDW order (left), but strongly enhances T_c (right). From [41].

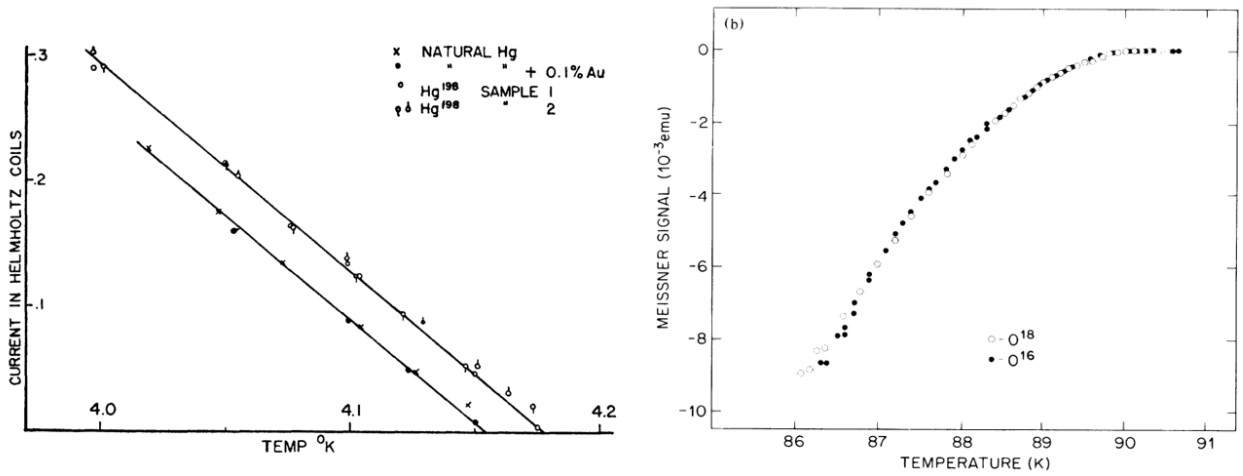

Figure 1.9: Left: Type-I superconductor Hg shows a clear difference in T_c between different isotopes. [43] Two different isotopes of YBCO appear to undergo a superconducting transition at the same temperature. [44]

1.4 Superconductivity in high-T_c cuprates

At sufficient hole doping (x$\gtrsim$0.05), a typical high-T_c cuprate material enters the superconducting state below a T_c which peaks at an optimal doping (x$\approx$0.15) and gradually declines to T_c=0 in the strongly overdoped (x$\gtrsim$0.3) region. This state has properties that contrast with the superconducting state in conventional BCS superconductors in a number of ways. For instance, the superconducting coherence length and magnetic penetration depth are anisotropic in cuprate superconductors between the in-plane (ab) and out-of-plane (c-axis) directions, such that $\xi_{ab} > \xi_c$ and $\lambda_{ab} < \lambda c$. [45] This indicates that superconductivity within the cuprates takes place primarily within the CuO_2 planes. Inter-plane transport is typically thought to be incoherent and mediated by Josephson coupling.

Further, in a type-I superconductor the transition temperature is sensitive to the atomic mass: pure ^{198}Hg has a T_c of 4.177K, while natural Hg with an atomic weight of 200.6 has a T_c of 4.156K. [43] BCS theory explains this result in terms of properties of phonons: the Debye frequency of phonons in a lattice is sensitive to the atomic mass of lattice ions, which in turn affects the phonon-mediated coupling that forms Cooper pairs. However, the isotope effect has been found to have only a small, doping-dependent effect on T_c of the cuprates, which further motivates seeking mechanisms other than electron-phonon coupling to explain high-temperature superconductivity. [44, 46]

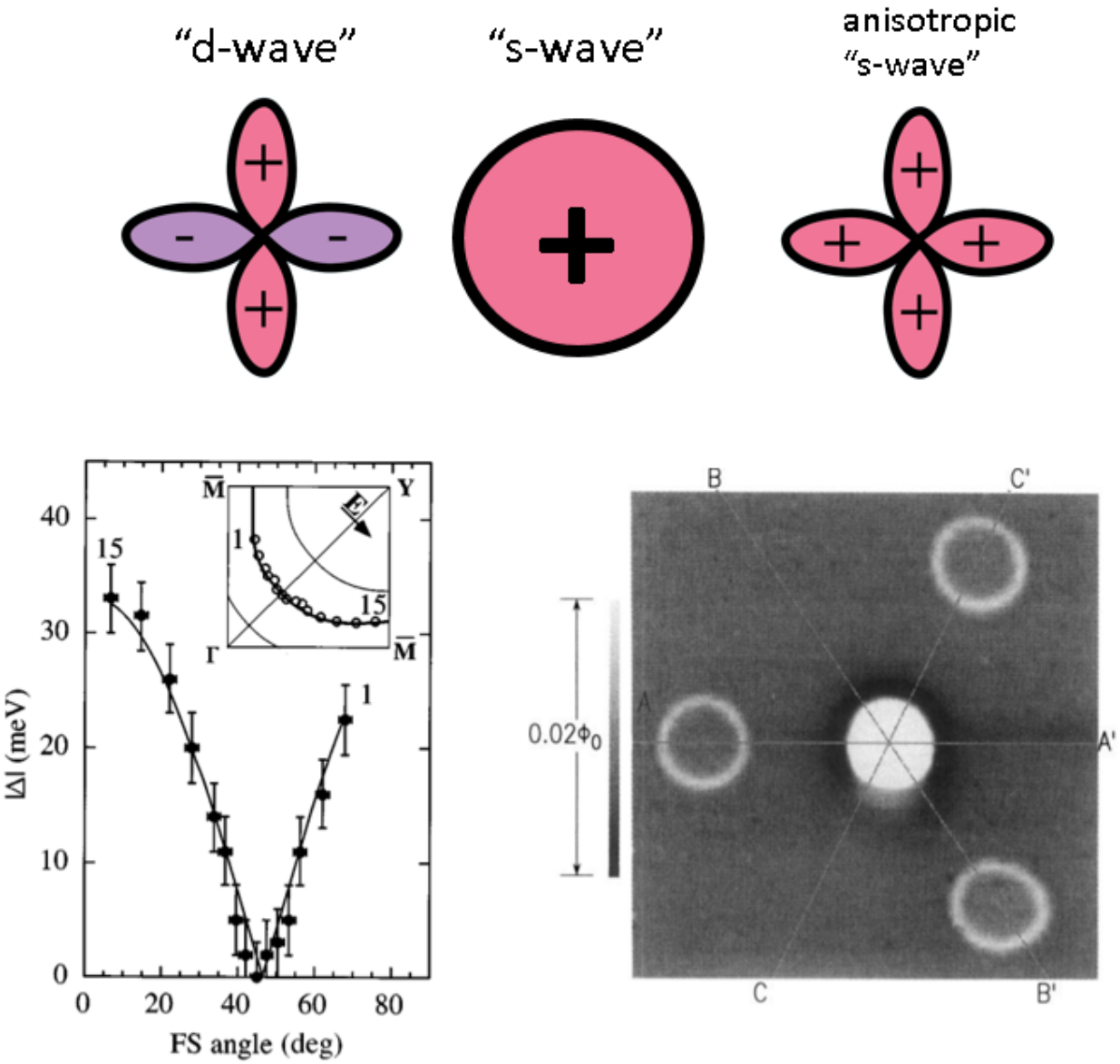

Figure 1.10: Top left: $d_{x^2-y^2}$ pairing has nodes in the energy gap along the (110) directions and a sign change in the order parameter between lobes. Top mid: s-wave pairing, typical of type-I superconductivity, has an isotropic energy gap. Top-right: Anisotropic s-wave pairing maintains a uniform sign of the order parameter, but allows for suppression of the magnitude of the order parameter along nodal directions. Bottom left: ARPES measurements [47] of BSCCO show a node in the superconducting energy gap, but lack phase information to differentiate d-wave from anisotropic s-wave pairing. Bottom right: A spontaneous flux is generated in a YBCO ring containing 3 grain boundary junctions, and not in rings containing 0 or 2 junctions. This indicates that these grain boundary junctions carry a π phase shift, a consequence of d-wave pairing symmetry in YBCO. [48]

1.4.1 d-wave Pairing Symmetry

One of the most distinguishing features of superconductivity in high-T_c cuprate materials is its pairing state, which is believed to have $d_{x^2-y^2}$ symmetry. Compared to the isotropic s-wave energy gap Δ of a BCS superconductor, the energy gap $\Delta(\mathbf{k})$ of a d-wave supercondcutor varies in reciprocal space following the functional form $\Delta(\mathbf{k}) = cos(k_x a) - cos(k_y a)$. [49] This energy gap has nodes along the (110) directions, and corresponds to a change in sign of the G-L order parameter between the k_x and k_y directions. ARPES measurements of cuprate materials have observed nodes in the energy gap consistent with this picture, but this measurement is not sensitive to to the phase of the order parameter. [47]

In order to differentiate d-wave pairing symmetry from anisotropic s-wave pairing, a phase-sensitive probe of the order parameter symmetry is required. Examples of such phase-sensitive measurements include Josephson interferometry, which will be discussed in the next chapter, and the tri-crystal experiment performed in [48]. In this experiment, four YBCO rings are deposited on the grain boundaries of a tricrystal $SrTiO_3$ substrate, such that one ring at the center contains three grain boundary Josephson junctions, and the other three rings contain two or zero such junctions. Assuming d-wave pairing symmetry within each grain, the junction critical current I_c across a grain boundary will depend on the crystallographic axis angles θ_i θ_j of the two grains such that $I_c \propto cos(2\theta_i)cos(2\theta_j)$. With the correct choice of angle, a π phase difference can be generated. If a superconducting ring contains an odd number of regions shifted by π, a spontaneous current will flow through the ring, which can in turn produce a spontaneous magnetization equal to half a flux quantum. [50, 51] If YBCO instead had s-wave pairing symmetry, none of the junctions would have a negative critical current, and no spontaneous magnetization would be observed. In Fig. 1.10, scanning SQUID magnetometry measurements of the aforementioned YBCO rings from [48] show a spontaneous magnetization in the ring with an odd number of junctions and no such signal in the rings with an even number of junctions, consistent with d-wave pairing.

1.4.2 Disordered d-wave superconductor-to-metal transition

D-wave superconductivity has been observed over much of the phase diagram of the cuprates. However, in the strongly overdoped regime (x$\gtrsim$0.2) of a disordered d-wave superconductor, some models predict deviations from uniform $d_{x^2-y^2}$ symmetry. LSCO, for instance, is considered a material in which doping contributes strongly to disorder: Sr dopants appear in random positions only 2.4Å away from the CuO_2 lattice. [53] In the vicinity of x=0.3 doping, the material experiences transitions from the superconducting state to a Fermi liquid-like normal state state.[54] Theoretical treatment of this transition in [52] considers superconductivity near criticality as consisting of spatially inhomogeneous "puddles" that can couple together via the Josephson

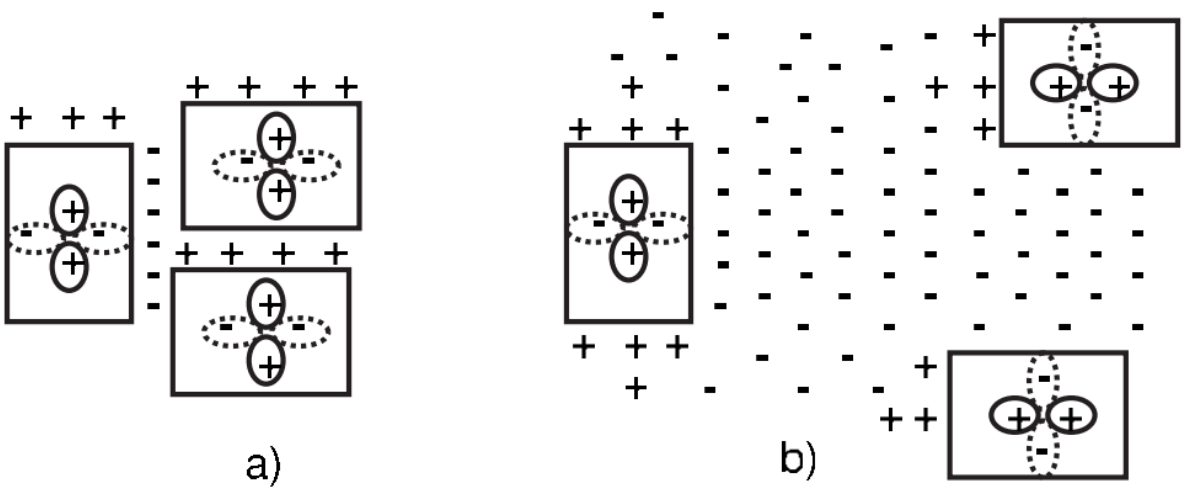

Figure 1.11: a) In the limit where puddles are closely spaced, SC is dominated by d-wave pairing. b) In the limit where puddles are dilute, an s-wave term dominates the Josephson coupling between puddles despite their local d-wave pairing symmetry. From [52]

effect. Locally, each puddle contains d-wave symmetry, with lobes aligned to either axis of the ab-plane. However, at the boundary of a puddle, a small but nonzero s-wave component is generated in the neighboring metal. The effective Josephson energy of this system has the form $E_J = \sum_{i \neq j}[\eta_i \eta_j \tilde{J^s_{ij}} + \tilde{J^d_{ij}}]cos(\phi_i - \phi_j)$, where $\eta_{i,j} = \pm 1$ introduces a sign change based on the relative orientations of the puddles, and $\tilde{J^{s,d}_{ij}}$ reflect the strength of the exchange interaction between s- and d-wave components of the order parameter of the puddles, which have a phase $\phi_{i,j}$. In the regime where the concentration of puddles is high, the pairing symmetry is dominated the d-wave term. However, $\tilde{J^s_{ij}}$ decays more slowly than $\tilde{J^d_{ij}}$ with puddle spacing, and as disorder strength increases with doping, the puddles become more dilute, causing the pairing to be dominated by the $\tilde{J^s_{ij}}$ term. As a result, this model predicts that disordered cuprate materials such as LSCO should appear to have globally s-wave symmetry in heavily overdoped parts of the phase diagram close to the d-wave superconductor to metal transition. We will investigate this problem using simulations and Josephson interferometry techniques in chapter 5.

1.4.3 Intertwined orders: striped superconductivity in LBCO

LBCO, the first discovered high-T_c superconductor, is still the subject of significant scientific interest due to the unique and exceptional phenomena it exhibits. In contrast to other cuprate materials, LBCO experiences a significant suppression of the bulk T_c at x=1/8 doping [56]. This doping corresponds with a strong onset of both charge and spin order. In contrast, in materials such as YBCO, antiferromagnetic spin order appears to compete with CDW order, and the two phases only seem to coexist over a small portion of the phase diagram.

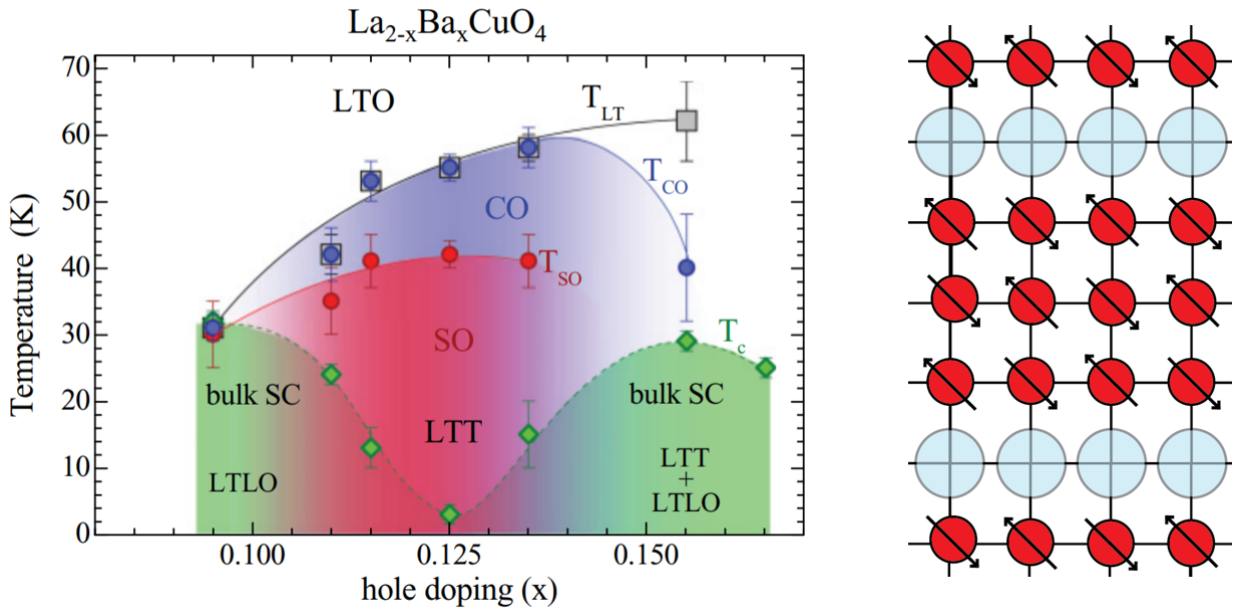

Figure 1.12: Left: Phase diagram of LBCO, from [55]. Hole doping affects onset of superconducting, charge and spin order, as well as crystal structure. Right: Schematic picture of stripe order. Hole-rich regions (blue) are arranged into charge stripes separated by hole-poor regions (red) with antiferromagnetic order.

The combination of charge and spin order as well low-temperature tetragonal (LTT) crystal structure leads to "stripe" order within LBCO.

In a stripe ordered state, hole rich regions line up to form 1D charge stripes in the copper oxide plane, which separate hole-poor, antiferromagnetically ordered stripes of copper spins. [60] The phase of each antiferromagnetic region changes by π across each hole stripe, doubling the periodicity of these regions. The first evidence for a striped phase in cuprate materials was found in neutron scattering experiments on $La_{2-x}Sr_xNi0_{4+\delta}$ in which simultaneous charge and spin order was detected, in addition to superlattice peaks which could be explained by the presence of periodic antiferromagnetic regions separated by charge stripes. [57, 61] Subsequent scattering studies have detected stripe order within the LTT phases of materials such as $La_{2-x-y}Eu_ySr_xCuO_4$ (LESCO) and LBCO.[62, 58] Compared to charge order in YBCO, stripe order in LBCO has a longer maximum correlation length, though it is strongly peaked about x=1/8 doping and falls off sharply at doping values away from this critical value. [59]

Although stripe order is most robust at the doping at which bulk SC order is weakest in LBCO, the stripe phase of LBCO appears to support 2D superconductivity and superconducting fluctuations well above the bulk T_c. In [63], transport and susceptibility measurements were carried out on LBCO crystals at x=1/8 doping with a bulk diamagnetic transition at 4K. Resistance measurements showed that resistivity at zero field along the in-plane direction goes to zero at roughly 18K, while the out-of-plane resistivity remains finite

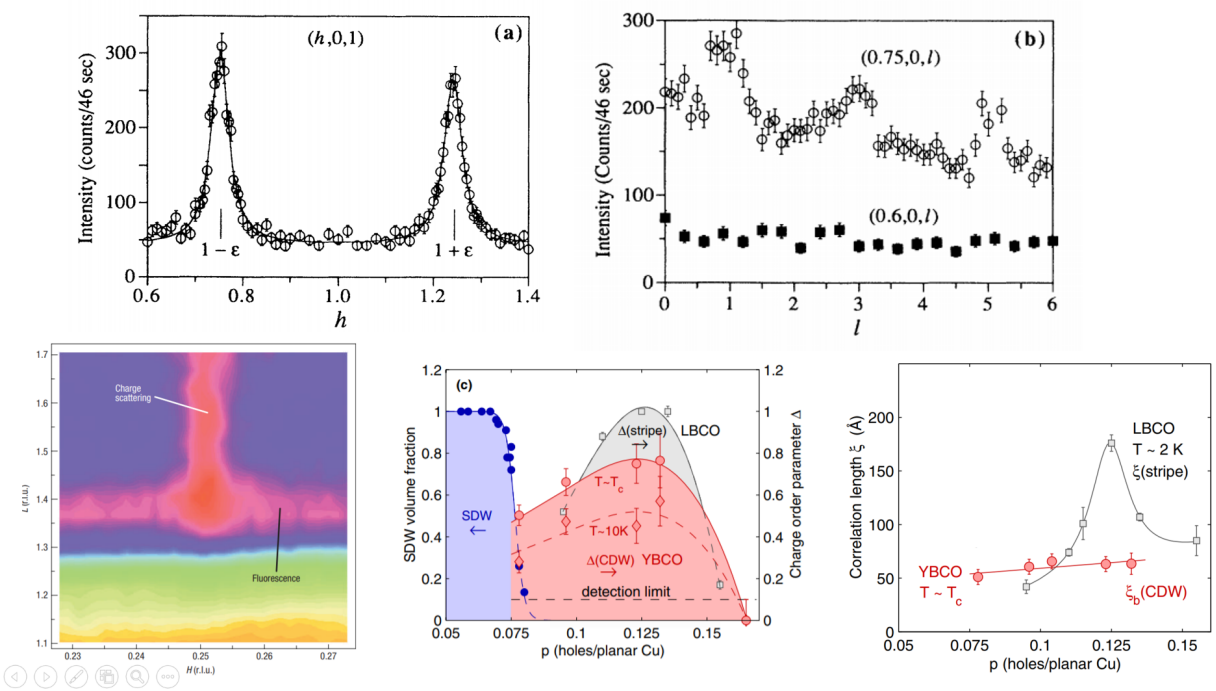

Figure 1.13: Top Left: Superlattice peaks obtained by neutron scattering of $La_2NiO_{4.125}$ [57] centered about (h,0,l) in reciprocal space, where h is odd and l an integer. The spacing of these peaks corresponds to 4-unit cell periodicity of the magnetic domains, and the peak width gives an in-plane correlation length of 40Å. Top right: also from [57], scan of 1-ϵ peak along the out of plane direction in reciprocal space, indicating interlayer correlations stronger at odd values of l. This implies a two-unit-cell periodicity of magnetic order in the out of plane direction. Bottom left: RSXS scattering of LBCO has a scattering peak in the out of plane direction displaced by 1/2 of a reciprocal lattice unit, indicating 2 unit cell periodicity of charge stripes between planes. The in-plane scattering peak at 1/4 of a reciprocal lattice unit similarly indicates 4-unit cell periodicity of in-plane charge stripes, and therefore 8-unit cell periodicity of spin stripes. Scattering is stronger in the out-of-plane direction, indicating weaker correlations between CuO_2 layers. Similarly, the in-plane correlation length, $\xi_a \approx 127$ unit cells, is much larger than the in-plane ξ_c, which is only ≈ 2 unit cells. [58] Bottom mid: phase separation of CDW and SDW order in YBCO, compared to the region of coexistence in LBCO. From [59] Bottom right: Correlation length vs doping of CDW order in YBCO vs stripe order in LBCO [59].

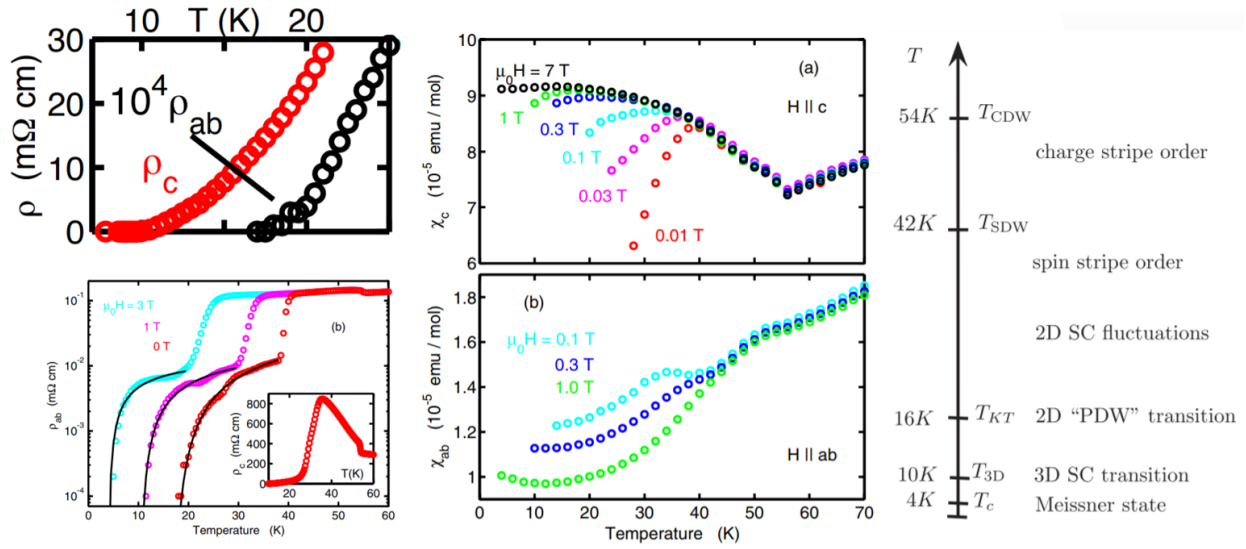

Figure 1.14: Left: resistivity along the c- and ab- directions of LBCO. Zero resistance state in the ab-direction occurs at T=18, while resistance is finite in the c-direction until T=10. Bottom left: drop in in-plane resistivity near T=40K corresponding to 2D superconducting fluctuations. Mid: Susceptibility measurements show an onset of weak diamagnetism in the direction perpendicular to these fluctuations (top), and not in the direction parallel to them (bottom). [63] Right: Summary of phase transitions in LBCO at low temperature. [64]

until it reaches 0 at 10K. Additionally, in the finite-resistance regime, ρ_{ab} begins to drop sharply at T≈40K. This has been interpreted as the onset of superconducting fluctuations, supported by the observation of weak diamagnetism in the c-direction measured at T≈28K via susceptibility. Further, above the bulk Meissner T_c, no such diamagnetism was observed in the direction parallel to these in-plane fluctuations. Hence, it would appear that superconducting correlations coexist with stripe order in LBCO over much of the stripe phase, but stripe order suppresses inter-plane coupling of superconductivity.

1.4.4 The Pair-Density Wave State

The anomalous behavior of superconductivity in the striped phase of LBCO is well described by pair-density wave (PDW) theory. In a system which follows the PDW model, the superconducting order parameter varies periodically with respect to position, and vanishes when averaged spatially over its center of mass position. [68] Additionally, the order parameter will have nonzero center of mass momentum $\mathbf{Q}$. In the case of a striped superconductor described by PDW theory, the superconducting order at each charge stripe is shifted in phase by π, and the arrangement of stripes at each successive CuO_2 layer is shifted by 90 degrees. [65, 69] This has the effect of completely cancelling Josephson coupling between a plane of stripes and its three nearest neighbors, which would explain the regime in which superconductivity persists in the in-plane direction, but

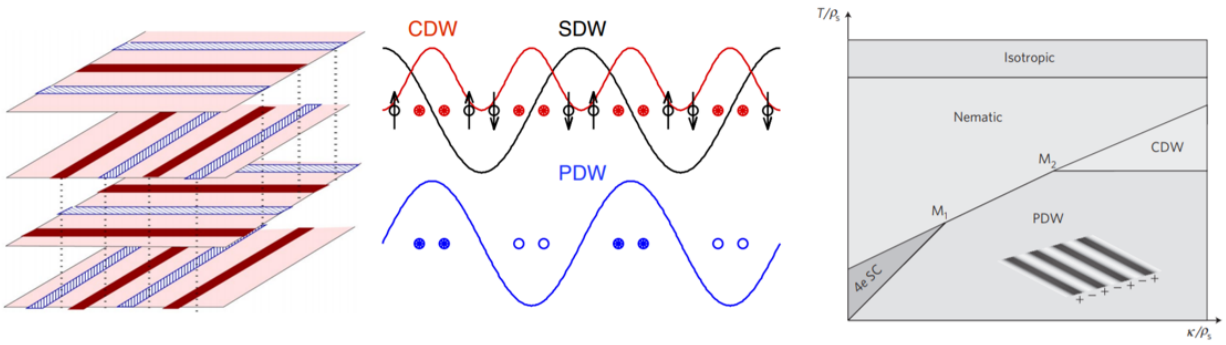

Figure 1.15: Left: Illustration of striped superconductivity in LBCO under PDW order. Adjacent charge stripes (blue, red lines) are shifted in phase by π, and charge stripes in adjacent CuO_2 planes are rotated by 90 degrees. This has the effect of cancelling Josephson coupling in the out-of-plane direction. [65] Mid: Comparison of charge, spin and PDW order. PDW order has the same periodicity as SDW order, but overlaps with sites of CDW order. Circles change from dark to light in the lower figure to indicate a phase shift of π in the superconducting order parameter. Figure from [66] Right: Theoretical phase diagram of the PDW state. At low temperatures where the CDW elastic constant κ is small compared to the superfluid stiffness ρ_s, a charge-4e superfluid condensate is predicted. [67]

is suppressed in the out-of-plane direction. Hence, this model explains the dynamical layer decoupling of LBCO as the result of the intertwining of CDW, SDW and superconducting orders to form the PDW state. This implies that charge, spin and superconducting correlations are coexisting and of similar strength in the PDW state, rather than competing orders in which one dominates as the others are suppressed. [64] PDW theory additionally predicts the onset of exotic phases such as a charge-4e superconducting condensate, which is expected to form upon thermal melting of a PDW state. [67]

Some experiments have found results suggestive of the existence of a PDW state. For instance, nonlinear tetrahertz spectroscopy of LBCO conducted in [70] identified a third harmonic in reflectivity which could be explained by spatial variations in phase predicted in PDW order. At $x = 0.095$ and $x = 0.155$, this signal does not persist beyond $T_c \approx 33K$. At $x = 0.115$ doping, the 3rd harmonic continues well past T_c=13K until it falls off at the charge order transition T=55K. Additionally, in [71], scanning Josephson tunneling on BSCCO appeared to find a modulating density of Cooper pairs with a well defined momentum $\mathbf{Q}$.

Successfully detecting changes in phase by π of the superconducting order parameter between adjacent charge stripes would be significant evidence supporting the existence of a pair-density wave state in LBCO. We will describe Josephson junction experiments intended to accomplish this in the following chapters.

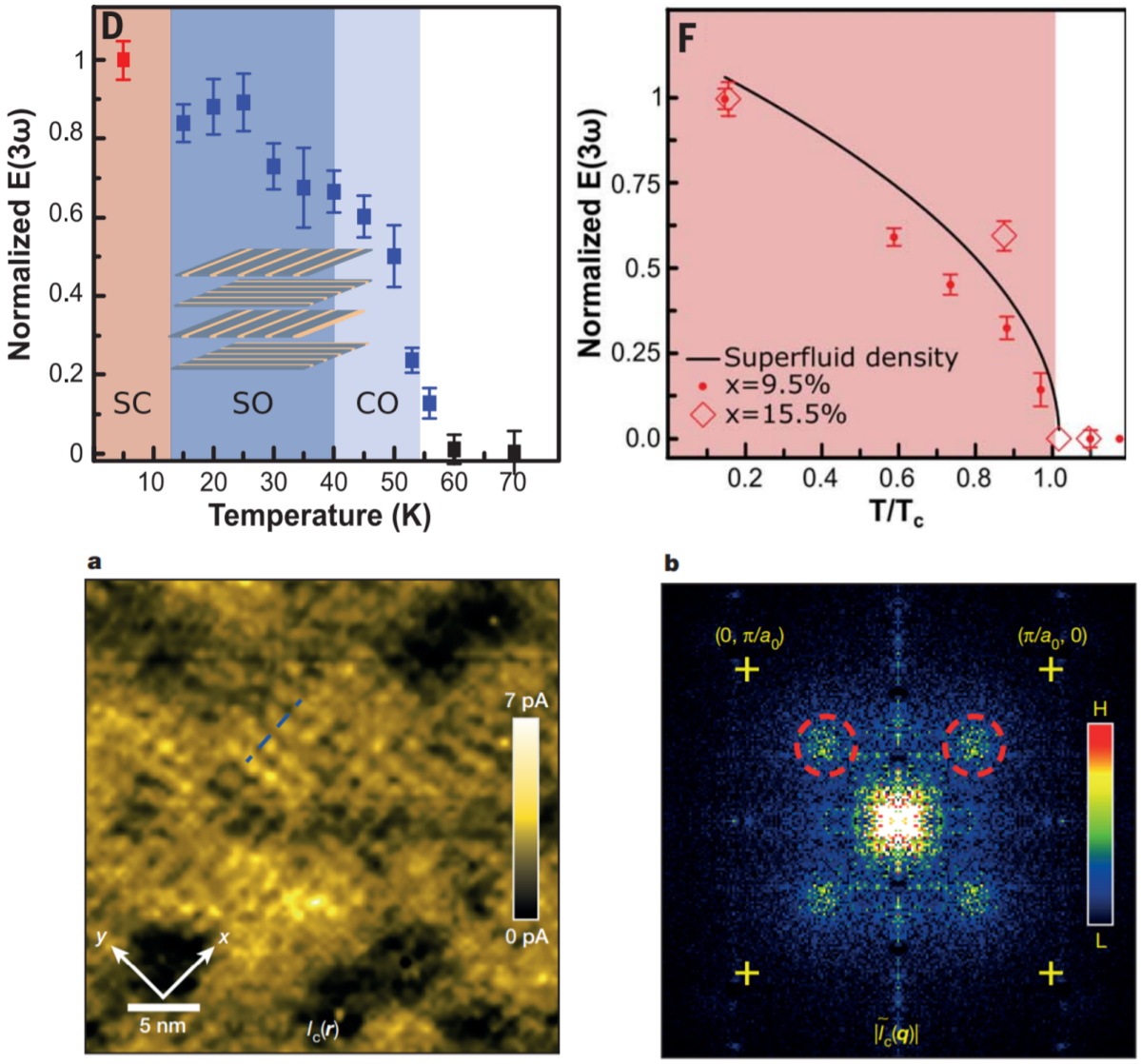

Figure 1.16: Top: Magnitude of reflectivity at ω=3ω_{pump} from [70] conneced with nonlinear Josephson tunneling in the PDW state. Close to $x = 1/8$ doping, this signal persists with T well past T_c until CO is suppressed. Further from 1/8 doping, the signal persists only until T_c. Bottom left: Modulations in cooper pair density in BSCCO obtained using scanned Josephson tunneling microscopy. [71] Bottom right: Fourier transform of these modulations indicate peaks at $\mathbf{Q}= (0.25 \pm 0.02, 0)2\pi/a_0$ and $\mathbf{Q}= (0, 0.25 \pm 0.02)2\pi/a_0$.

Chapter 2

Josephson Junctions and SQUIDs

2.1 The Josephson Effect

When two superconducting electrodes are separated by a weak link, it is possible for a supercurrent to flow between the two electrodes. This is known as the Josephson effect, first predicted by B.D. Josephson in 1962. [72] While Josepshon's calculations involved quantum tunneling of paired electrons through an insulating barrier, the Josephson effect has also been observed to take place in junctions containing other types of weak links, such as a normal metals or constricted superconductors.

To illustrate how the Josephson effect arises from G-L theory, consider two superconductors contacting the left and right sides of a normal metal material with coherence length $\xi_N \ll$ L, spanning from $x = 0$ to $x = L$, and where the phases of the order parameter of the superconducting regions are ϕ_L and ϕ_R, respectively. An exponentially decaying portion of the order parameter will penetrate into the normal region from each side on the scale of the coherence length ξ_N, such that the order parameter in the normal region can be approximated [73] as

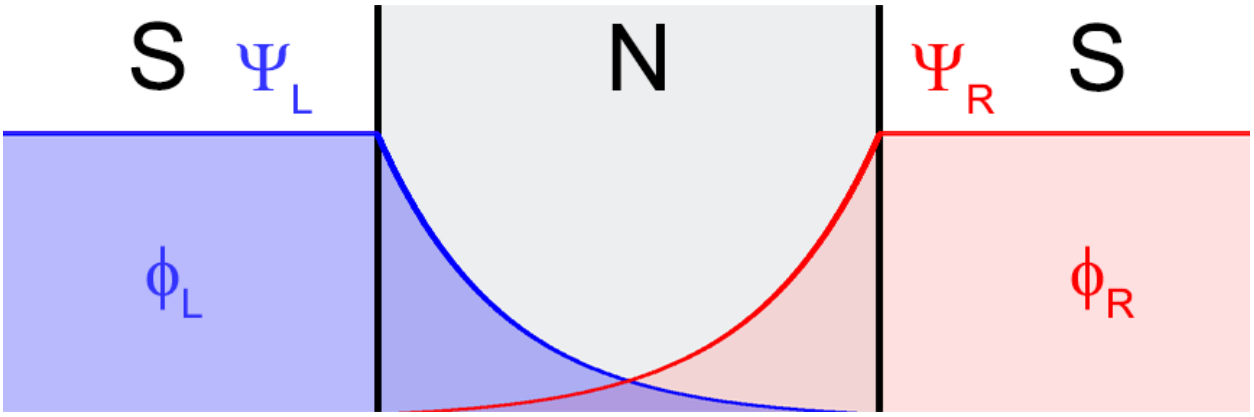

Figure 2.1: Diagram of a Josephson junction. The order parameter of the two superconducting regions penetrate into the weak link from either side, allowing a supercurrent to pass through the junction.

$$\Psi(x) = |\Psi_L(0)|e^{-x/\xi_N} + |\Psi_R(L)|e^{-(L-x)/\xi_N}e^{i\Delta\phi} \tag{2.1}$$

where $\Delta\phi = \phi_R - \phi_L$. In the absence of field, the magnitude of the supercurrent density j_s can be expressed as

$$j_s = \frac{e^*\hbar}{2m^*i}(\Psi^*\nabla\Psi - \Psi\nabla\Psi^*) = \frac{e^*\hbar}{\xi_N m^*}|\Psi_L(0)||\Psi_R(L)|e^{-L/\xi_N}sin(\Delta\phi) = j_0 sin(\Delta\phi) \tag{2.2}$$

where $j_0 = \frac{e^*\hbar}{\xi_N m^*}|\Psi_L(0)||\Psi_R(L)|e^{-L/\xi_N}$ depends on physical constants, material properties and junction length.

Integrating j_s over the junction dimensions, we obtain the functional form of the dc Josephson effect,

$$I_s = I_c sin(\Delta\phi) \tag{2.3}$$

which indicates that when two superconductors lie across a weak link with a difference in phase $\Delta\phi$ of the superconducting order parameter across the barrier, a zero-voltage dissipationless current I_s is generated.

Josephson further predicted if a voltage V were maintained across a junction, the phase difference would evolve as

$$d(\Delta\phi)/dt = 2eV/\hbar. \tag{2.4}$$

This is known as the ac Josephson effect. Taking 2.3 and 2.4 together, we can obtain the free energy stored in the junction:

$$F = \int I_s V dt = \hbar I_c/2e \int sin(\Delta\phi)d\phi = const. - E_J cos(\Delta\phi) \tag{2.5}$$

where $E_J \equiv \hbar I_c/2e$ is the Josephson energy. This energy is then minimized at $\Delta\phi = 2\pi n$, where n is an integer.

In order to determine the effect of a uniform external field $\mathbf{B}$, we may replace $\Delta\phi$ in the preceding equations with a gauge invariant phase

$$\phi \equiv \Delta\phi - \frac{2\pi}{\Phi_0}\int \mathbf{A}\cdot d\mathbf{s} \tag{2.6}$$

where $\Phi_0 \equiv h/(2e)$ is a flux quantum. [12] As a result, $\mathbf{B}$ causes the phase difference across the junction to vary spatially over the width w of the junction. Because $\mathbf{B} = \nabla\times\mathbf{A}$, $\int \mathbf{A}\cdot d\mathbf{s}$ is equivalent to a magnetic flux Φ. Setting the phase $\phi(0) = \phi_0$ at the edge of the junction, the phase at a distance y from the edge for

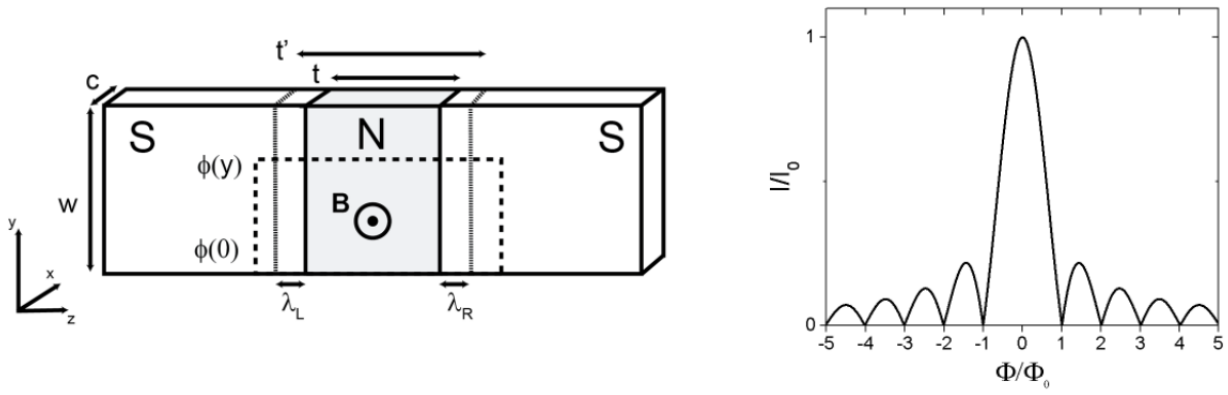

Figure 2.2: Left: diagram of a Josephson junction under the effect of a field. Dashed line shows the effect of the penetration depth, dotted rectangle indicates contour of integration. Right: Calculated I_c vs field of a Josephson junction.

a junction with thickness t should be

$$\phi(y) = \phi_0 + \frac{2\pi\Phi(y)}{\Phi_0} = \phi_0 + \frac{2\pi}{\Phi_0}B(t + \lambda_L + \lambda_R)y = \phi_0 + \frac{2\pi}{\Phi_0}Bt'y. \tag{2.7}$$

$\lambda_{L,R}$ correspond to the penetration depth of the superconductors on either side of the barrier. Using this phase dependence, we obtain the supercurrent across the junction with height c:

$$I_s(B) = c\int_0^w j_c sin(\phi_0 + \frac{2\pi}{\Phi_0}Bt'y)dy = I_0\frac{sin(\pi\Phi/\Phi_0)}{\pi\Phi/\Phi_0}sin(\phi_0) \tag{2.8}$$

where $\Phi = Bt'w$ is the flux through the junction and $I_0 = j_c wc$ is the critical current of the junction at zero field. To obtain the critical current as a function of field, we maximize the above equation with respect to ϕ_0 to obtain

$$I_c(\Phi) = max(I_s(\Phi), \phi_0) = I_0\left|\frac{sin(\pi\Phi/\Phi_0)}{\pi\Phi/\Phi_0}\right| \tag{2.9}$$

This result has a similar form to the Fraunhofer diffraction pattern observed in optics when light passes through a single slit.

2.2 The dc SQUID

For a superconducting analog of double-slit optical interference, we can consider a superconducting ring separated by two Josephson contacts, known as a SQUID (Superconducting Quantum Interface Device). In this configuration, the supercurrent through the ring has the form

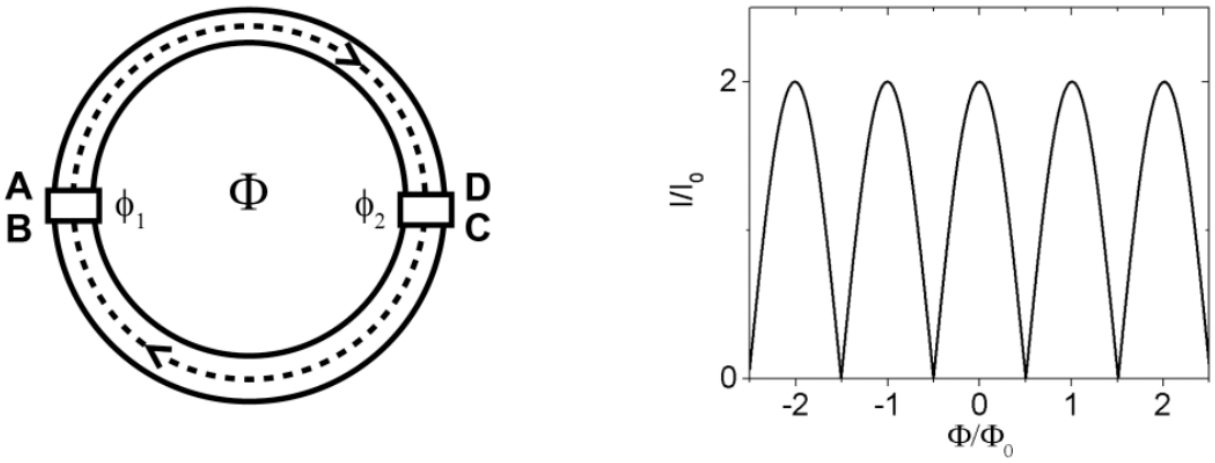

Figure 2.3: Left: diagram of a SQUID, which consists of two Josephson junctions along a superconducting ring. Dashed loop indicates integration path. Right: Calculated I_c vs field of a SQUID.

$$I_s = I_{c1} sin(\phi_1) + I_{c2} sin(\phi_2) \tag{2.10}$$

where ϕ_1 and ϕ_2 denote the phase difference across the junction with I_{c1} and I_{c2}, respectively. In order for the phase at any point on the ring to be singly valued, we will enforce the phase difference across a complete circuit of the ring must be an integer multiple of 2π. So for a complete circuit through both barriers and superconducting regions, we obtain

$$\oint \nabla\phi \cdot d\mathbf{l} = 2\pi n = \Delta\phi_{BA} - \frac{2\pi}{\Phi_0}\int_B^A \mathbf{A}\cdot d\mathbf{l} + 0 - \frac{2\pi}{\Phi_0}\int_A^D \mathbf{A}\cdot d\mathbf{l} + \Delta\phi_{DC} - \frac{2\pi}{\Phi_0}\int_D^C \mathbf{A}\cdot d\mathbf{l} + 0 - \frac{2\pi}{\Phi_0}\int_C^B \mathbf{A}\cdot d\mathbf{l} \tag{2.11}$$

Assuming the flux through the junction area is negligible compared to the flux through the loop, we can neglect $\int \mathbf{A}\cdot d\mathbf{l}$ through the junctions, equate $\phi_{AB,CD} = \phi_{1,2}$ and evaluate $\int \mathbf{A}\cdot d\mathbf{l}$ about the ring to obtain

$$\phi_2 - \phi_1 = \frac{2\pi\Phi}{\Phi_0} + 2\pi n \tag{2.12}$$

where n is an integer. Using this flux quantization condition, we can solve for the field dependence of the supercurrent through the SQUID. Setting $I_{c1} = I_{c2} = I_0$, this becomes

$$I_s(\Phi) = I_0 sin(\phi_1) + I_0 sin(\phi_1 + \frac{2\pi\Phi}{\Phi_0}) = 2I_0 cos(\frac{\pi\Phi}{\Phi_0}) sin(\phi_1 + \frac{\pi\Phi}{\Phi_0}) \tag{2.13}$$

Maximizing with respect to ϕ_1, we obtain the critical current of the SQUID as a function of applied flux,

$$I_c(\Phi) = 2I_0|cos(\frac{\pi\Phi}{\Phi_0})| \tag{2.14}$$

which indeed resembles an optical double-slit interference pattern. If an appropriate constant bias current is maintained through this device, and the device is resistively shunted to eliminate hysteresis, the measured voltage across the SQUID will vary periodically, with one period in voltage corresponding to one flux quantum, $\Phi_0 = h/2e \approx 2 * 10^{-15} Wb$. [74] As a result, SQUID magnetometers can make some of the most sensitive measurements of magnetic flux possible.

2.3 Measuring order parameter anisotropy using Josephson interferometry

Because superconducting transport through a Josephson junction is sensitive to the phase of the order parameter, devices based on Josephson junctions are a naturally useful system for studying superconductors with exotic order parameter symmetry. While equation 2.9 holds for a junction with constant supercurrent density j_c over the junction area, such as a junction between two s-wave superconductors, this assumption is invalidated if the phase of the order parameter of one or both superconductors is anisotropic over the junction area.

For example, suppose a junction is formed on the corner of a crystal of a superconducting material with $d_{x^2-y^2}$ pairing symmetry, such that half of the junction area lies along the (100) axis, and the other half along the (010) axis. As we discussedin section 1.4.1, for a crystal with d-wave pairing symmetry, the phase of the order parameter changes by π between the k_x and k_y directions. Integrating over the junction width, with y=0 defined as the corner position, the field dependence of the supercurrent becomes:

$$\begin{aligned} I_s(\Phi) = c\int_{-w/2}^{w/2} j_c(y)sin(\phi(y))dy \\ &= c\int_{-w/2}^{0} j_0 sin(\phi_0 + \frac{2\pi\Phi\frac{y}{w}}{\Phi_0})dy + c\int_{0}^{w/2}(-j_0)sin(\phi_0 + \frac{2\pi\Phi\frac{y}{w}}{\Phi_0})dy \\ &= I_0\frac{sin(\phi_0 + \frac{\pi\Phi}{2\Phi_0})sin(\frac{\pi\Phi}{2\Phi_0})}{\frac{\pi\Phi}{2\Phi_0}} \end{aligned} \tag{2.15}$$

Maximizing with respect to ϕ_0, we obtain the field dependent critical current for a symmetric corner junction on a material with $d_{x^2-y^2}$ pairing symmetry:

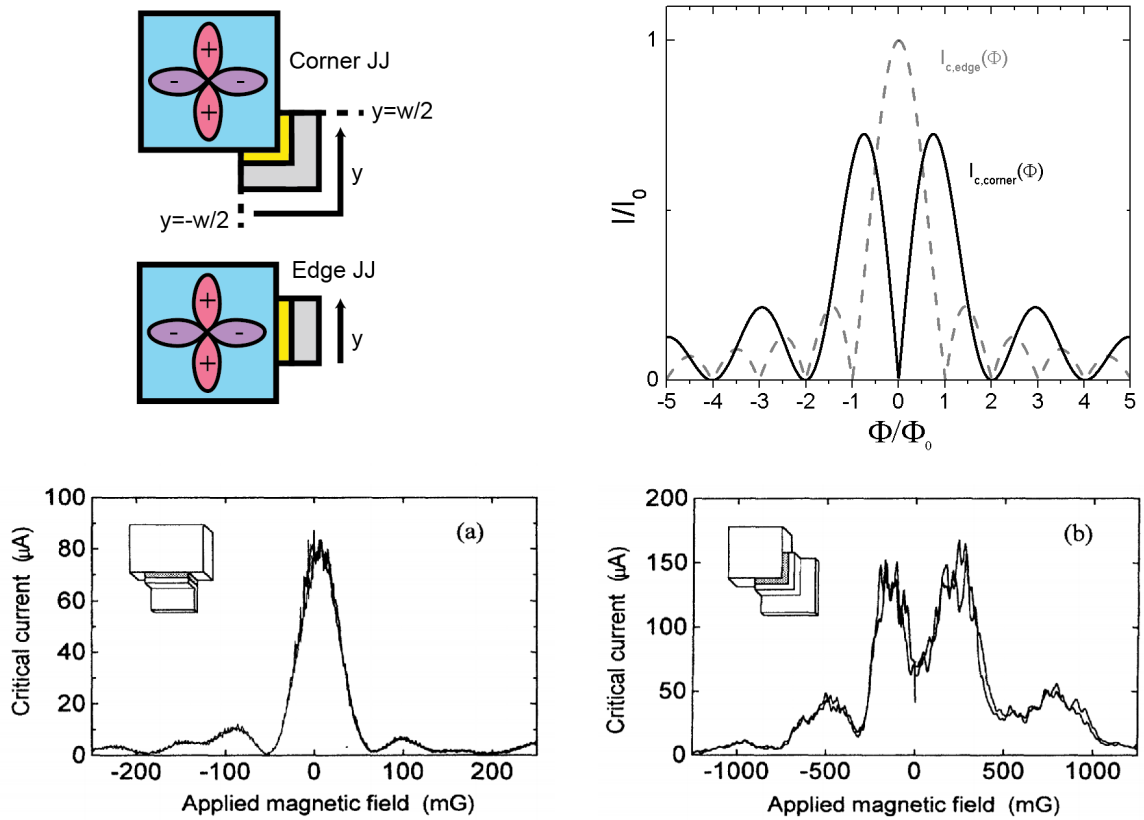

Figure 2.4: Top Left: Symmetric Josephson junction fabricated on the corner of a d-wave superconductor, with an s-wave superconducting electrode (gray) on the other side of the barrier (yellow). The y-coordinate follows the length of the junction as it rounds the corner. Mid left: Josepshon junction along a single face of the same material. The phase of the order parameter of the d-wave superconductor does not change sign over the length of the junction. Top Right: Comparison of $I_c(\Phi)$ of the corner and edge junctions. Bottom: Experimentally measured $I_c(\Phi)$ of YBCO-Pb edge (left) and corner (right) Josephson junctions, from [75]. The corner junction shows a clear suppression of $I_c(0)$, consistent with d-wave pairing.

$$I_c(\Phi) = I_0 \left| \frac{sin^2(\frac{\pi\Phi}{2\Phi_0})}{\frac{\pi\Phi}{2\Phi_0}} \right| \tag{2.16}$$

As we can see in Fig. 2.4, this expression is visibly different from the result for $I_c(\Phi)$ derived earlier for a junction between two s-wave superconductors. First, the periodicity of nodes in I_c is halved. Secondly, $I_c(0)$ is completely suppressed. The latter follows logically from the difference in sign of the critical current density across y=0. Conversely, a junction formed entirely along either the (100) or (010) crystal axis would have a uniform critical current density of the junction area, and would have an $I_c(\Phi)$ which would follow the typical Fraunhofer pattern for a Josephson junction, given by Figure 2.9. This sitaution was first experimentally realized in [75], which provided compelling evidence for the existence of $d_{x^2-y^2}$ pairing symmetry in the

cuprate superconductor YBCO.

We will apply this technique in chapter 5 to look for deviations from d-wave symmetry near criticality in highly overdoped LSCO, the disordered d-wave superconductor discussed in section 1.4.2.

2.4 Josephson current-phase relation measurements

While a typical Josephson junction has a sinusoidal relationship between supercurrent and phase as described by equation 2.3, the current-phase relation of a Josepshon junction can more generally be expressed [76] as a sum of sinusoidal terms, such that

$$I_c(\phi) = \sum_{n \geq 1} I_n sin(n\phi_n) \tag{2.17}$$

which reduces trivially to 2.3 when all but the n=1 term are neglected. Measuring the current-phase relation (CPR) of a Josephson junction can provide useful information about the physical processes that govern the supercurrent. In this section, we will discuss two techniques for performing this measurement, and how it can provide information about the pair-density wave state predicted to exist in LBCO.

2.4.1 Current-phase relation of Josephson junctions with spatially varying phase difference

Recall our discussion of the striped superconductor and the pair density wave state in Chapter 1. One key feature of the pair-density wave state in a material such as LBCO is that the phase of the superconducting order parameter at each charge stripe should be shifted in phase by π. Due to this phase shift, two hypothetical Josephson junctions formed on adjacent stripes would then carry current with opposite sign. However, the incredibly small scale of the spacing ($\approx$ 12Å) between adjacent stripes makes fabricating a junction on an individual stripe impractical. Instead, we can consider a junction formed on an in-plane axis that contains several stripes, such that the phase rapidly changes from 0 to π several times over the junction area.

Such a system is similar to grain boundary junctions in which two grains of a d-wave superconductor are misaligned at some angle θ, causing the phase of the order parameter across the grain boundary to shift between 0 and π repeatedly over the length of the junction. [77] Measurements of the current-phase relation of YBCO grain boundary junctions misaligned by $\theta = 45$ degrees show that the current-phase relation has a significant $sin(2\phi)$ component which increases in strength at low temperatures due to conduction through mid-gap states. [78]

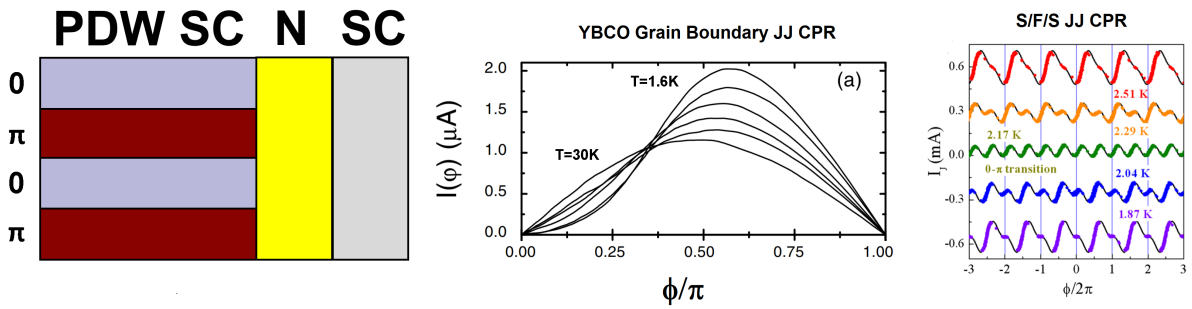

Figure 2.5: Left: PDW superconductor-normal metal-s-wave superconductor Josephson junction. Adjacent stripes are phase-shifted by π. Mid: Measured current phase relation of YBCO grain boundary junction, which also experiences 0-π phase shifts. This has a sin(2ϕ) component at low T due to predicted midgap states. From [78]. Right: Measured CPR of an S/F/S Josephson junction has a clear sin(2ϕ) component, which dominates at the 0-π transition. From [81].

Additionally, Josephson junctions with a ferromagnetic weak link can experience a transition a from 0- to π- state depending on the thickness of the weak link due to the effect of the exchange field in the ferromagnet. [79] Inhomogeneity in the barrier can lead to an intermediate regime in which some areas of the junction are in the 0- state and others are in the π-state, causing changes in sign over the junction area. [80] Current-phase relation measurements of such S-F-S junctions show a sin(2ϕ) component which dominates at the 0-π transition, in which the typical $sin(\phi)$ component of the current-phase relation is suppressed. [81]

Theoretical treatments of systems containing junctions with rapidly varying alternations of phase between 0 and π are able to reproduce this $sin(2\phi)$ harmonic using a coarse-graining approximation, in which the critical current density within a $0-$ or $\pi-$ region varies little compared to the difference in magnitude between adjacent regions. [82, 83] These predictions together with the above observations of a $sin(2\phi)$ harmonic in other types of Josephson junctions with spatially varying phase lead us to believe that $0-\pi$ phase shifts between stripes in LBCO due to the PDW model will lead to a $sin(2\phi)$ harmonic in a Josephson junction fabricated on this material.

For this reason, we are interested in measuring the current-phase relation of a Josephson junction incorporating LBCO in order to probe for evidence for the PDW state. We will discuss techniques to measure the current-phase relation of a Josephson junction in the following section, and present the results of these measurements in chapter 4.

2.4.2 The rf SQUID

Our approach is based on a well-studied experimental method which involves coupling a junction with a phase difference ϕ to a superconducting ring with some inductance L.[84, 85] Notable previous applications

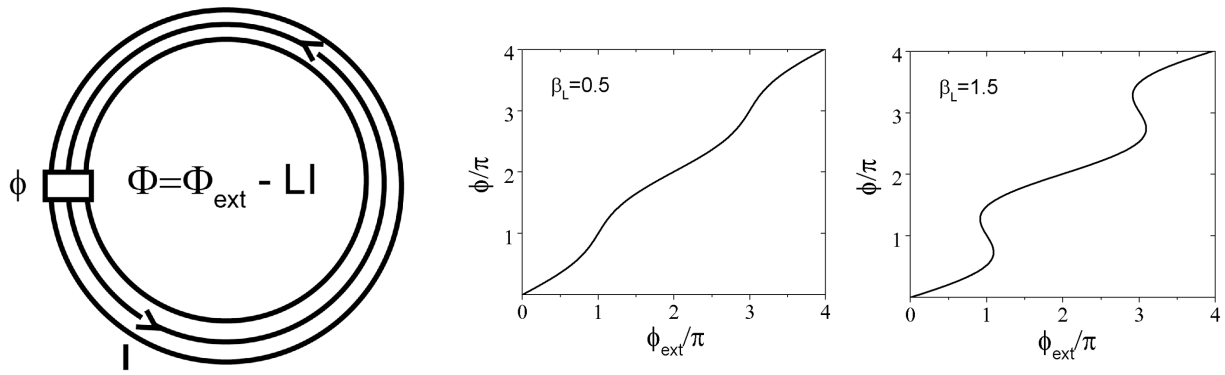

Figure 2.6: Left: Drawing of an rf SQUID, which consists of a superconducting ring interrupted with a Josephson junction with phase ϕ across the barrier. Net flux through the loop is $\Phi_{ext} - LI$, where L is the inductance of the ring and I=$I_0 sin(\phi)$ for a typical Josephson junction. Mid: ϕ is a single valued function of ϕ_{ext} for $\beta_L < 1$, where $\beta_L = \frac{2\pi L I_0}{\Phi_0}$. Right: The response of $\phi(\phi_{ext})$ becomes hysteretic for $\beta_L > 1$.

of this technique include measuring the current-phase relation of junctions using ferromagnetic materials or graphene as the weak link.[86, 87] First, we will discuss some basic properties of this system, which is known as an rf SQUID, drawn in fig. 2.6. As in section 2.2, we require that the phase difference across a path traveling around the complete length of the ring must be an integer multiple of 2π for the phase ϕ to be single-valued. Assuming that $\int_{JJ} \mathbf{A} \cdot d\mathbf{l}$ is negligible, this gives us the flux quantization condition

$$\oint \nabla\phi \cdot d\mathbf{l} = 2\pi n = \phi - \frac{2\pi}{\Phi_0} \int_{ring} \mathbf{A} \cdot d\mathbf{l} = \phi - \frac{2\pi\Phi}{\Phi_0} \tag{2.18}$$

For n=0, when no flux is trapped in the ring, this reduces simply to

$$\phi = \frac{2\pi\Phi}{\Phi_0}. \tag{2.19}$$

Hence, under the right conditions, the flux Φ in an rf SQUID has a clear correspondence with the phase ϕ of the enclosed Josephson junction. In the next section, we will discuss a measurement circuit which takes advantage of this property to directly measure the current-phase relation of a Josephson junction. However, we must also take into account that any Φ_{ext} applied to the loop will be opposed by an induced $\Phi_{ind} = LI$, such that the total $\Phi = \Phi_{ext} - LI$. Assuming a typical sinusoidal current-phase relation through the junction, we can set I=$I_0 sin(\phi)$ as well as define the parameter $\beta_L = \frac{2\pi L I_0}{\Phi_0}$ and the normalized external flux $\phi_{ext} = \frac{2\pi\Phi_{ext}}{\Phi_0}$, such that for n=0,

$$\phi - \frac{2\pi(\Phi_{ext} - LI_0 sin(\phi))}{\Phi_0} = 0 \implies \phi = \phi_{ext} - \beta_L sin(\phi) \tag{2.20}$$

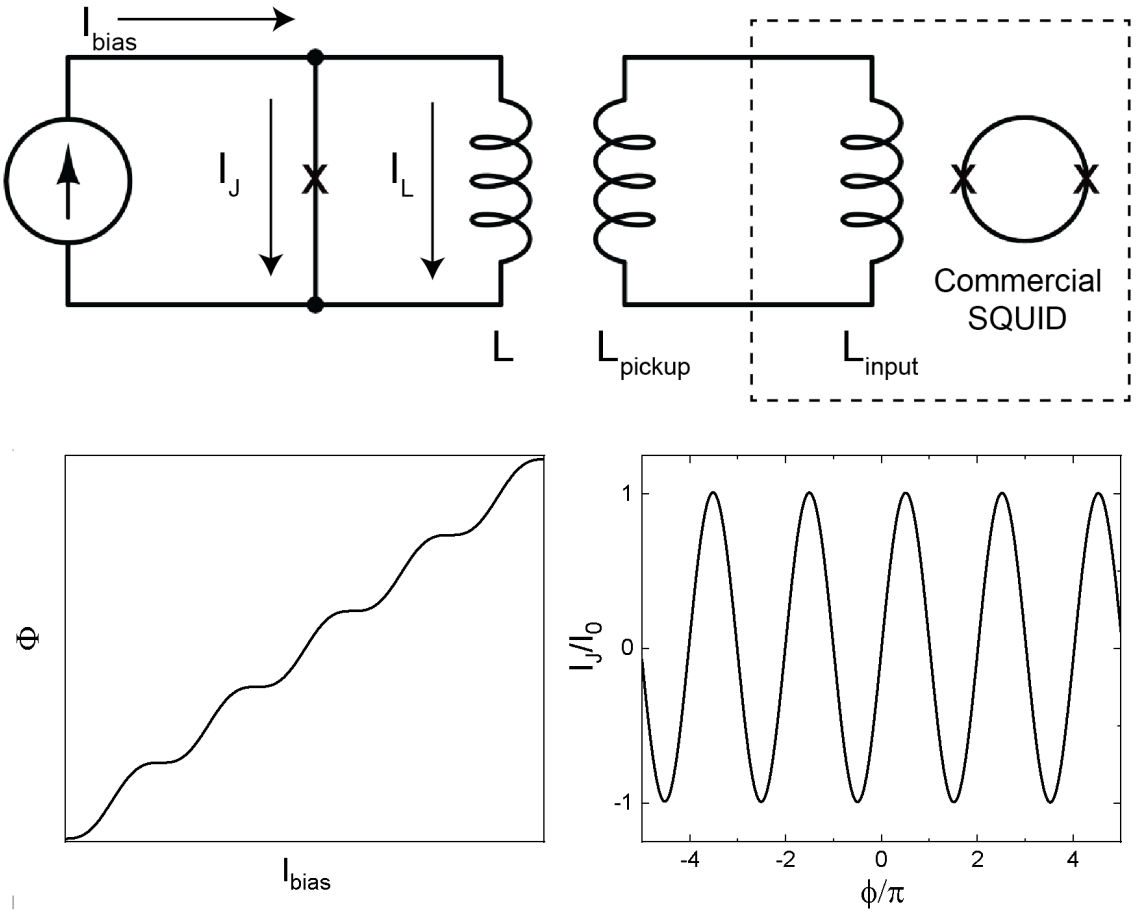

Figure 2.7: Top: Current-phase relation measurement circuit. Bias current induces a flux Φ through the inductor which varies periodically according to the current-phase relation of the Josephson junction connected in parallel. The inductor is coupled to a SQUID with a pickup coil, allowing precise measurement of Φ. Bottom left: Theoretical $\Phi(I_{bias})$ with arbitrary units for a junction in this circuit with $\mathrm{I}_J(\phi) = I_0 sin(\phi)$. Bottom right: Inversion of $\Phi(I_{bias})$ and subtraction of the linear term due to the inductor yields the sinusoidal current-phase relation of this junction.

This tells us that when $\beta_L < 1$, ϕ is a single valued function of ϕ_{ext}, but when $\beta_L > 1$, the response of ϕ to ϕ_{ext} becomes hysteretic, or multiply-valued. We illustrate this property in Figure 2.6.

2.4.3 Direct method to measure the Josephson current-phase relation

Suppose a current I_{bias} is maintained through a Josephson junction in parallel with an inductive washer L, as shown in the circuit diagram in Figure 2.7. Assuming that the inductance l of the junction arm is small, this current should divide through the junction and washer inductance such that

$$I_{bias} = I_L + I_J(\phi) = \frac{\Phi}{L} + I_J(\frac{2\pi\Phi}{\Phi_0}) \tag{2.21}$$

where $I_J(\phi)$ is the current-phase relation of the junction being measured. By coupling a SQUID to the inductor, we can measure the induced Φ as a function of applied bias current I_{bias}. Inverting this curve to find $I_{bias}(\Phi)$ and subtracting the linear contribution of the inductor, we can isolate the current-phase relation $I_J(\phi)$ as a function of measurable quantities:

$$I_J(\phi) = I_J(\frac{2\pi\Phi}{\Phi_0}) = I_{bias}(\Phi) - \frac{\Phi}{L} \tag{2.22}$$

A hypothetical extraction of the CPR from such a circuit is shown in figure 2.7. In order to couple the SQUID to the sample, a pickup loop acting as a flux transformer is spot welded to the SQUID input coil to ensure robust superconducting contact, and fastened directly above the washer using dental floss. To maximize sensitivity, the inductance L_{pickup} of the pickup coil is matched to the geometric mean of the SQUID input inductance L_{input} and the washer inductance L, such that $L_{pickup} = \sqrt{LL_{input}}$. [88] The inductances of a typical SQUID input coil and $1mm^2$ square washer used in this experiment are roughly $L_{input} \approx 2\mu H$ and $L \approx 2nH$, respectively, so the ideal $L_{pickup} \approx 63.25nH$. We create a pickup loop of appropriate inductance by winding a 1mm diameter pickup coil out of $N = 17 \sim 20$ closely packed turns of superconducting NbTi wire, held together by G1 epoxy.

In order for the response of the measured flux Φ in the circuit to be a single-valued function of the phase ϕ across the junction, it follows from the discussion in section 2.4.2 that $\beta_L = \frac{2\pi L I_0}{\Phi_0} < 1$, which requires that the junction critical current $I_0 < \frac{\Phi_0}{2\pi L} \approx 165nA$. This imposes a significant constraint on this measurement technique: if junction critical currents are too high, the circuit becomes hysteretic and a current-phase relation cannot be extracted without encountering artifacts such as backward skewness.[87] Junctions with smaller area and thicker barriers can have smaller I_c, and I_c tends to be suppressed with increasing temperature. In practice, I_c of the junctions fabricated for this thesis work were in the hysteretic regime at base temperature, and were measured at intermediate temperatures ($1 \sim 3$K) to suppress I_c enough to extract a CPR. However, because the signal to noise ratio of this measurement drops with increasing temperature, the result is a fairly narrow range of accessible temperatures for a given junction. For this reason, we will supplement our current-phase relation data obtained through the aforementioned flux transformer method with data obtained using an alternate technique, which involves applying an external field to an asymmetric SQUID.

2.4.4 Asymmetric SQUID technique to measure the CPR

Consider a dc SQUID as described in section 2.2, except instead of two symmetric junctions with $I_{c1} = I_{c2}$, we have two junctions with critical currents I_c^L and I_c^S, where $I_c^L >> I_c^S$. The critical current of a SQUID

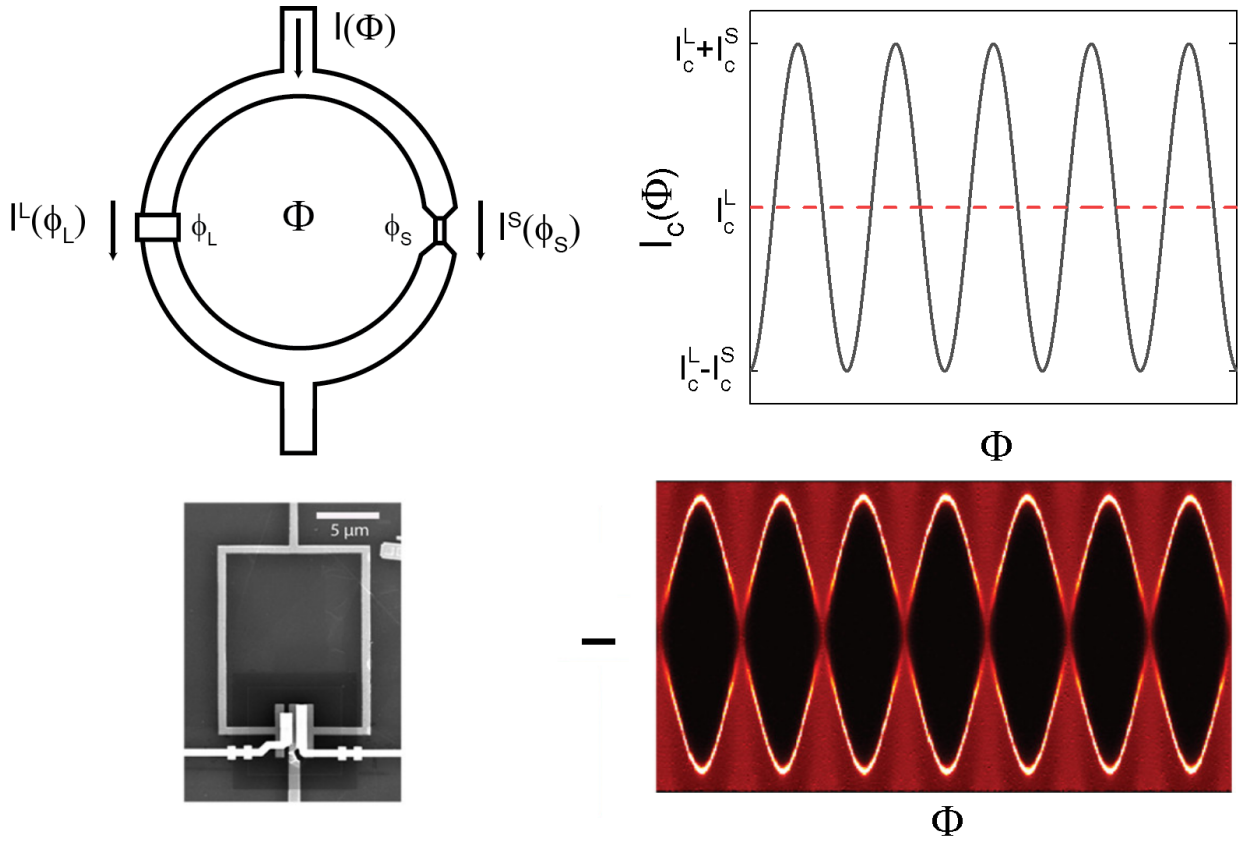

Figure 2.8: Top left: Asymmetric SQUID setup with $I_c^L >> I_c^S$. Top right: In this regime, fluctuations in $I_c(\Phi)$ about I_c^L are entirely due to the current-phase relation of the smaller junction $I^S(\phi_S)$. In this example, the measured CPR is a simple sinusoid. Bottom left: Scanning micrograph of asymmetric SQUID circuit in [89] to study ballistic graphene junctions. Bottom right: Differential resistance vs I, Φ of the example from [89]. Black regions indicate a supercurrent, with maximum amplitude of order $0.4\mu A$.

composed of two such junctions with arbitrary current-phase relations $I^{L,S}(\phi) = \sum_{n\geq 1} I_n^{L,S} sin(n\phi_{L,S})$ should behave as

$$I_c(\phi_L, \phi_S) = I^L(\phi_L) + I^S(\phi_S) \tag{2.23}$$

Following the same flux quantization arguments laid out in 2.2, we find that in the absence of trapped flux (n=0),

$$\phi_S - \phi_L = \frac{2\pi\Phi}{\Phi_0} \tag{2.24}$$

Where Φ is the flux through the SQUID. Combining the above two relations, we can then write

$$I_c(\Phi, \phi_L) = I^L(\phi_L) + I^S(\phi_L + \frac{2\pi\Phi}{\Phi_0}) \tag{2.25}$$

Next, because $I_c^L >> I_c^S$, $I_c \sim I_c^L = I^L(\phi_{max})$. Hence in the vicinity of the SQUID's I_c, ϕ_L is approximately fixed at a constant ϕ_{max}, while ϕ_S can vary freely. For example, if the large junction had a sinusoidal current-phase relation $I^L(\phi_L) = I_c^L sin(\phi_L)$, we would have $\phi_L \approx \phi_{max} = \pi/2$. With ϕ_L constant, we can write the current-phase relation $I^S(\phi_S)$ as a function of the external flux Φ, as follows:

$$\begin{aligned} I_c(\Phi, \phi_L) = I_c(\Phi) &= I_c^L + I^S(\phi_{max} + \frac{2\pi\Phi}{\Phi_0}) \\ \implies I^S(\phi_S) &= I_c(\Phi) - I_c^L \end{aligned} \tag{2.26}$$

As a result, fluctuations in critical current of an asymmetric SQUID under the application of an external flux Φ directly represents the current-phase relation $I^S(\phi_S)$ of the smaller junction. Prior to the work in this thesis, this technique was successfully applied to study the current-phase relation in systems such as superconducting atomic contacts and ballistic graphene Josephson junctions. [89] [90]

Chapter 3

Experimental Methods

The bulk of the measurements in this thesis take place on Josephson junctions and SQUIDs fabricated onto cuprate crystal samples. However, several processing steps are required in order to make such devices. The orientation of the crystals must be defined, the crystal must be fixed to a substrate, the junction geometry must be patterned, normal and superconducting layers must be deposited, and good electrical contact must be established across the crystal-normal metal interface. Additionally, contact must be made between the vertical junctions and the planar device geometry on the substrate.

3.1 Crystal Alignment and Preparation

The crystals studied in this work are grown through the floating-zone technique, in which two ceramic rods are brought together such that their tips meet in the "hot zone" of a specialized furnace. The tips of the rods melt together to form a liquid bridge, or "floating zone." Through translation of the rods or the furnace's hot zone, the molten zone moves upward through the top rod, allowing previously melted areas to cool and crystallize, forming a large single crystal. [91] The LBCO crystals were provided by Genda Gu's lab in Brookhaven, the LESCO crystals were grown by Greg Macdougall's group at UIUC, and the LSCO crystals were grown by Masaki Fujita's group at Tohoku University.

However, crystals grown using the floating-zone technique often do not have facets, and alignment of the output crystal depends on the crystal alignment of the lower (seed) rod. Further, the growth direction does not always correspond to an experimentally useful crystal axis, and materials such as LBCO and LSCO do not cleave easily. For these reasons, we need to undergo additional fabrication and characterization to fabricate junctions parallel to the copper-oxide planes, as proposed in section 2.4.1.

Recall from Chapter 1 that in materials such as LBCO and LESCO near 1/8 doping, superconductivity within the CuO_2 planes (oriented in the ab-plane) has a higher T_c than superconductivity along the c-axis, between the CuO_2 planes. Additionally, due to the d-wave pairing symmetry of cuprate superconductors, there is a phase difference of π in the superconducting order parameter between the a- and b- planes. For

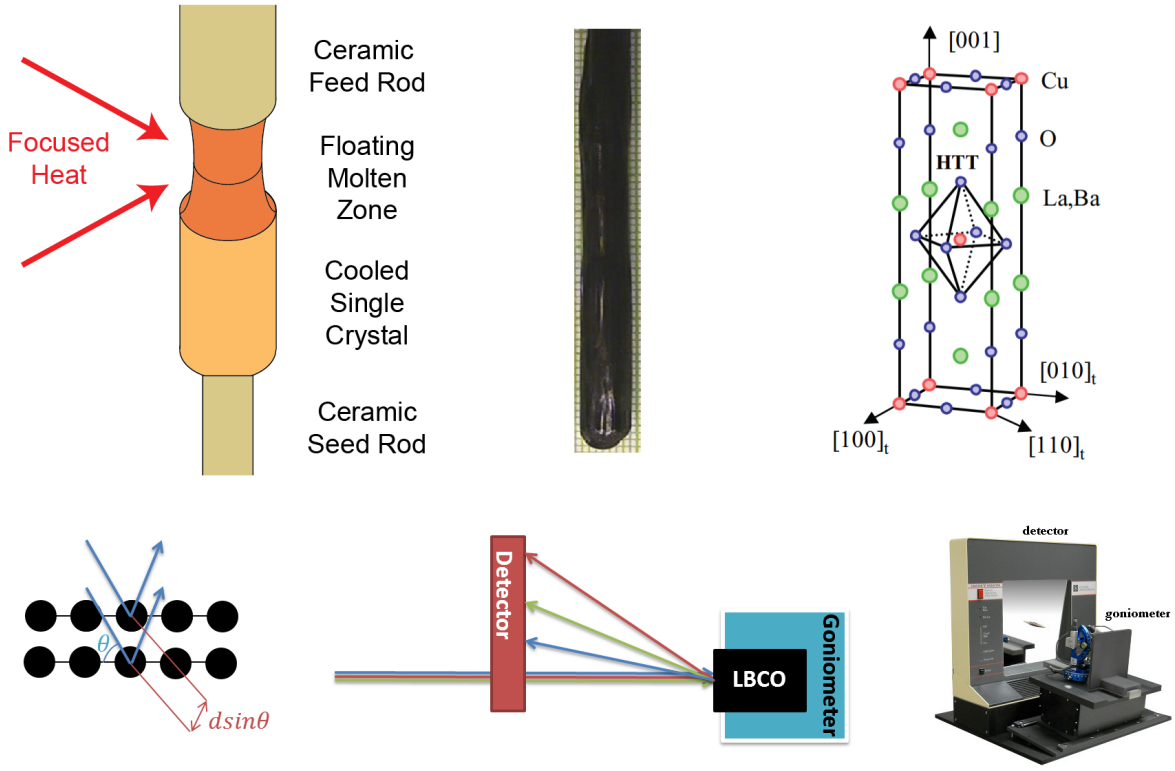

Figure 3.1: Top Left: illustration of floating zone technique. Focused heat melts the ceramic "feed" rod such that it melts onto the "seed" rod, cooling to form a single crystal. Top Mid: BSCCO single crystal grown using this technique, from [91]. Top right: LBCO crystal structure, from [55]. Bottom left: Bragg's law illustration. Constructive intereference occurs when the condition $2dsin(\theta) = n\lambda$ is satisfied. Bottom mid: Principle of Laue x-ray diffraction. Different components of a multichromatic beam scatter onto the detector at different angles. The symmetry of diffraction maxima picked up by the detector corresponds to the symmetry of the crystal in the beam direction. Bottom right: Image of Multiwire Laue camera system, from [92]

most of these experiments, we place crystals on the substrate such that the c-axis is normal to the substrate, and form junctions on faces aligned with a- and b- axes. In order to obtain our desired alignment, we can measure a crystal using Laue diffraction, then fix that alignment in place for cutting or polishing.

In back-reflection Laue diffraction, a polychromatic x-ray source is shined on a single crystal, and the reflected x-rays are recorded by a detector.[93] For each wavelength λ of the beam, which is incident at a given crystal plane at an angle θ, constructive interference occurs when $2dsin(\theta) = n\lambda$, from Bragg's law, where d is the interplanar distance. Since several wavelengths λ are shined on the sample from the x-ray source, multiple Bragg reflections are possible off the sample's lattice planes, which appear as spots on the detector at positions which correspond to the crystal's symmetry in the chosen orientation.[94]

Laue diffraction of these crystals was performed using the Multiwire Laboratories MWL120 Real-Time

Back-Reflection Laue Camera System in the UIUC Materials Research laboratory. First, the crystal is attached to the goniometer chuck using double-sided tape or putty. Then, the goniometer is rotated until the array of diffraction spots is observed to show the desired symmetry. For instance, the materials studied in this thesis have tetragonal symmetry under space group space group I4/mmm, such that four mirror planes at 45 to one another intersect along a fourfold rotation axis, which we define as the 001 axis. [95] Another two mirror planes at right angles to the fourfold axis intersect the other mirror planes along four twofold rotation axes, which we identify as the 100 and 010 directions.[96] Hence, the measured diffraction spots obtained by the Laue method will show 2-fold rotation symmetry in the 100 or 010 directions with 2 mirror planes, and 4 fold rotation symmetry with 4 mirror planes in the 001 direction. An example of Laue diffraction used to determine crystal axes is shown in Figure 3.2.

Once the desired crystal alignment has been found, the crystal must be transferred in place to a polishing or cutting chuck, allowing a new face, aligned to the relevant axis, to be cut into the crystal. In order to do this, we use a custom piece of equipment made by the MacDougall group, which mounts onto the same rail as the goniometer and can securely align a polishing chuck in front of the goniometer-mounted crystal. The polishing chuck is moved as close as possible to the crystal without touching it or disturbing the angular position of the goniometer. Then, a small amount of 5-minute epoxy is used to attach the crystal to the polishing chuck. After allowing at least 30-60 minutes for the epoxy to harden, the polishing chuck is carefully pulled away from the goniometer, taking the aligned crystal with it.

After initial alignment, the mounted crystal is typically taken to a lab bench for polishing. Initially, the chuck is gently moved in a figure-eight motion over coarse emery paper to define a face in the aligned axis. Ideally only a few μm of material should be exposed during polishing. For this reason, a stainless steel shield is screwed onto the polishing chuck to limit the amount of material exposed to the abrasive paper. Once the exposed material has been polished away, the shield can be lowered to allow further polishing. To do this contollably, the chuck is placed on top of a plate containing a large screw. The shield screw is loosened to allow adjustment, the large screw is twisted slightly to change the relative position of the chuck and shield, and then the shield is tightened again. These steps are repeated until a face of the desired size has been polished into the crystal. Then, the crystal face is polished for a short time on successively fine grit emery paper, followed by a set of increasingly fine lapping papers, to create a smooth facet. To remove the crystal from the chuck epoxy, the chuck is placed in a beaker containing CH_2Cl_2 overnight, which aggressively dissolves the cured epoxy.

Now that an aligned crystal face has been polished into the crystal, the crystal is placed back into the Laue camera system to find the orientation of a perpendicular face, and the above steps are repeated for

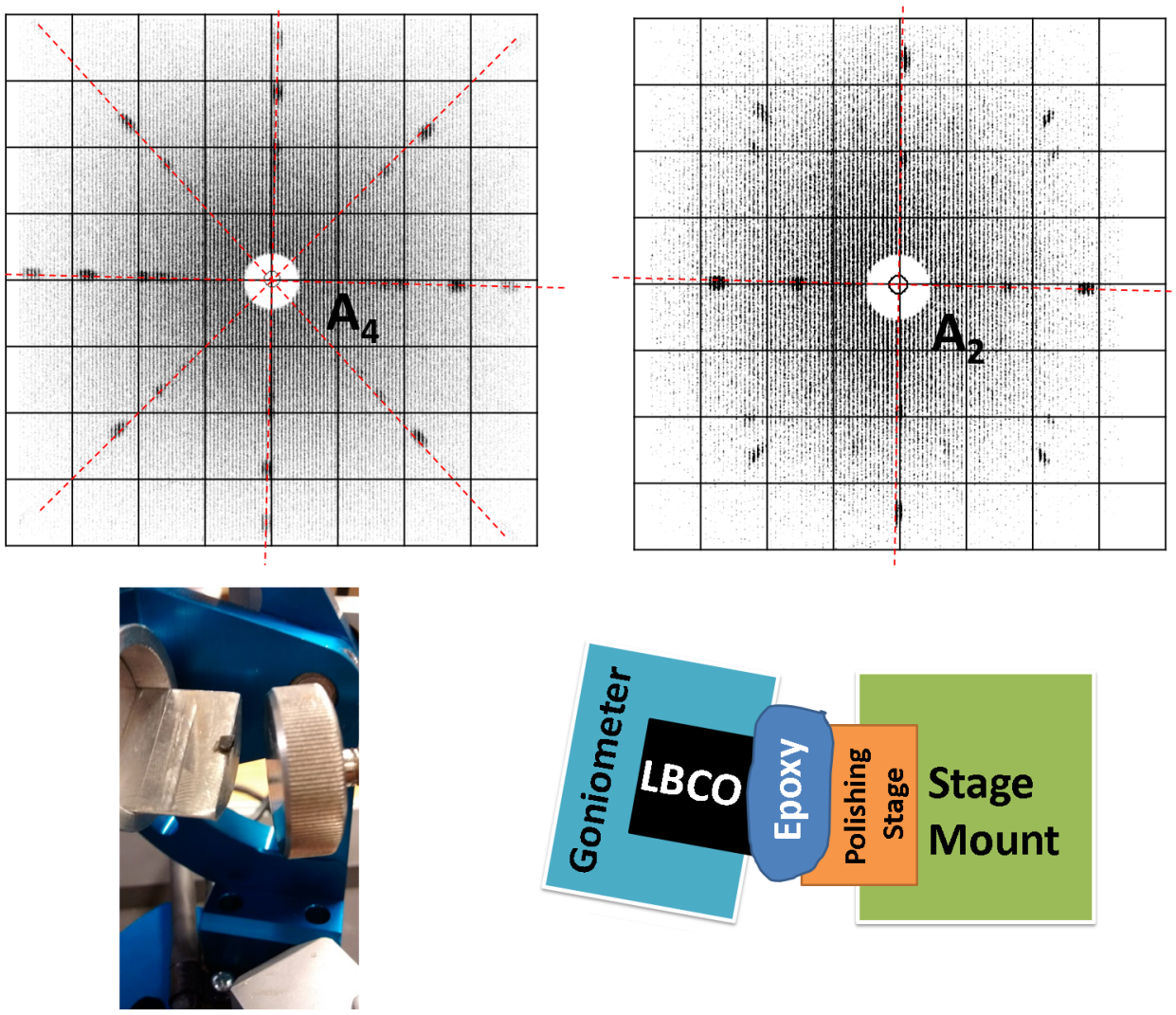

Figure 3.2: Top left: Laue camera image of an LBCO crystal oriented in the 001-direction, as determined by the marked mirror planes and rotation symmetry axis. Top right: LBCO crystal oriented in the 100- or 010-direction (both are equivalent). Bottom left: Real image of LBCO crystal (black) mounted on goniometer chuck, opposite the alignment transfer rig (stage mount). Bottom right: Schematic image of alignment transfer. Crystal is epoxied to a polishing or cutting stage attached to the stage mount in order to preserve the orientation. This epoxy is stronger than the adhesive used to mount to the goniometer, allowing the oriented crystal to be carried away in place for further processing.

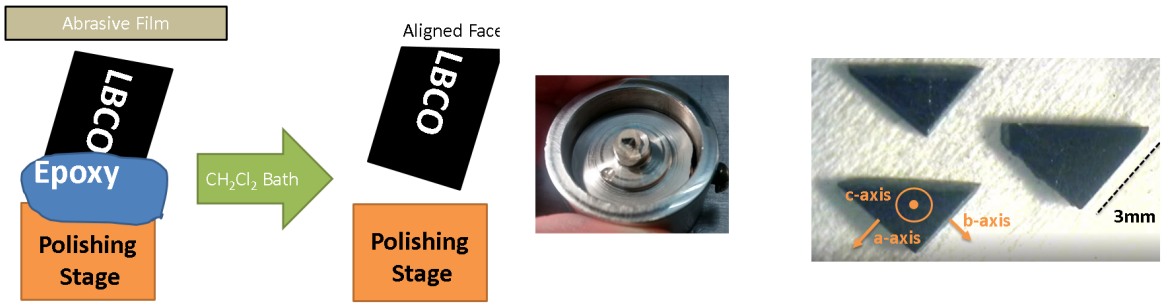

Figure 3.3: Left: Aligned crystal is polished by an abrasive film, creating a facet, then removed from the epoxy by a halogenated solvent. Mid: Photograph of crystal glued to polishing stage. Movable shield allows a controllable thickness of material to be removed. Right: LSCO crystals after alignment and polishing. Polished facets lie along a, b and c axes, as shown.

that face, until we are left with a crystal with two orthogonal polished faces aligned with crystal axes.

In the case of a small ($\leq$2mm side length) crystal, the remaining facets can be defined entirely via polishing, without any further x-ray orientation. If a rectangular geometry is desired, the crystal can be glued to a chuck along each previously polished face using Crystalbond, then polished along the opposite face. Crystalbond can be adhered to a crystal by heating it to 70C on a hot plate, and can be washed off easily in acetone. The last crystal axis can be defined by gluing the crystal orthogonal to the other two oriented directions, and polishing again. The end result of this procedure is a crystal with smooth facets along the a, b and c directions.

For a large (>2mm side length) crystal, a single crystal can be split into multiple aligned samples using a wire saw. To do this, we use Crystalbond to attach a crystal with at least two orthogonal polished faces to a cutting chuck such that the 001 axis is normal to the chuck. Then. the chuck is mounted to the saw such that the wire is parallel to a polished 100 or 010 face. As an abrasive slurry composed of glycerine, water and boron carbide moistens the wire, the saw makes any needed cuts. Surfaces made rough during sawing can be made uniform by polishing. This procedure produces two or more crystals with cut facets aligned with crystal axes.

3.2 Crystal junction fabrication

Now that we have a crystal with aligned facets, the next step is to define the junction geometry. Because these crystals have significant height (>0.2mm) compared to thin films, conventional lithography techniques cannot be used. Instead, we use a mechanical masking technique to produce our junctions.

First, we temporarily affix the crystal to a glass substrate using double-sided polyamide tape. Then, we

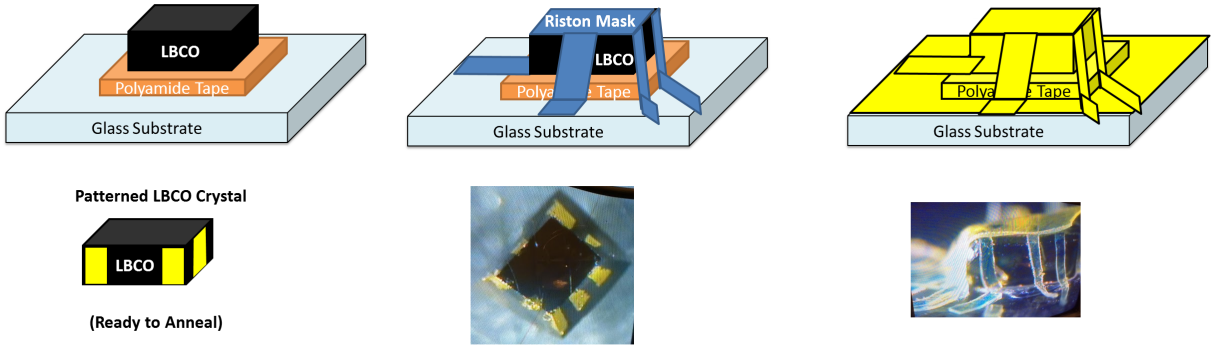

Figure 3.4: Top left: Cuprate crystal is affixed to a temporary substrate using polyamide tape. Top mid: Riston dry film photoresist is rolled over the top and sides of the crystal to mask off the desired junction geometry along the a- and b- facets. Top right: Au is evaporated onto the sample, coating all exposed faces of the crystal within line of sight of the source. In-situ stage tilting allows coverage of all sides of the crystal. Bottom left: The crystal, now patterned with Au, is removed from the temporary substrate, to be placed in an annealing furnace. Bottom mid: Microscope camera image of crystal with deposited Au layer. Bottom right: Microscope camera image of crystal during the masking process.

cut thin strips of Riston dry film photoresist, a flexible adhesive material, and carefully roll it onto the sides of the crystal such that the desired junction areas are left uncovered during evaporation, and the rest of the crystal is shielded, as shown in Figure 3.4.

Now that the junction area is defined, the normal barrier can be deposited. Before discussing deposition, we should note that normal contacts deposited on cuprate materials tend to conduct poorly, and exhibit a temperature dependence which appears semiconducting rather than resistive. This occurs because surface layer of a copper oxide tends to lose oxygen in the presence of atmospheric gases, creating an oxygen-depleted 'dead' layer with high resistivity. [97] However, it has been shown that if a layer of Au or Ag is placed on the surface of a cuprate and is annealed at high temperature (>400C) in an O_2 atmosphere, the contact resistivity is lowered significantly. [98] This process reverses oxygen loss and enhances conductivity by allowing the normal metal to diffuse through the dead layer. Au and Ag also act as a buffer preventing further O_2 loss at room temperature. Further, these materials do not oxidize, which would pull oxygen from the crystal, forming a semiconducting layer at the interface between the two materials. We avoid annealing at temperatures significantly above 400C to prevent significantly altering the chemistry or crystal structure of our samples. YBCO, for instance, experiences an orthorhombic to tetragonal structural transition after annealing at 700C. [99] With this in mind, we choose Au as our normal barrier, and introduce an annealing step to ensure low contact resistance.

To deposit our Au normal barrier, we use electron beam evaporation. Initial deposition is typically

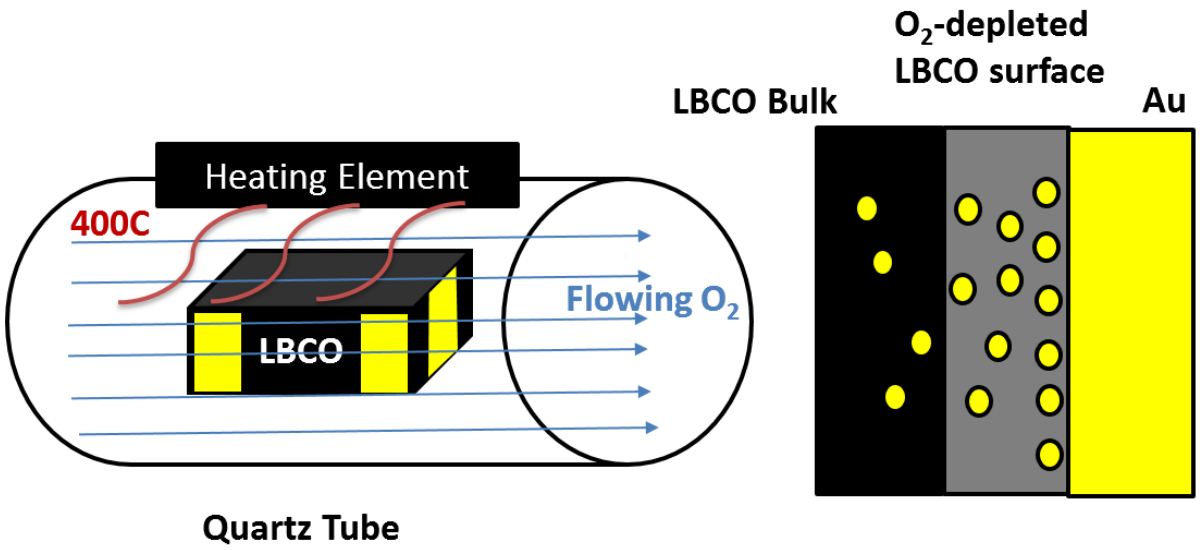

Figure 3.5: Left: Schematic of annealing process. Crystal sample is placed in flowing O_2 at 400C for 2-4 hours. Right: Annealing causes Au to diffuse through the poorly conducting surface layer of a cuprate crystal, ensuring good electrical contact.

performed in the Quantum Cluster Evaporator (QCE) in the MRL, because it has an in situ ion mill and a stage that can be tilted up to 45 degrees. After a short ion milling step to clean the surface, 50-100 nm of Au is deposited at a 45 degree angle to ensure that the side of the crystal is covered. Because the throw distance in the QCE is fairly long and the Au layer in these devices is relatively thick to improve the effect of annealing, the Au consumption per device can be large if the Au layer for these devices is deposited entirely in the QCE. For this reason, in some devices the ion milling and the deposition of the first 20-25nm of material was performed in the QCE, and the remaining thickness of Au was deposited in the Temescal Electron Beam 4 evaporator, which has lacks in-situ ion milling but consumes less Au per unit film thickness.

After the Au barrier is deposited, annealing in O_2 is performed to ensure good contact across the Au-LBCO interface, as discussed above. Before annealing, the mask is peeled off the crystal and the crystal itself is removed from the glass substrate, then transferred to a quartz boat. The boat is placed in the Lindberg 2 inch tube furnace with 2 lpm of flowing O_2 for 4 hours at 400C, following a recipe used for YBCO Josephson junctions.[100]

Now that the Au has been annealed, the crystal is ready to be attached to a substrate for measurement using polyamide resin. Initially Si was chosen as the substrate material, but this was phased out in favor of fully insulating glass or sapphire substrates due to the possibility of shorts through regions where the SiO_2 layer is damaged. To aid adhesion of the polyamide to the substrate, the portion of the substrate where the

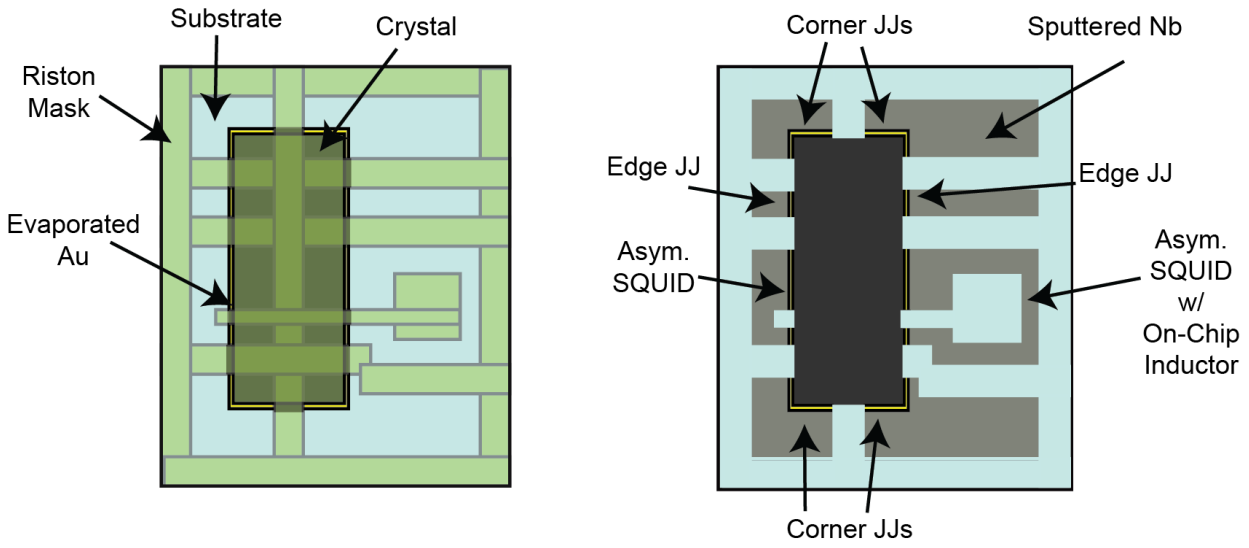

Figure 3.6: Left: Example masking geometry to create Josephson junction devices described in this thesis. Right: Sputtering Nb onto this mask, then peeling away the mask material, yields edge and corner Josephson junctions with large attached contact pads, and asymmetric SQUIDs for CPR measurement. The SQUID with a small loop on the left side is used for the I_c vs field technique described in section 2.4.4, and the large loop in the right is for coupling to an external SQUID to perform the measurement described in section 2.4.3. The latter geometry is equivalent to the circuit shown in Figure 2.7: due to the asymmetry in the junctions, the phase difference across the large junction is negligible, and the current-phase relation of the small junction can be extracted.

crystal will sit is scratched with a diamond scribe. Then, a thin layer of polyamide is applied to this region with a narrow wooden dowel. The crystal is then picked up with a teflon-coated wooden dowel and lowered gently onto the polyamide, such that the crystal sinks partially into the resin. Then, the resin is cured on a hot plate for 75 minutes, temperature ramping over the first 60 minutes from 60 to 200 degrees C.

Now that the crystal is fixed in place, the superconducting electrodes can be patterned using the mechanical masking technique described earlier. Due to the limited availability of crystals, we fabricate as many junctions as possible on the same sample. Strips of Riston resist are rolled from the substrate onto the crystal to create the boundaries of a Nb layer which contains superconducting electrodes of each Josephson junction, and connect each Au junction area to a contact pad region on the substrate. Typical geometries for the superconducting layer are shown in figure 3.6. For SQUID devices, two junction areas are shorted together with a small loop region near the crystal.

To construct the geometry for the direct current-phase relation measurement described in section 2.4.3, an inductor geometry is formed with a 1mm^2 loop to optimize coupling to the SQUID pickup coil. Because Nb would pull oxygen from our cuprate samples if contacted directly, inhibiting conduction, all Nb contacts to our crystals are made atop Au, forming Josephson junctions. Hence, our circuit for the direct current-

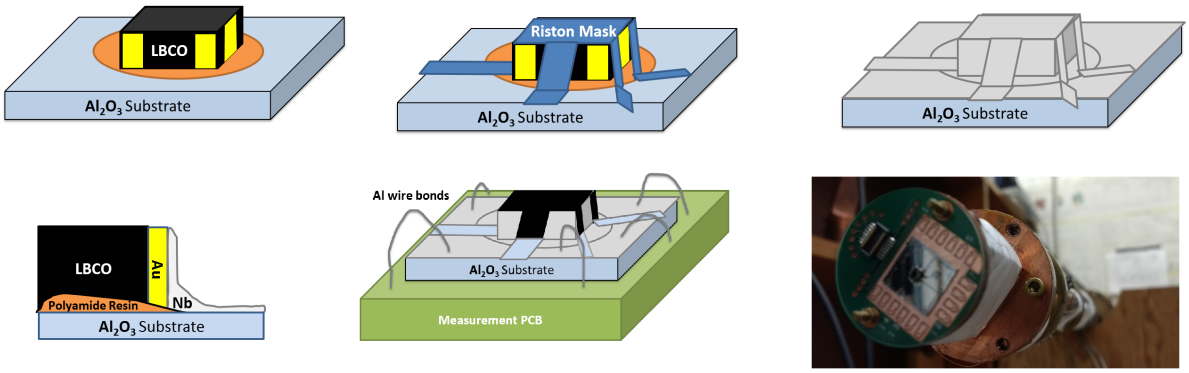

Figure 3.7: Top left: The sample is affixed to an insulating substrate using polyamide resin. Top mid: Superconducting electrode and contact pad geometry is defined through masking with Riston film. Top right: Sputtered Nb conformally coats the sample, creating a continuous Nb film from the contact pads on the substrate to the Au barrier on the crystal facets. Bottom left: Cross-section of a finished sample. Bottom mid: Sample is connected to measurement electronics via wire bonding. Bottom right: Photograph of sample mounted to cryogenic probe.

phase relation measurement differs from Figure 2.7 in that there is now a large Josephson junction in series with the small junction under test. However, if the junction is sufficiently large, we can assume that the phase difference of the large junction under test is negligible.

Once the patterning has been completed, the sample is placed in the sputter deposition chamber located in MRL 316. After a short ion mill cleaning step, 150 to 200nm of Nb is sputter deposited on the masked sample. Sputtering is used for this step because it conformally coats the sample surface with Nb, creating a continuous Nb film from the side of the crystal to the substrate.

The sample is then mounted onto a circuit board with silver paint, and connections are made to it with a wedge bonder. The board, in turn, is mounted onto a cryogenic probe for measurement and connected to room temperature electronics via a Molex cell phone connector.

3.3 Cryogenics and Measurement Electronics

Initial measurements took place using a probe with 12 measurement leads and an attached Quantum Design SQUID can. The probe was immersed in a super-insulated ^{4}He dewar, which, using heating and variable pumping, could be controlled in temperature from 4.2K to 1K. The system could hold ^{4}He for 16 hours at a time, and had fairly short turnaround times.

Later measurements used a single-shot ^{3}He probe with a base temperature of 310mK and 16 measurement leads. In order for this system to reach base temperature, a capillary fills the 1K pot of the system with

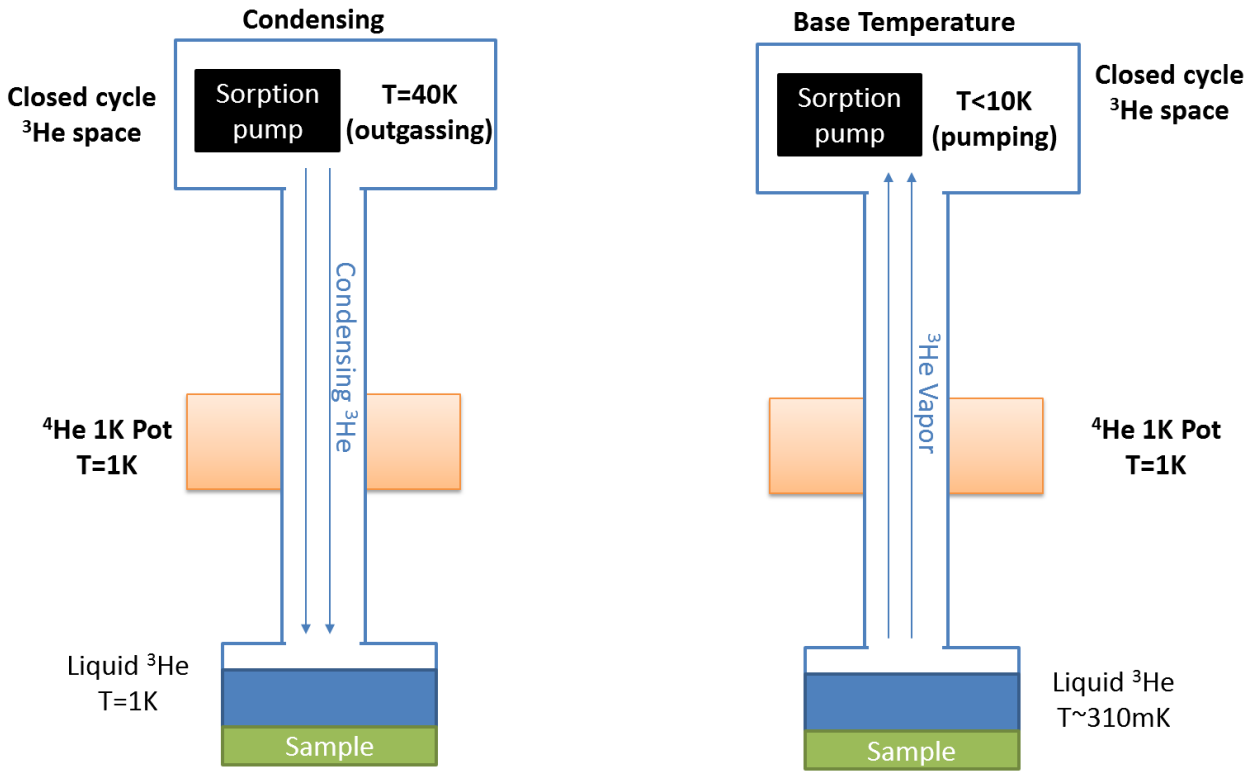

Figure 3.8: Principle of operation of the ^{3}He refridgerator. Left: ^{3}He gas is released by the activated charcoal sorb when it is heated up. This gas is cooled by pumped ^{4}He in the 1K pot, causing it to condense to liquid. Right: After all the ^{3}He has condensed, the sorbption pump is cooled, causing it to pump on the ^{3}He space, which enables it to cool to roughly 310mK.

^{4}He. A pump reduces vapor pressure of the ^{4}He, cooling it to a temperature of roughly 1.5K. Once the 1K pot temperature has stablized, a heater inside the sealed ^{3}He space heats up an activated charcoal sorb to 40K, causing it to release the gaseous ^{3}He stored within. This ^{3}He vapor, cooled by the 1K pot, condenses to liquid at the bottom of the closed ^{3}He space, which is thermally connected to the sample. After about 30 minutes of condensing, heat to the sorb is turned off and it is cooled through thermal contact to the ^{4}He recovery line. Once the sorb temperature has been reduced to less than 10K, it begins to pump on the ^{3}He space, reducing the vapor pressure of the liquid ^{3}He and reducing its temperature to roughly 310mK. The temperature of the sample can be further controlled through the application of heating to the sorb. Over the course of 2-4 hours of operation at base temperature, the ^{3}He vapor in the system will evaporate, and the condensation procedure must be repeated to further cool the sample with the ^{3}He bath.

In addition to the direct CPR measurement method described in section 2.4.3, four terminal measurements of current vs voltage were a key technique we used to characterize the behavior of Josephson junctions measured in this thesis. This four-point configuration has the advantage of eliminating the resistance of wires and other circuit elements leading up to the junction. Because all contacts to a crystal are formed with Josephson junctions, this is accomplished by placing current leads between the junction under test and a second junction, and a set of voltage leads between the junction under test and a third junction, which are measured by an Ithaco preamplifier. This configuration is shown in figure 3.9. Current is typically output by a DAQ in series with a 100k-1MΩ bias resistor, and junction current is recorded by a second Ithaco preamplifier which measures the voltage across a small resistance in series with the current path.

To improve the signal:noise ratio, a sum box can be used to add a small oscillating perturbation to our bias current, such that a lock-in amplifier connected in parallel with either preamplifier will measure the component of the signal which oscillates at the same frequency as the perturbation. This has the effect of measuring the derivative of the signal, and significantly reduces the effect of noise sources such as 60Hz noise. However, because RC filtering is crucial to the operation of a lock-in amplifier, the output needs time to adjust to changes in the input signal, which slows down the speed of data acquisition. We also use a lock-in to improve the signal to noise ratio of current-phase relation measurements, which we will discuss further in Chapter 4.

Magnetic field is typically applied to our samples using a randomly wound solenoid concentric with our sample stage, which produces about 80mG of field per mA applied. A μ-metal shield around our measurement dewar and a lead bag around the sample space help to screen out the unwanted electromagnetic radiation. Current is applied to the solenoid using a custom-made battery powered current source controlled by the voltage of the DAQ, which is fed through a battery powered optical isolator to prevent ground loops.

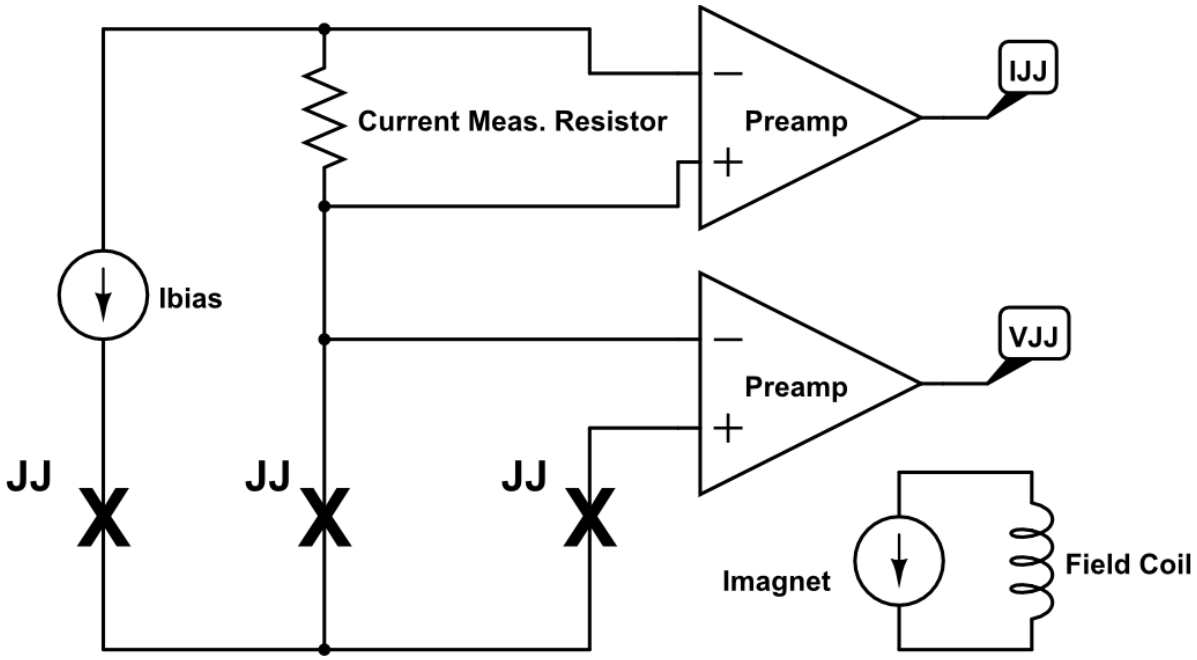

Figure 3.9: Basic 4 point measurement setup. Current is passed between the junction under test (center) and another junction a junction (left), and the voltage between the junction under test and a third junction (right) is measured. This eliminates all additional resistances besides that of the junction under test. A second current supply drives a current through the a magnet coil, which controls the flux through the junction.

Most data was taken using LABVIEW programs to communicate with the DAQ, which would step through different values of output current and record measured inputs at each value. Plotting and further data analysis was typically accomplished through Origin software or custom MATLAB scripts. In the following chapters, we will discuss the specific results we obtained from these measurements, and the our interpretation thereof.

Chapter 4

Search for PDW order via phase-sensitive measurements of LBCO-Au-Nb Josephson junctions

The goal of this chapter is to find evidence for the pair-density wave state through measurement of a sin(2ϕ) component of a Josephson junction fabricated on LBCO, as we discussed in sections 1.4.4 and 2.4. We will compare measurements of junctions near x=0.125 doping, where PDW order is believed to be strongest, to a sample at x=0.155 doping, where the bulk T_c is at a maximum and PDW order is not expected to dominate (see Figure 4.1). Because our Josephson junctions do not have a measurable critical current until cooled to much lower temperatures than the bulk T_c, it is not realistic for us to measure a junction in the regime where the bulk T_c is suppressed completely, leaving behind only 2D superconducting order (10K<T<18K). In fact, our Nb electrodes (T_c≈9K) will not be be superconducting at all in this range.

We instead expect to observe a current-phase relation that is a superposition of a typical sin(ϕ) term, which corresponds to a typical Josephson current-phase relation caused by the bulk superconductivity, and an anomalous sin(2ϕ) term which would be caused by the presence of spatially varying 2D superconductivity within the CuO_2 planes, as predicted by the PDW model. Or in functional form, we should expect to measure a current-phase relation

$$I_c^{PDW}(\phi) = I_{c1}sin(\phi) + I_{c2}sin(\phi) \tag{4.1}$$

where the amplitudes I_{c1} and I_{c2} represent amplitudes of the conventional and anomalous (PDW) components of the current-phase relation. As temperature increases, we expect the fraction of Josephson current exhibiting a sin(2ϕ) current-phase relation $\frac{I_{c2}}{I_{c1}}$ to increase with T as the interlayer Josephson coupling and conventional 3D superconductivity are suppressed within LBCO, giving way to an increasing proportion of spatially varying 2D superconductivity within the CuO_2 planes. Likewise, we expect I_{c2} to have at most a negligible contribution to the CPR at dopings far from $x = 1/8$, due to the relative weakness of stripe order in this regime.

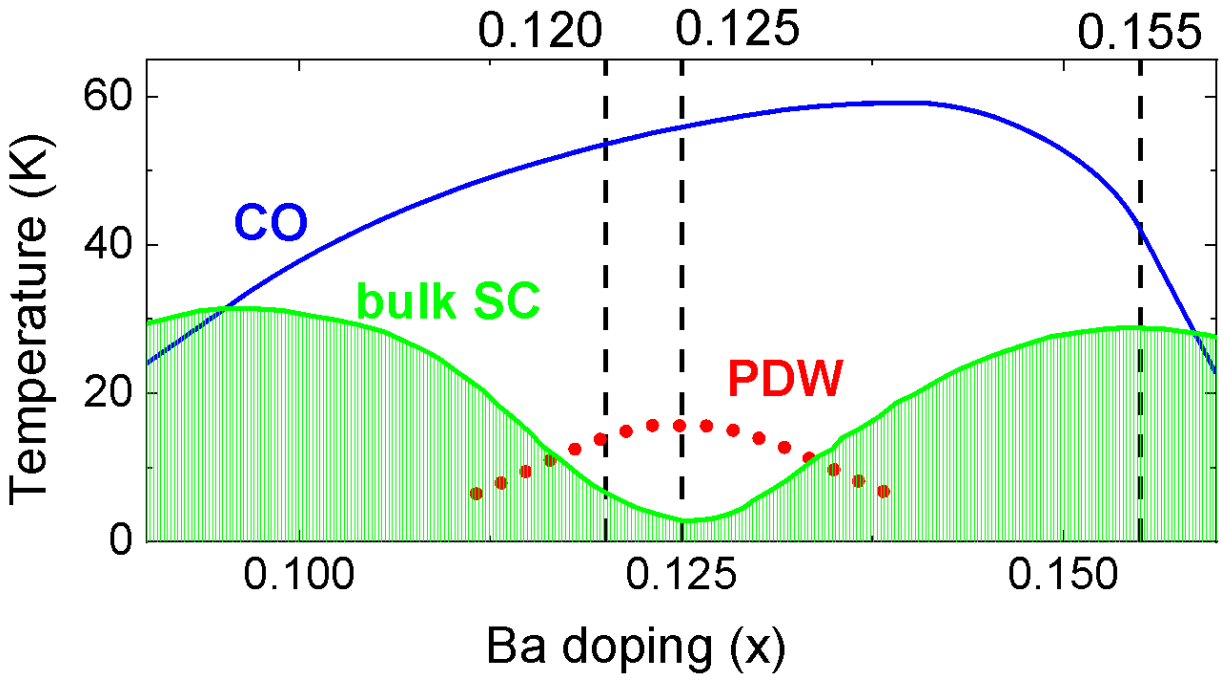

Figure 4.1: Phase diagram of LBCO, including observations of charge order and bulk superconductivity from [55], and the predicted region where PDW order is observable. Vertical lines indicate dopings of samples measured in this thesis.

4.1 Sample and junction characterization

In these experiments, we looked at crystals with three nominal dopings: x=0.120, x=0.125, and x=0.155. To verify the superconducting transition temperatures of these crystals, we performed susceptibility measurements in the Quantum Design Magnetic Property Measurement System (MPMS), a turnkey cryogenic system with a vibrating sample magnetometer (VSM). This system works by sending a uniform magnetic field through the sample as it its position rapidly oscillates, and measuring the voltage induced in a pickup coil according to Faraday's Law.[101] As a material undergoes a transition to the superconducting state, its measured magnetic moment should decrease due to Meissner screening effects.

Representative magnetization measurements are shown in Figure 4.2. Because the magnetic moment of these samples decreases continuously below T$\lesssim$30K, we define the bulk T_c as the temperature at which the magnetization drops to 1/e of its normal state value. This gives bulk T_c=6.75K, 11K and 28.75K for crystals with with nominal dopings x=0.125, x=0.120 and x=0.155, respectively. Note that although the x=0.155 sample drops sharply in magnetization in the vicinity of T_c, the magnetic moment of the x=1/8 sample drops by 8% at T=18K, the regime where 2D superconductivity is expected. This is in agreement with a similar two-step diamagnetic transition that was observed in LBCO at 1/8 doping in [102]. The x=0.120 sample sees a secondary transition in magnetism as well above T_c, where magnetization gradually drops by

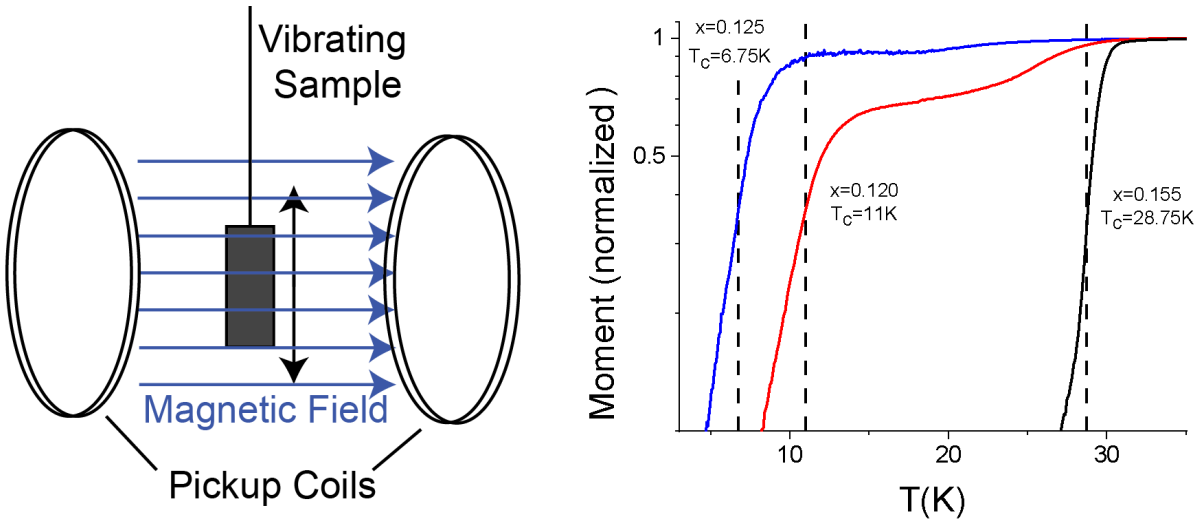

Figure 4.2: Left: Principle of operation of a vibrating sample magnetometer. Oscillating position of sample affects flux through the coils, creating a voltage which depends on the magnetic susceptibility of the sample. Right: Moment vs T of LBCO at x=0.125, x=0.120 and x=0.155 yields a T_c of 6.75K, 11K and 28.75K, respectively. Weak diamagnetism onsets above these temperatures, possibly due to superconducting fluctuations.

as much as 40% with temperature, at which before it begins to decline faster at T=15K. This may be due to the onset of superconducting fluctuations which take place above the bulk T_c.

These experiments rely heavily on the successful fabrication of Josephson junctions, and transport through a Josephson junction is well described by current-voltage characteristics. For instance, the critical current (I_c) of a Josephson junction would appear on an I-V characteristic as a significant finite current at zero voltage, and beyond this point it enters the normal state. In figure 4.3, we show the temperature dependence of the I-V and resistance curves of a LBCO-Au-Nb junction on a crystal at x=1/8 doping. Between T=1K to T=2.5K, the critical current falls from over 7μA to just above 1μA, at which point the I-V curve begins to appear noise-rounded. At T=1K, the I-V is discontinuous due to Fiske modes, which occur at voltages where the wavelength of the ac Josephson effect oscillation matches a physical length of the junction. [103] As we increase further in temperature, the drop in zero bias resistance due to the Josephson effect steadily decreases. The measured resistance increases considerably around T=6.5K, which can be attributed to a transition to the normal state in the LBCO bulk. Generally, we have observed that for these devices, the magnitude and onset temperature of the critical current in these junctions is not well correlated with the bulk T_c of the crystal, which may be much higher than the temperature at which a critical current can be measured. Instead, the strength of the critical current appears to be more sensitive to fabrication considerations such as variations in junction dimensions or annealing time.

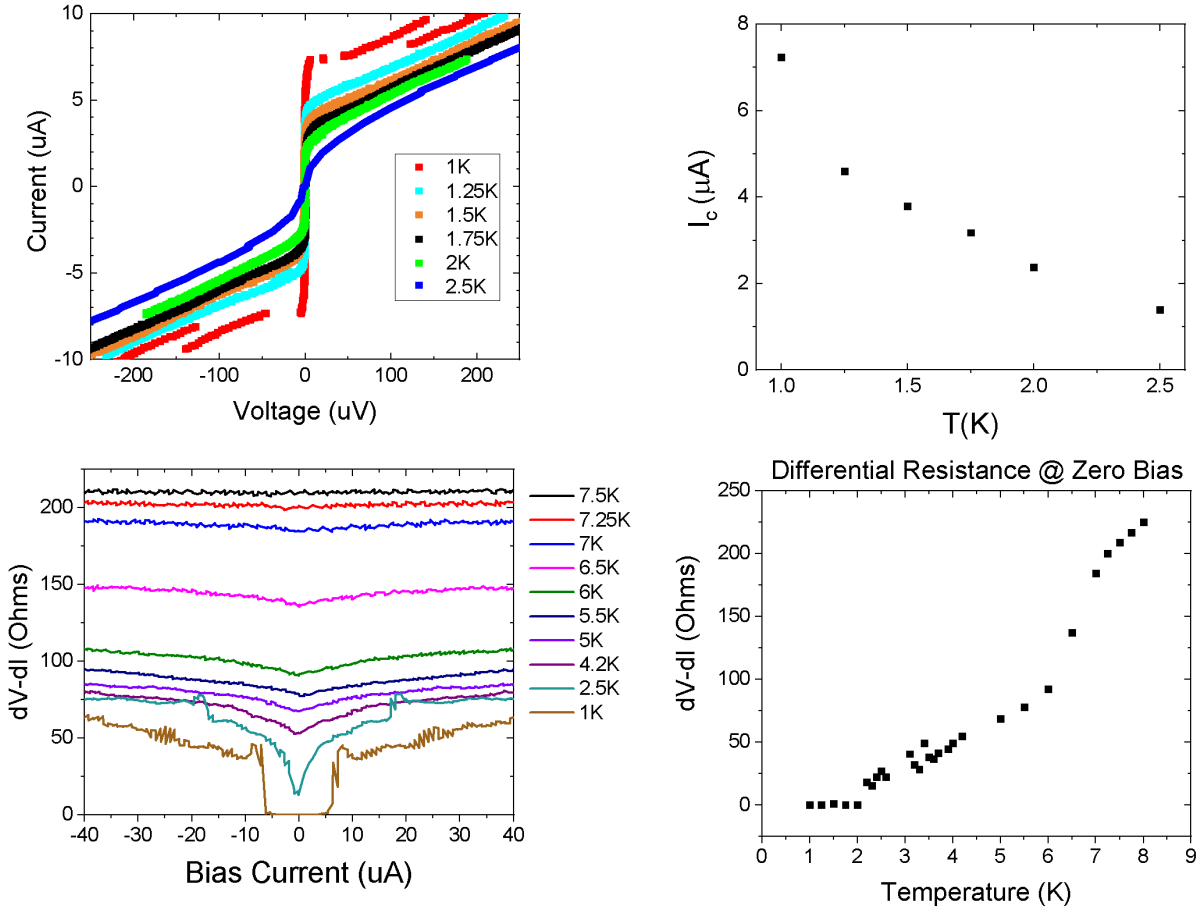

Figure 4.3: Top Left: Representative current-voltage characteristic vs T of an LBCO-Au-Nb Josephson junction on a crystal at x=0.125 doping. At T=1K, Fiske modes create discontinuities in the I-V curve. At 2.5K, noise begins to round out the measured supercurrent at zero voltage. Top right: Extracted I_c vs T. Bottom left: Measured differential resistance of the junction up to high bias current, high T. A large drop in normal state resistance occurs below 7K, possibly due to the junction's electrodes becoming superconducting. Below 4.2K, zero-bias resistance drops significantly compared to values at higher bias until a true zero-resistance Josepshon current is observed at 2K. Bottom right: Zero bias resistance vs T.

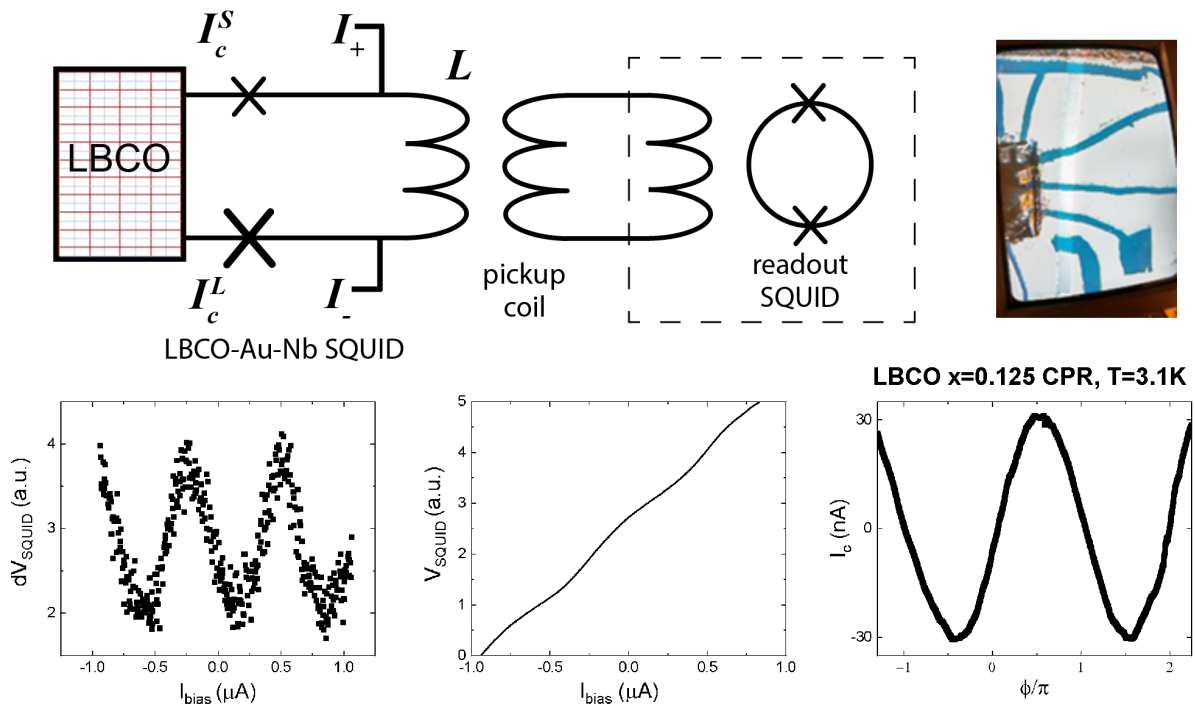

Figure 4.4: Top Left: Circuit to measure the CPR of an LBCO-Au-Nb JJ with critical current I_c^S. Compared to Figure 2.7, a large JJ with critical current I_c^L is used to complete the loop. The phase drop across the large junction can be neglected (see section 3.2). Top Right: Microscope camera image of sample for direct CPR measurement at x=1/8 doping. Bottom two leads are to pass bias current through the circuit, the remaining three are for transport measurements. A pickup loop connected to a commercial SQUID's input coil is placed directly above the on-chip washer inductance to measure the induced flux. Bottom Left: Lock-in measurement of derivative of SQUID response vs bias current. Bottom mid: Integrating dV_{SQUID}, we obtain the measured induced flux vs bias current. Bottom right: Exchanging axes and subtracting the linear contribution of the inductor, we extract the current-phase relation of the junction. Small deviations from a typical $\sin(\phi)$ CPR are visible.

4.2 Current-Phase Relation of LBCO-Au-Nb Josephson Junctions

4.2.1 Direct CPR measurement

Now that our samples have been shown to be superconducting, and that Josephson junction fabricated on them can carry a supercurrent, we move on to current phase relation measurements using using the method described in section 2.4.3. A diagram of the device itself and the CPR extraction method is shown in Figure 4.4. As discussed in section 3.2, an additional Josephson junction with large I_c is used to connect one arm of the inductor to the crystal, because a layer of annealed Au is needed to make contact. However, due to the asymmetry in critical currents, the phase drop across the larger junction can be neglected.

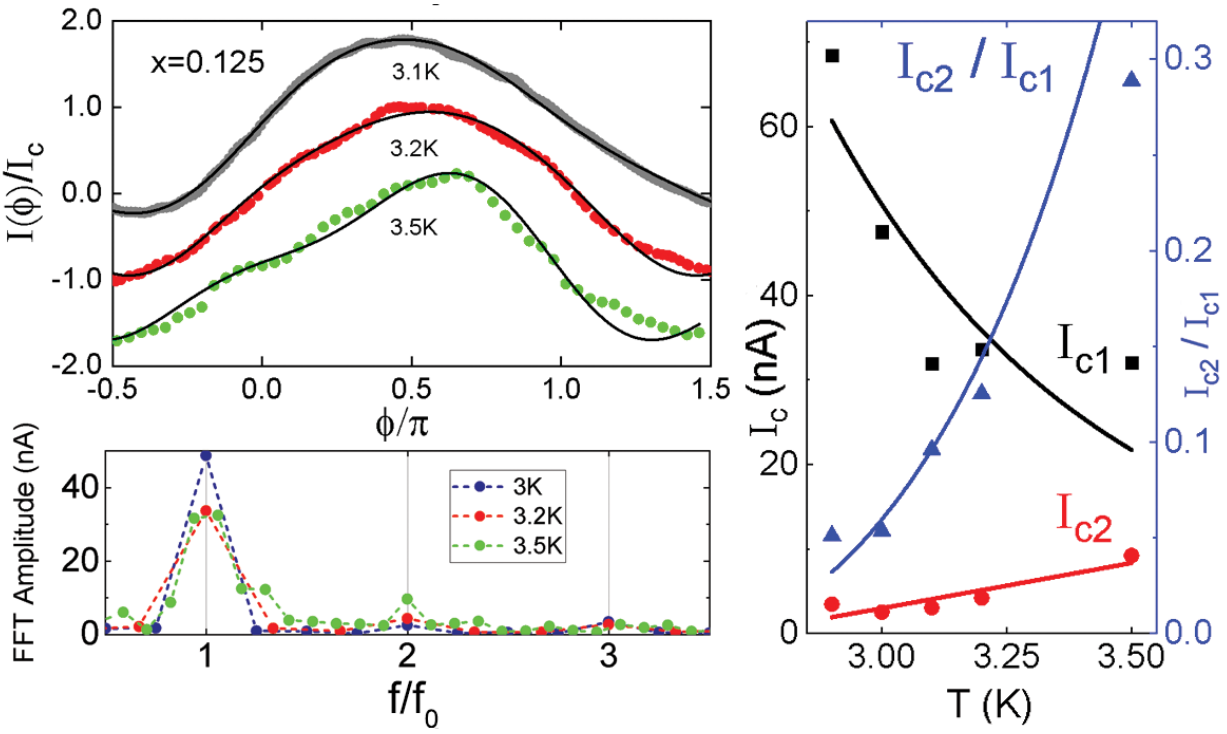

Figure 4.5: Top left: Normalized CPR measurements vs T at $x = 0.125$ doping, represented as points. The solid line is a fit of this data to a sum of sinusoids. At T increases, CPR deviates from typical $\sin(\phi)$ character. Bottom left: Fourier transforms of selected CPR curves reveal the strength of the 1^{st} and 2^{nd} harmonic amplitudes I_{c1} and I_{c2}. Right: Temperature dependence of I_{c1}, I_{c2} and $\frac{I_{c2}}{I_{c1}}$ from measured CPR curves. As I_{c1} is suppressed with increasing T, I_{c2} increases in strength.

Generally, the signal to noise ratio in these measurements was small enough to warrant using a lock-in amplifier to measure the SQUID voltage, which is proportional to the flux Φ induced in the inductor L. To extract the CPR, the lock-in signal, which corresponds to the derivative of Φ, is integrated with respect to applied bias current. This yields a plot analogous to the Φ vs I_{bias} curve shown in Fig. 2.7, which contains a linear response due to the inductance L and an oscillating term due to the junction's current-phase relation. After exchanging axes such that current becomes the vertical axis, the linear term is subtracted to obtain the junction's current-phase relation. The Φ axis is rescaled in terms of ϕ based on the observed periodicity of the junction oscillations.

We now present measurements of the current-phase relation of these Josephson junctions as a function of temperature for samples at x=0.125 and x=0.155 doping. Amplitudes are normalized in these plots to emphasize changes in shape of the CPR curves as a function of T. A Fast Fourier Transform is also performed on each curve using Origin software in order to get a quantitative measure of the harmonic content of the CPR. In order to improve resolution of the FFT, some measured curves which contained only a small number of periods were repeated before taking the Fourier transform.

For the 0.125 sample, summarized in figure 4.5, we find that the harmonic amplitude I_{c1} associated with a conventional $\sin(\phi)$ current-phase relation becomes suppressed as T increases, as is typical for a Josephson junction. Below T≈2.9K, the critical current becomes high enough for the CPR circuit to enter the hysteretic regime, which introduces a backward skewness artifact to the CPR that increasingly dominates as T is decreased. Beyond 3.5K, I_c becomes small enough that a CPR can no longer be extracted due to the signal:noise ratio of the measurment. As I_{c1} becomes suppressed, we observe that the second harmonic amplitude I_{c2} increases in strength in the x=1/8 sample, such that the ratio $\frac{I_{c2}}{I_{c1}}$ increases with T to as high as 29% within the temperature range accessible to this experiment. In this regime, the measured CPR qualitatively deviates from a simple sinusoid, showing a plateau feature associated with a waveform with a significant $\sin(2\phi)$ component. From the fits, we can see that this $\sin(\phi)$ component appears to have opposite sign to the $\sin(\phi)$ component, which would agree with the prediction of [82].

We will now compare this result to measurements of a sample at x=0.155 doping, shown in figure 4.6. Although the bulk T_c of this sample is much higher, the critical current of this junction is significantly smaller, requiring measurement at lower temperatures (1-1.5K) to achieve an acceptable signal to noise ratio. We attribute this difference to sample fabrication variations: we annealed the $x = 1/8$ crystal for a longer time, causing more of the Au to diffuse through the poorly conducting surface layer of that crystal compared to the $x = 0.155$ crystal, thus improving coupling between the LBCO and the Nb film. In the x=0.155 sample, we see that the amplitude of I_{c1} still decreases with temperature, but I_{c2} does not appear

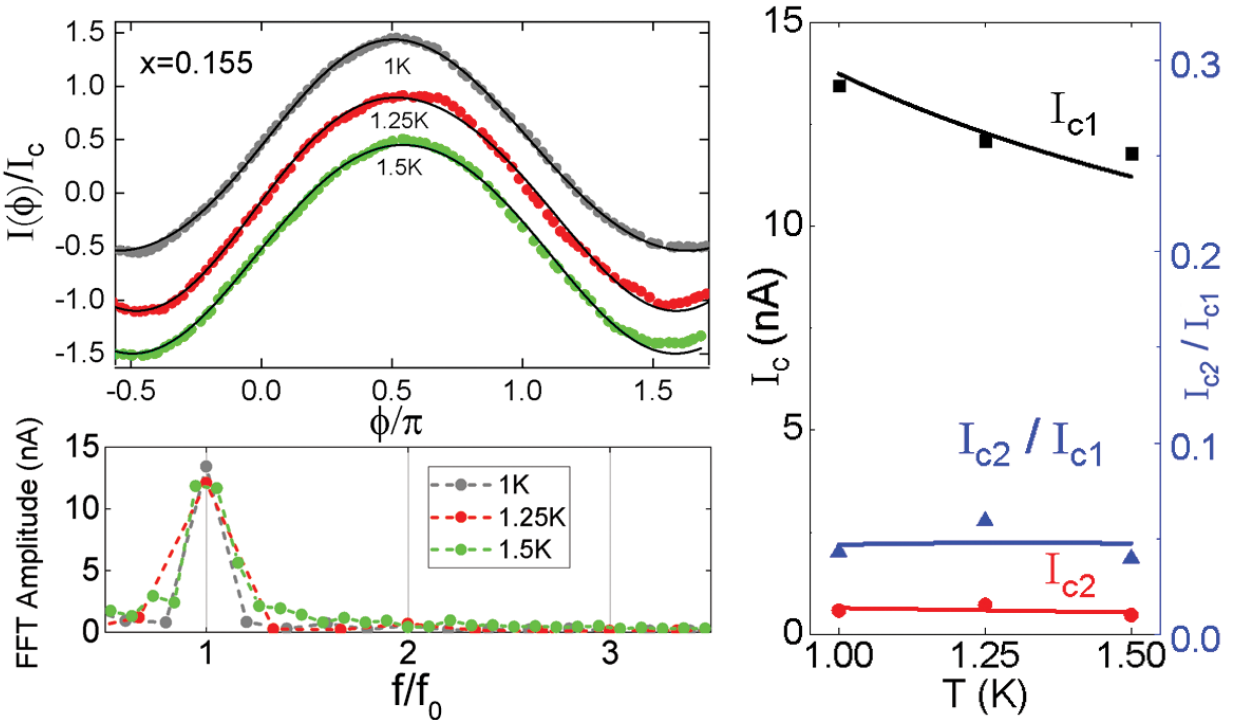

Figure 4.6: Top left: Normalized CPR measurements vs T at $x = 0.155$ doping. These appear dominated by the conventional $\sin(\phi)$ phase dependence. Bottom left: Fourier transforms of selected CPR curves, as in Figure 4.5. Right: Temperature dependence of I_{c1}, I_{c2} and $\frac{I_{c2}}{I_{c1}}$ from measured CPR curves. As I_{c1} is suppressed with increasing T, I_{c2} remains small and fairly constant.

to increase significantly as temperature increase, and is not easily distinguishable from noise in the FFT spectrum. The ratio $\frac{I_{c2}}{I_{c1}}$ remains fairly constant at about 5%. Qualitatively, the measured CPRs appear to be dominated by the conventional $\sin(\phi)$ component of the CPR.

From these measurements, it appears that the proportion of Josephson current with an anomalous $\sin(2\phi)$ CPR is strongest near 1/8 doping, and at temperatures where the conventional $\sin(\phi)$ component begins to vanish. The temperature dependence and doping dependence of $\frac{I_{c2}}{I_{c1}}$ is indicative of the presence of a superconducting state with a spatially varying phase which persists at temperatures where the bulk T_c is suppressed, such as in the pair-density wave model.

4.2.2 Asymmetric SQUID CPR measurements

To further study the CPR of these junctions, we will now compare the preceding results to CPR measurements obtained using the asymmetric SQUID technique discussed in 2.4.4. A diagram of such a device on an LBCO x=0.125 crystal is shown in Figure 4.7. In this sample, bias current was held at a fixed value I and voltage V across the junction was measured as magnet current Φ was varied. I_c of the SQUID was then

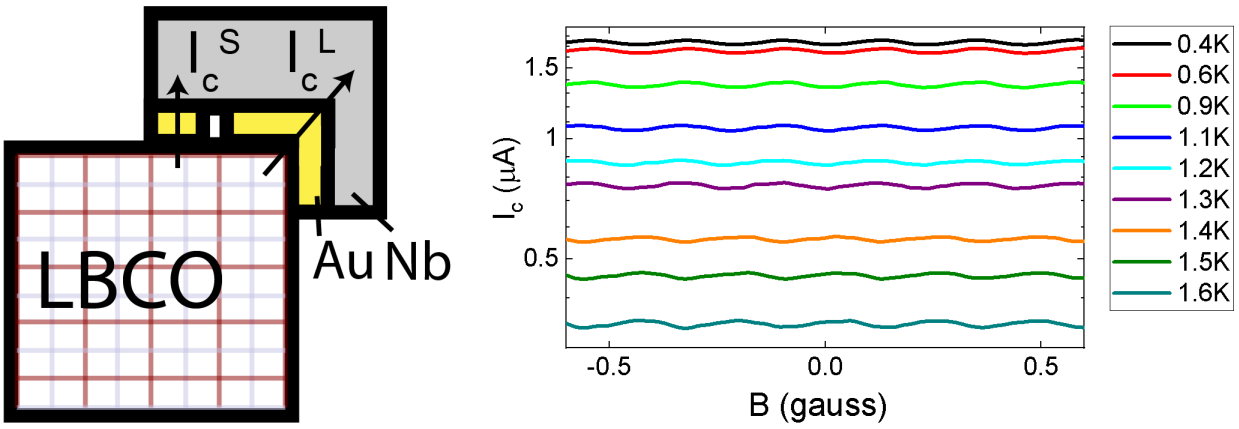

Figure 4.7: Left: Asymmetric SQUID fabricated on LBCO crystal at x=1/8 doping, such that $I_c^S >> I_c^L$. This enables measurement of the CPR of the small junction. Right: $I_c(\Phi)$ of the SQUID vs temperature, calculated via the RSJ model. Scale of current axis is logarithmic to improve visbility of high-T curves.

calculated using the resistively shunted junction (RSJ) approximation: [104]

$$V(\Phi) = \begin{cases} 0 & I \leq I_c \\ R\sqrt{I^2 - I_c(\Phi)^2} & I > I_c \end{cases} \tag{4.2}$$

which implies $I_c(\Phi) = \sqrt{\frac{V(\Phi)}{R} - I^2} = I^L(\phi) + I^S(\phi)$ for $I > I_c$. Measurements of $I_c(\Phi)$ vs T obtained in this measurement are shown in figure 4.7. Per the discussion in section 2.4.4, the asymmetry of the junctions allows us to extract the current-phase relation of the small junction $I^S(\phi)$ by subtracting $I^L(\phi_L)$, which is approximately constant at its maximum value I_c^L.

Then for a sample at x=1/8 doping, we perform a subtraction of I_c^L to obtain the current-phase relation $I^S(\phi)$, plotted in figure 4.8. These plots were Fourier filtered to reduce the contribution of low-frequency drift and high-frequency noise, and adjacent averaged smoothing was performed for visual clarity. Compared to the direct CPR method, it was possible to measure the CPR over more periods in a single sweep using this technique, which improved the frequency resolution of the FFTs of these curves. Additionally, the signal to noise ratio was favorable over a wider temperature range, allowing for CPRs to be extracted from 400mK-1.6K, above which point the critical current of the small junction was too small to measure.

As T increases in this sample, we observe that the temperature dependence of the first harmonic I_{c1} bears resemblance to an Ambegaokar-Baratoff curve rather than an exponent, increasing as T decreases but leveling off at a maximum value. [105] It's possible that a similar temperature dependence was present in the direct CPR samples, but was not observable due to the distortion of the CPR at high critical currents.

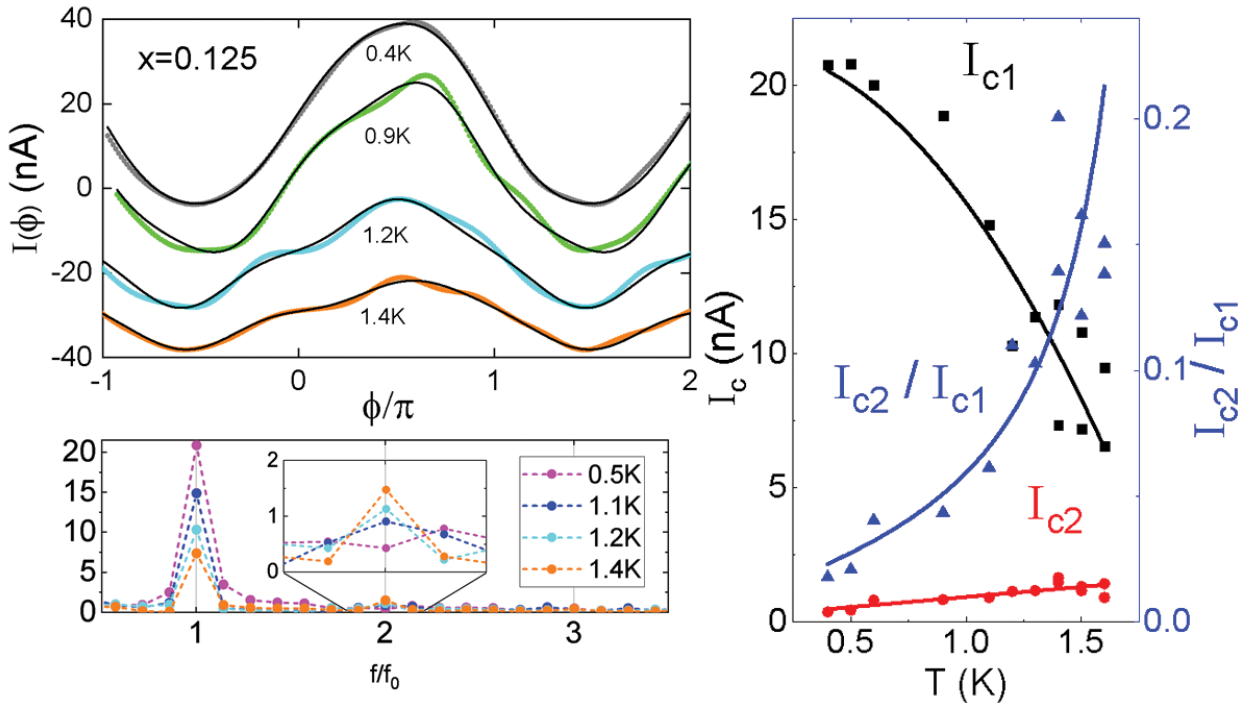

Figure 4.8: Top left: CPR extracted via subtraction of constant I_{c1} from figure 4.7. Deviations from $\sin(\phi)$ behavior strengthen as T increases, as in figure 4.5. Bottom left: Fourier transforms of selected CPR curves to show their harmonic content. Right: Temperature dependence of I_{c1}, I_{c2} and $\frac{I_{c2}}{I_{c1}}$. $\frac{I_{c2}}{I_{c1}}$ increases with T. Black line is a fit to Ambegaokar-Baratov temperature dependence.

Meanwhile, the magnitude of a second harmonic I_{c2} of the current-phase relation trends upward with increasing temperature, to as high as 20% of I_{c1}. The qualitative shape of the CPR again deviates from sinusoidal at these temperatures, with pronounced plateaus due to $\sin(2\phi)$ periodicity. Hence, we have again measured an anomalous $\sin(2\phi)$ component current-phase relation which begins to dominate in the the regime where $\sin(\phi)$ is suppressed, as we saw in the direct CPR sample at x=1/8 doping.

We also attempted to measure the CPR of an x=0.120 sample using the Asymmetric SQUID technique. In this case, $I_c(\Phi)$ was measured using a PID feedback technique, in which the measured resistance was compared to a set point associated with a transition to the superconducting state, and the bias current was adjusted automatically until the set point was reached. This technique was preferred to the approach applied to the x=1/8 sample due to the relatively low normal state resistance of the x=0.120 sample, which caused measurements of $V(\Phi)$ to have fairly poor resolution. These results, shown in Figure 4.9, were less conclusive, because the measured $I_c(\Phi)$ contain both a fast-period oscillation due to the SQUID and an envelope due to single-junction modulation, which implies that the fabricated junctions may have had too large of a cross-sectional area compared to the SQUID loop dimension. Additionally, flux trapping seems to offset $I_c(\Phi)$ significantly along the flux axis: repeated measurements after thermal cycling show the SQUID

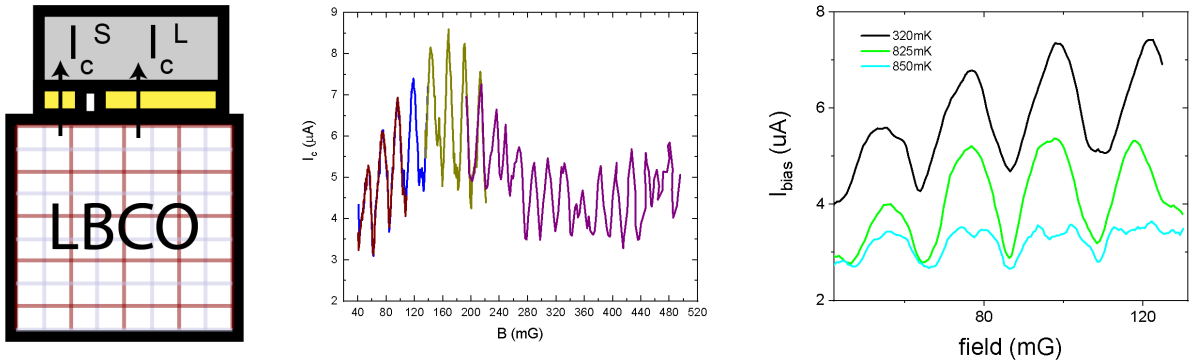

Figure 4.9: Left: Schematic picture of an Asymmetric SQUID fabricated on a crystal of x=0.120 doping. Mid: Multiple measurements of $I_c(\Phi)$. Thermal cycling alters the flux trapped in the SQUID loop, generating an offset in $I_c(\Phi)$. This effectively shifts the measured SQUID oscillations about the single-junction modulation envelope. This makes it difficult to obtain information about the current-phase relation from these measurements. Right: Temperature dependence of SQUID oscillations shows some evidence of period halving at temperatures where I_c begins to vanish, which could be evidence of a $\sin(2\phi)$ component of the current-phase relation.

oscillations appear to shift randomly about the envelope for each cooldown. These complicated attempts to extract a CPR at x=0.120 doping, and quantitatively measure its harmonic content. Still, we do see that at temperatures close to where T_c disappears, period halving in the SQUID oscillations due to a residual $\sin(2\phi)$ harmonic of the current-phase relation appears to take place. This could tentatively provide some evidence for a spatially varying order parameter at dopings slightly removed from x=1/8, but further study would be needed to characterize this behavior at x=0.120 doping.

4.3 Pairing symmetry of LBCO

If we are to increase the field applied through the circuit in figure 4.7, we can see the effect of a single-junction envelope on the SQUID oscillations, as we observed for the x=0.120 crystal in figure 4.9. Recalling from section 2.3 that a Josephson junction on the corner of a d-wave superconductor would have a suppression of critical current at 0 field, observing such a feature in the single-junction envelope of this sample would support the view that superconductivity in LBCO, like other cuprate superconductors, has d-wave pairing symmetry.

In figure 4.10, we show a plot of $V(\Phi)$ for the asymmetric corner SQUID on an LBCO crystal with x=1/8 doping discussed earlier, with the applied field increased by a factor of 40. Adjacent averaging is used to smooth out the SQUID oscillations superposed on the single-junction envelope. From this data, we can see that $V(\Phi)$ has a local maximum at 0 field, which corresponds to a local minimum of the critical current that

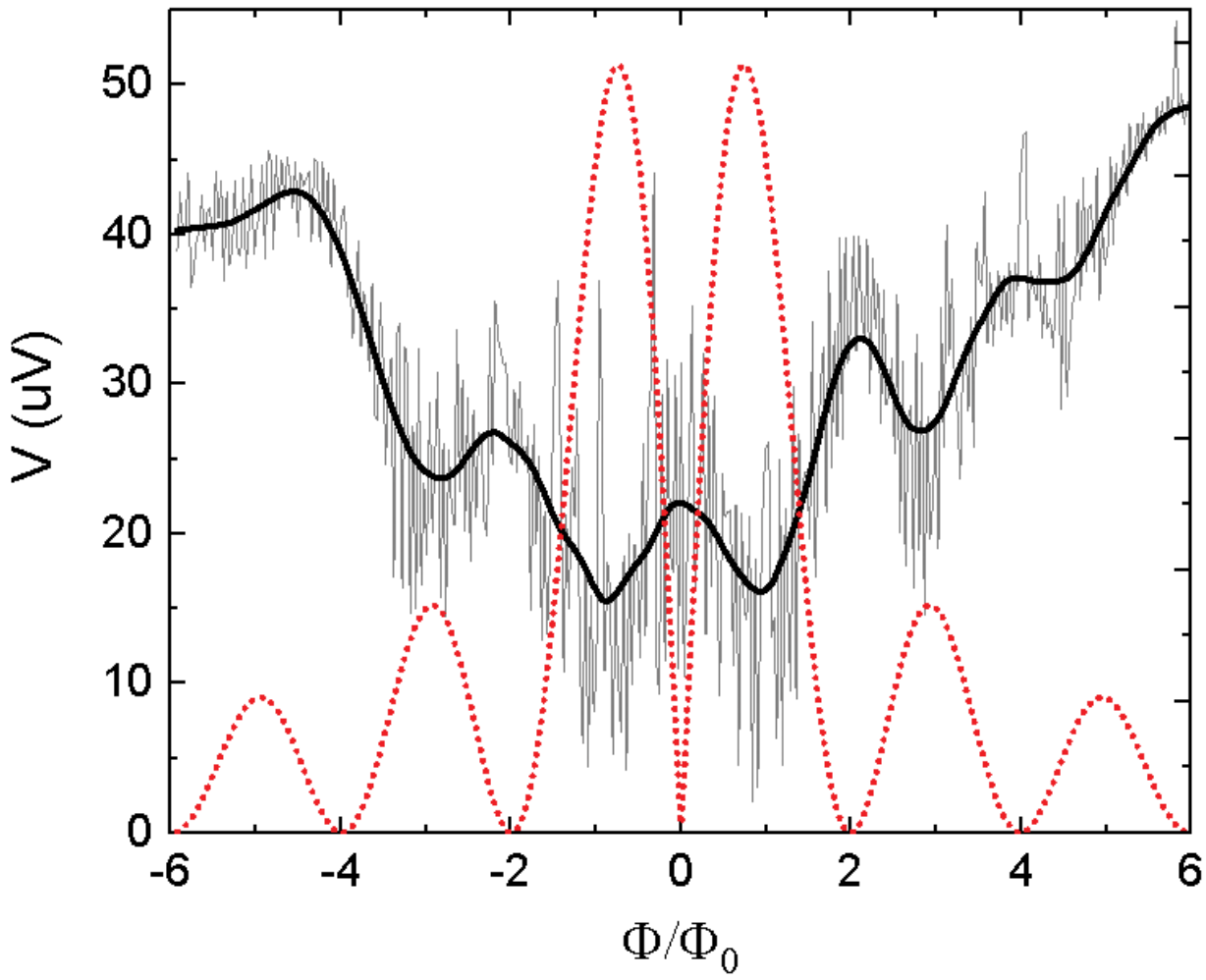

Figure 4.10: V(Φ) of device shown in 4.7, over a larger field scale. Smoothing out the fast SQUID oscillations, we see single junction effects. The minima in V (black curve) correspond to the local maxima in the theoretical Ic(Φ) (red dotted curve) for a symmetrical junction fabricated on the corner of a crystal with a d-wave pairing symmetry.

would occur due to a difference in sign of the critical current between the portion of the junction which lies along the a-face of the crystal, and the portion along the b-face. Hence, the single-junction modulation patter of our corner SQUID device appears to indicate that superconductivity in LBCO has d-wave symmetry.

4.4 Conclusions

We have measured the current-phase relation of LBCO-Au-Nb crystals at x=0.120, x=0.125, x=0.155 doping. At x=1/8 doping, we used two independent measurement techniques to observe the onset of a significant, anomalous sin(2ϕ) component of the CPR which becomes stronger relative to the conventional sin(ϕ) com-

ponent as T increases. This phase-sensitive measurement indicates that as T increases, a larger proportion of the superconductivity in the crystal is carried by a state where the superconducting order parameter is spatially modulated, consistent with the PDW state. In the x=0.155 sample, we saw a relatively small second harmonic of the CPR which does not increase significantly with temperature, is consistent with the PDW state weakening away from x = 1/8 doping. At x=0.120 doping, we saw some signs of this component as well, but the results were less conclusive due to experimental complications. Finally, by increasing the applied field to the corner SQUID device at x=1/8 doping, we observed a single junction modulating consistent with $d_{x^2y^2}$ pairing symmetry. The observation of the $\sin(2\phi)$ component in the Josephson current and its temperature dependence gives strong support to the proposal of [65] that LBCO at x = 1/8 doping harbors a PDW state, in which charge, spin and superconducting order are intertwined.

Chapter 5

Josephson interferometry measurements of the superconducting pairing symmetry in overdoped LSCO

In this chapter, we will use Josephson interferometry techniques to search for disorder-induced deviations from d-wave symmetry in the strongly overdoped regime of the cuprate superconductor LSCO. As we discussed in section 1.4.2, a disordered d-wave superconductor in the vicinity of a superconductor-to-normal transition has been predicted to feature a spatially inhomogeneous superconducting state localized to discrete "puddles" coupled together by the Josephson effect. A consequence of this model, described in greater detail in [52], is that as disorder is increased, the puddles become more dilute, and coupling between puddles will favor a state with global s-wave symmetry, even though the superconducting order parameter within each puddle will locally have d-wave symmetry.

We will test this prediction through performing pairing symmetry measurements of LSCO crystal samples at x=0.25 doping. At this doping, superconductivity is still present up to a a bulk T_c of 18K, but we expect the effect of disorder to be much higher than at optimal (x=0.15) doping due to the greater concentration of randomly arranged Sr dopants in the lattice. To measure the pairing symmetry, will apply the methods described in section 2.3 to measure the $I_c(\Phi)$ diffraction pattern of LSCO-Au-Nb Josephson junctions formed on edges and corners of the crystal. We will then compare these results to simulated $I_c(\Phi)$ of junctions formed over several puddle regions of random size and orientation.

5.1 Pairing symmetry measurements

Following the crystal junction fabrication procedures detailed in Chapter 3, we deposited junctions on crystals of LSCO at x=0.25 doping, such that one junction lies on the corner intersecting the polished a- and b- facets, and the remaining area along these facets is used to create edge junctions. Current-voltage characteristics are then measured for each junction under a fixed applied magnetic flux Φ in the four-terminal configuration detailed in section 3.3. Of the junctions produced on three x=0.25 crystals, we were able to measure one corner and one edge junction which had a measurable critical current that modulated significantly with applied magnetic field. Representative I-V curves are shown in Figure 5.2. The critical currents of these

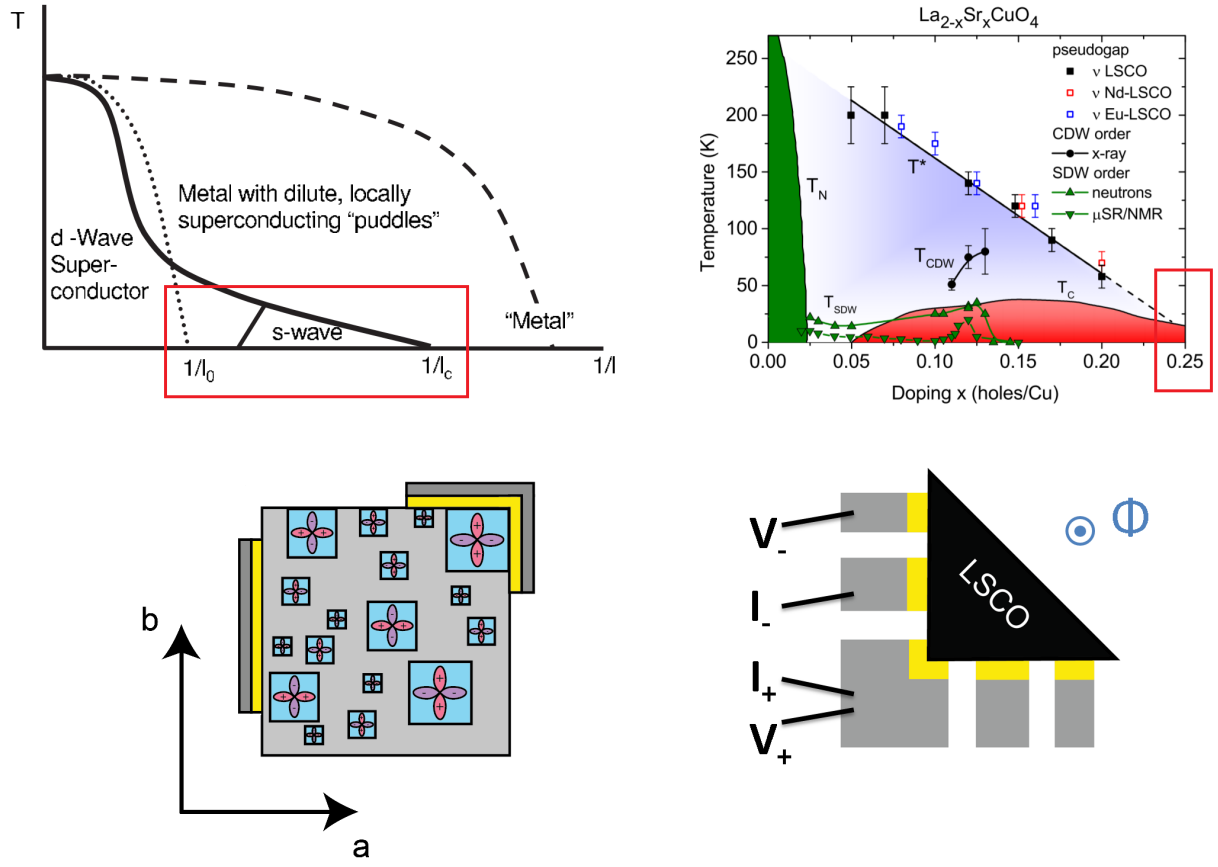

Figure 5.1: Top left: Evolution of pairing symmetry as a function of T and disorder, from [52]. With sufficient disorder, coupling between puddles is predicted to appear globally s-wave. Top right: Phase diagram of LSCO, from [106]. Samples measured in this experiment were at x=0.25 doping. Bottom left: cartoon picture of corner and edge junctions fabricated on a disordered d-wave superconductor. Each junction spans several puddles of random size and orientation. Bottom right: Diagram of typical sample, with one corner junction and multiple edge junctions. I-V characteristics were obtained using a four-terminal method, as shown.

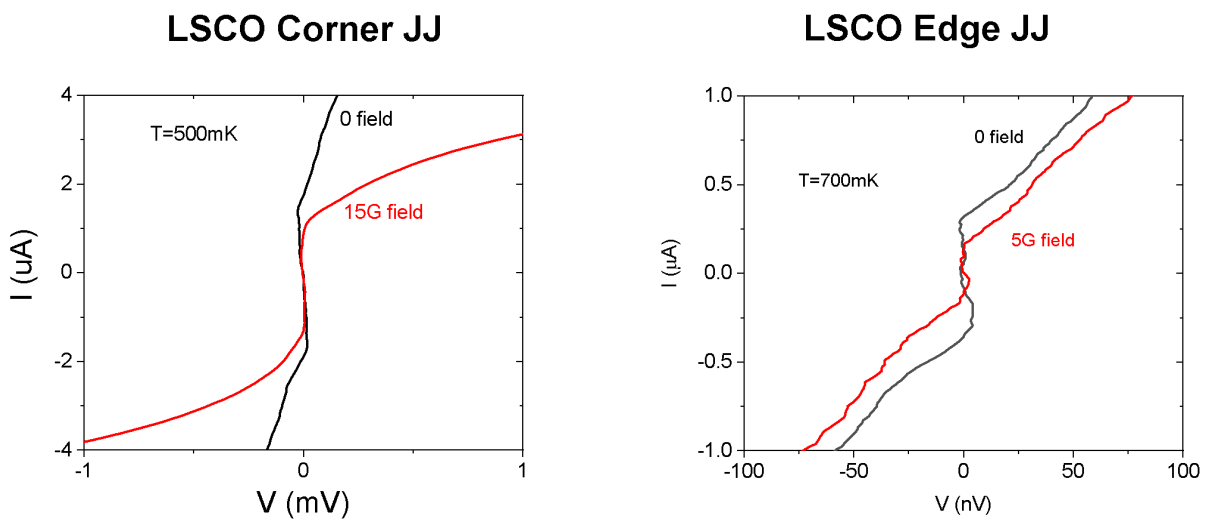

Figure 5.2: Current-voltage characteristics for corner JJ at T=500mK (left) and the edge JJ @ 700mK, showing modulation under an applied field. Both curves show an a slight backward tilt artifact due to amplifier drift, but the superconducting transition is clearly visible as a sharp change in dV-dI.

junctions are suppressed as temperature increases: I_c of the corner junction drops from roughly 2μA to 0.3μA between 400 and 700mK, while the edge junction drops from around 1μA to 0.2μA between 400 and 900mK.

To measure $I_c(\Phi)$, we recorded I-V curves at a few hundred values of applied flux, then compiled the results into a single contour plot, such that dVdI is the Z-axis and I_c can be observed within a contour of zero resistance. Field is limited to below ≈ 13 gauss so that resistance in the magnet connections does not generate unwanted sample heating.

For the corner junction summarized in figure 5.3 we find that at 800mK, a finite resistance is present, but is partially suppressed at low bias currents and applied fields. As temperature is reduced to 700mK, a critical current appears in the junction as the spatially separated superconducting domains nucleate and couple together via the Josephson effect. As T is decreased further, I_c is enhanced, the envelope of low resistance expands, and additional fast-periodic structure is visible in $I_c(\Phi)$. Further, the measured $I_c(\Phi)$ is not symmetric about zero field. This could be due to inhomogeneity in field over the junction dimensions caused by circulating currents between adjacent domains, which we will discuss in the next section.

In the edge junction shown in figure 5.4. we find that the observed $I_c(\Phi)$ diffraction patterns also display fast-periodic oscillations superposed with a large-field envelope and asymmetry about zero field. However, the overall character and horizontal offset of the measured $I_c(\Phi)$ changes noticeably after thermal cycling. In some measurements, I_c is maximized at zero field, as seen in a conventional Fraunhofer pattern of a homogeneous edge or s-wave corner junction. In other measurements I_c has a minimum at zero field flanked

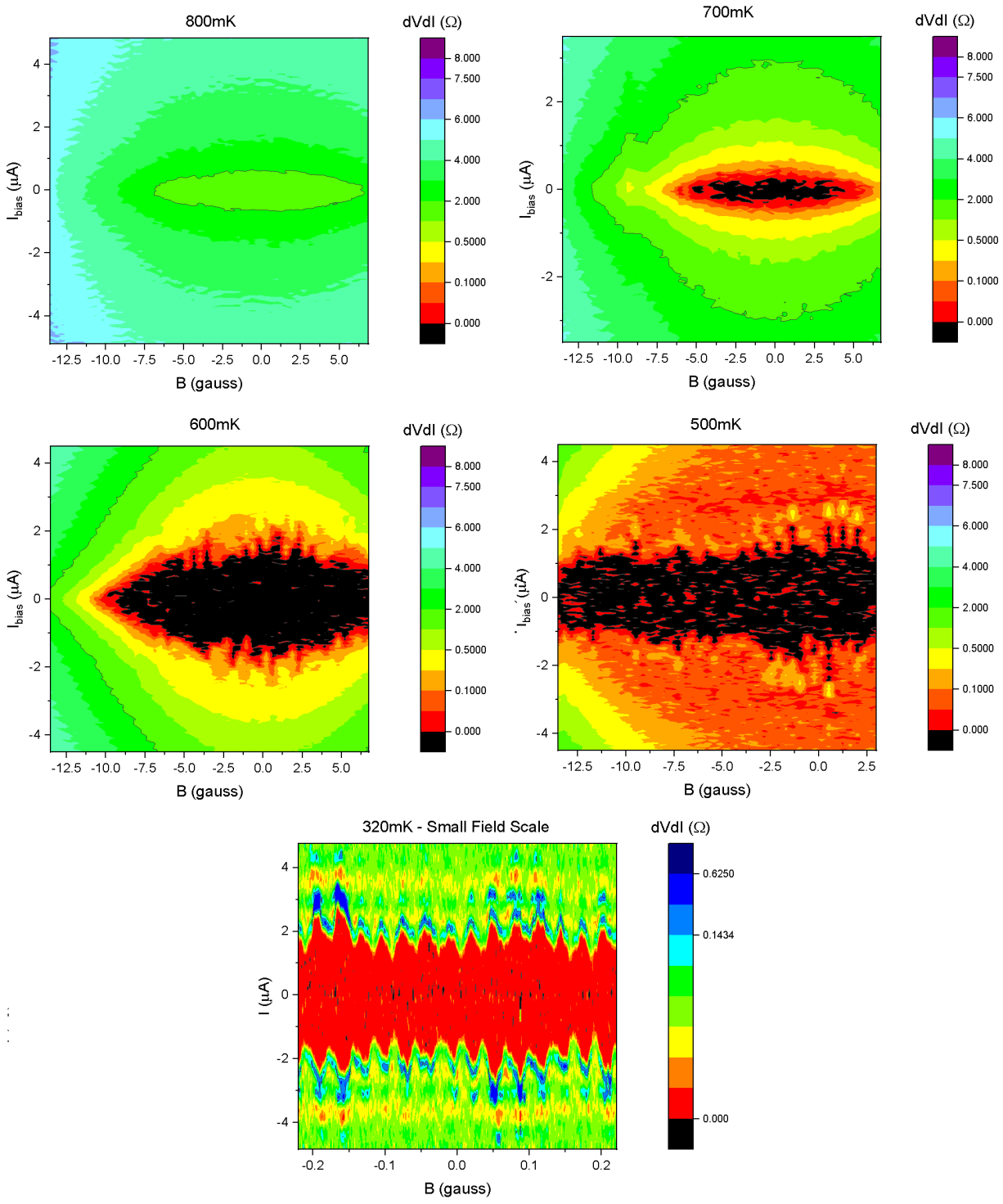

Figure 5.3: Color plot of bias current vs field vs resistance of overdoped LSCO corner junction at several temperatures. Top Left: At 800mK, resistance is still finite, but shows an I- and B- dependence. Top right: A supercurrent is now visible, with resistance gradually increasing above I_c. Mid left: Fast-periodic oscillations in I_c appear in addition to the overall envelope. Mid right: I_c oscillates about a steady value for larger values of field. Hints of the overall envelope are seen at this field range. Bottom: Small field scale measurement highlights fast-periodic oscillations in I_c.

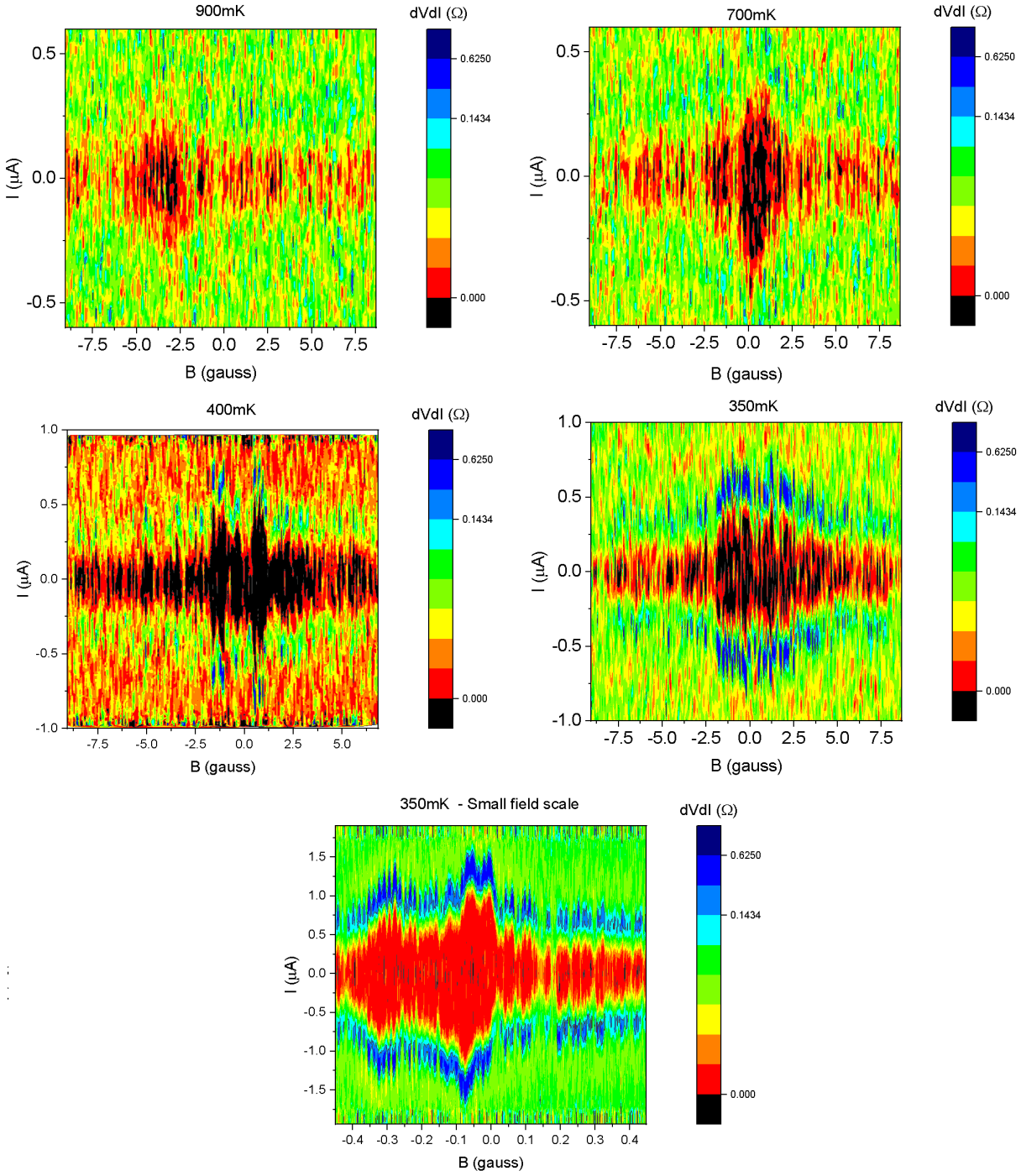

Figure 5.4: Bias current vs field vs resistance of overdoped LSCO edge JJ at multiple values of T. Top: Noisy, modulating supercurrents visible at 900 and 700mK. Lower normal state resistance of this sample lessens resolution of these plots. Mid left: Twin maxima in I_c observed about 0 field, similar to a corner d-wave junction's Fraunhofer pattern. Mid right: At low T, fast oscillations significantly affect the behavior of I_c. Bottom: Small field scale plot shows fast oscillations, field asymmetry.

by maxima, as in a d-wave corner junction. This can likely be explained by changes in the distribution of superconducting domains which occur during thermal cycling. In the next section, will employ simulations to help explain the field dependence of the critical current in both edge and corner junctions.

5.2 Simulated $I_c(\Phi)$ of junctions incorporating a disordered d-wave superconductor

Both junctions measured in the preceding segment have diffraction patterns which deviate significantly from either the Fraunhofer-like field dependence of a typical Josephson junction or the characteristic behavior of a d-wave corner junction seen in section 2.3. To understand these observations, we will consider a hypothetical Josephson junction fabricated on a material containing multiple superconducting domains of irregular size, separated by normal regions. To define these random domains, the junction length is divided into N regions of random size, such that which half are superconducting (constant, finite order parameter) and half are normal (zero order parameter). Per the theoretical discussion in [52], each domain will be oriented such that the order parameter in the direction of a crystal axis will carry a positive or negative sign, which will affect the sign of the critical current passing through that segment of the junction. The order parameter in each superconducting region is then assigned a positive or negative sign at random. The proximity effect should additionally yield an exponentially decaying fraction of the order parameter penetrating into the normal region over a length scale y_p. Hence in general terms,

$$OP(y) = \begin{cases} 1 & y \in y_+ \\ -1 & y \in y_- \\ OP_L^{edge} e^{-\frac{|(y-y_L^{edge}|}{y_p}} + OP_R^{edge} e^{-\frac{|(y-y_R^{edge}|}{y_p}} & y \notin y_\pm \end{cases} \tag{5.1}$$

where y$\in y_\pm$ denotes regions in y assigned a positive or negative order parameter and $\mathrm{OP}_{L,R}^{edge}$ gives the values of OP at the superconductor-normal boundary positions $\mathrm{y}_{L,R}^{edge}$ at either end of a normal region. To simulate a corner junction, we simply introduce a sign change in OP(y) over the corner position, as shown in figure 5.5.

Setting j_c and the junction dimension c to unity, for a range of uniform applied flux Φ we can then calculate

$$I_c(\Phi) = \max_{wrt\ \phi_0} \left(\int_0^w OP(y) sin(\phi_0 + \frac{2\pi\Phi\frac{y}{w}}{\Phi_0} dy \right) \tag{5.2}$$

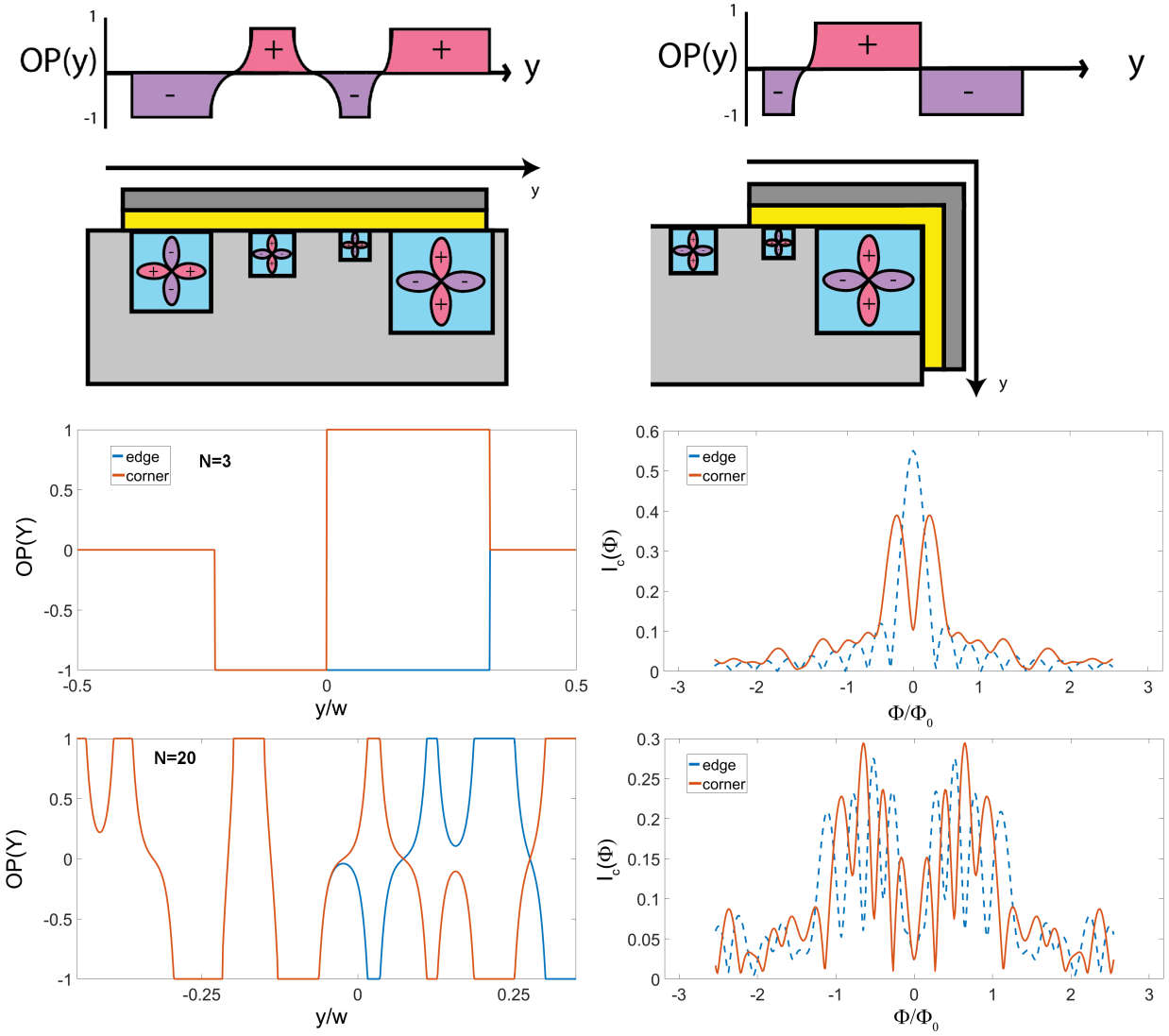

Figure 5.5: Top left: Illustration of order parameter as a function of position across an edge junction. Sign of OP depends on the orientation of the superconducting grain's d-wave order parameter. Normal regions include an exponentially decaying portion of OP due to the proximity effect. Top right: Corner junction experiences a sign change of the order parameter at the corner position. Mid left: Order parameter as a function of position for N=3 domains. Orange curve denotes a corner junction, in which OP sees a sign change across the corner position (y=0). Bottom left: As above, but for N=20 domains. Mid right: Calculated diffraction patterns based on the given OP(y) for N=3 bears resemblance to junctions on a uniform d-wave superconductor. Bottom right: N=20 case is similar to the diffraction pattern of a YBCO grain boundary junction.

Example OP(y) and diffraction patterns calculated for corner and edge junctions in Figure 5.5 for N=3 and N=20 domains. In the limit of few domains, $I_c(\Phi)$ bears qualitative resemblance to $I_c(\Phi)$ of an edge or asymmetric corner junction on a uniform d-wave superconductor. As the number of domains increases, we observe a combination of fast periodic oscillations in I_c combined with a large scale envelope, similar to our experimental observations from the previous section. This calculated $I_c(\Phi)$ resembles the field dependence of a grain boundary junction, in which the order parameter changes sign multiple times over the junction area.[107]

However, this calculation notably does not reproduce the asymmetry about zero field we see in our data. To explain this, we consider the possibility of an inhomogeneous magnetic field over the junction area produced by circulating currents between d-wave grains. From [108], a system of three grains within a material composed of many superconducting islands can form a loop carrying a spontaneous current if the phase between each successive grain differs by π. This is referred to as the Wohlleben effect, or the paramagnetic Meissner effect. Such a configuration does not appear possible if each grain follows $d_{x^2-y^2}$ symmetry pinned to the crystal axes. However, if the order parameter contains a complex component with id_{xy} symmetry, this would enable a circulating current $I_{w.e.}$ to take place between two adjacent, oppositely oriented grains and a third grain within the bulk, as shown in Figure 5.6. To incorporate this phenomenon into our simulation, we introduce a field with magnitude $\pm B_{w.e.}$ between any two adjacent grains of opposite sign, and which vanishes everywhere else. Incorporating this spatial variation of Φ into our calculation of $I_c(\Phi)$ yields diffraction patterns with broken symmetry about Φ=0, as shown in figure 5.6

Because this calculation involves generating superconducting domains of random size and orientation, each calculated $I_c(\Phi)$ diffraction pattern is unique. Generally, these $I_c(\Phi)$ become suppressed after a few flux quanta, and oscillate over a faster field scale. However, in some curves I_c is suppressed at 0-field, and in others generated with the same parameters, I_c is at a maximum. Further, in calculations involving some domain structures, both corner and edge junctions exhibit a suppression or maximum at zero field, and in others, these two cases diverge.

In order to better understand this behavior, we performed a statistical study of I_c at zero field over 100 sets of generated domains, shown in figure 5.7. When the number of domains is small (N=3), the values of $I_c(0)$ of the corner and edge junction together form a bimodal distribution, with curves centered at the mean values of 0.15 and 0.35, respectively, where 1 is the maximum possible value of I_c. In this limit, $I_c(\Phi)$ will tend to be similar to the diffraction pattern of a junction on a uniform d-wave material, in the sense that on average, the measured $I_c(0)$ of the corner junction would be smaller compared to the edge junction. In contrast, when the number of domains is large, the two distributions converge, centered around an $I_c(0)$ of

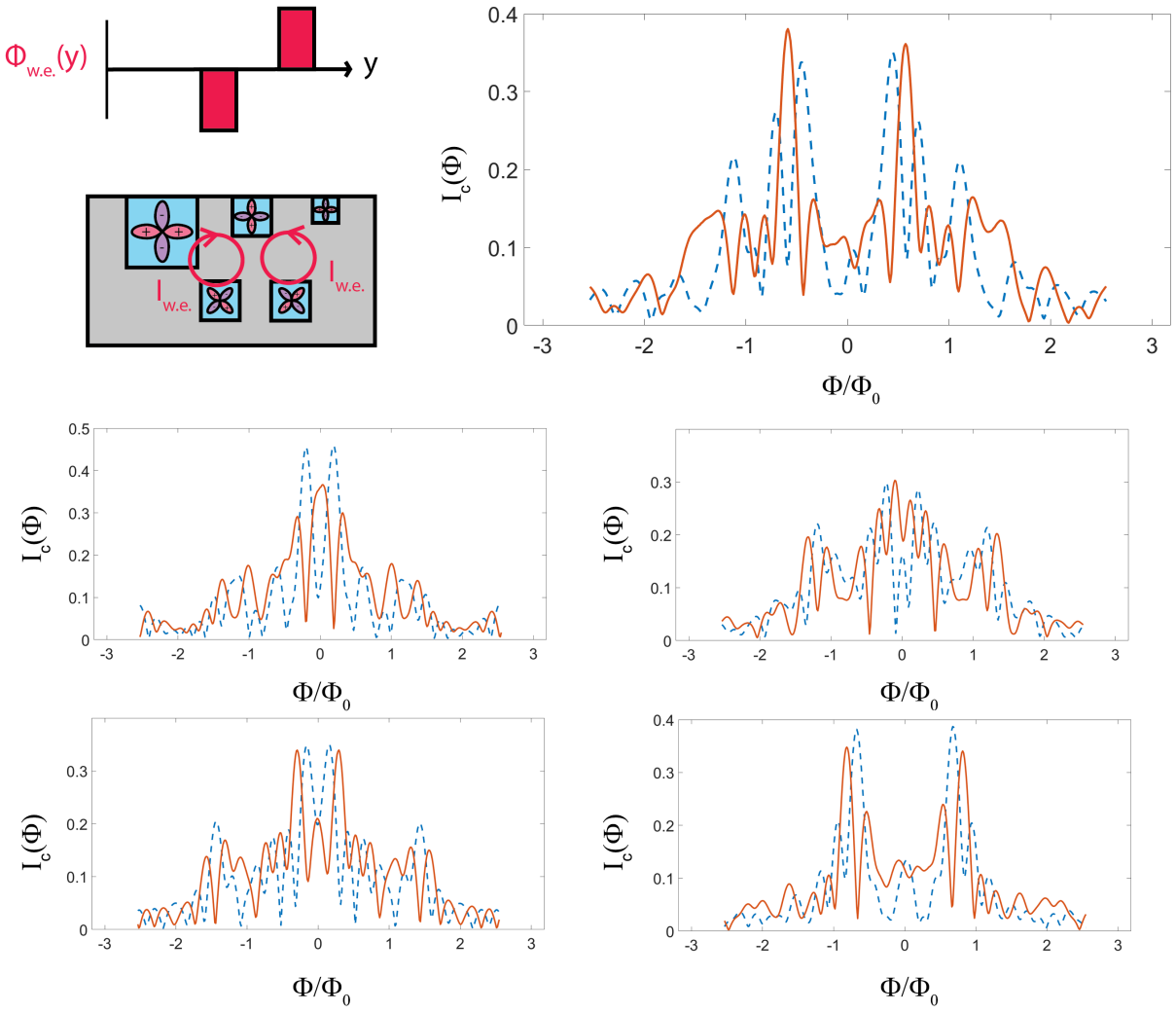

Figure 5.6: Top left: If a complex id_{xy} component of the order parameter exists, circulating currents can develop between adjacent oppositely-aligned puddles of d-wave superconductivity, creating induced fields at these locations. Top right: Calculated $I_c(\Phi)$ for N=20 domains that include these inhomogeneous fields are no longer symmetric about Φ=0. As before, the blue curve is calculated for an edge junction and the orange curve is for a corner junction. Bottom: Four additional curves calculated using the same sets of parameters as above. We see that $I_c(\Phi)$ can vary depending on the randomly generated domain structure.

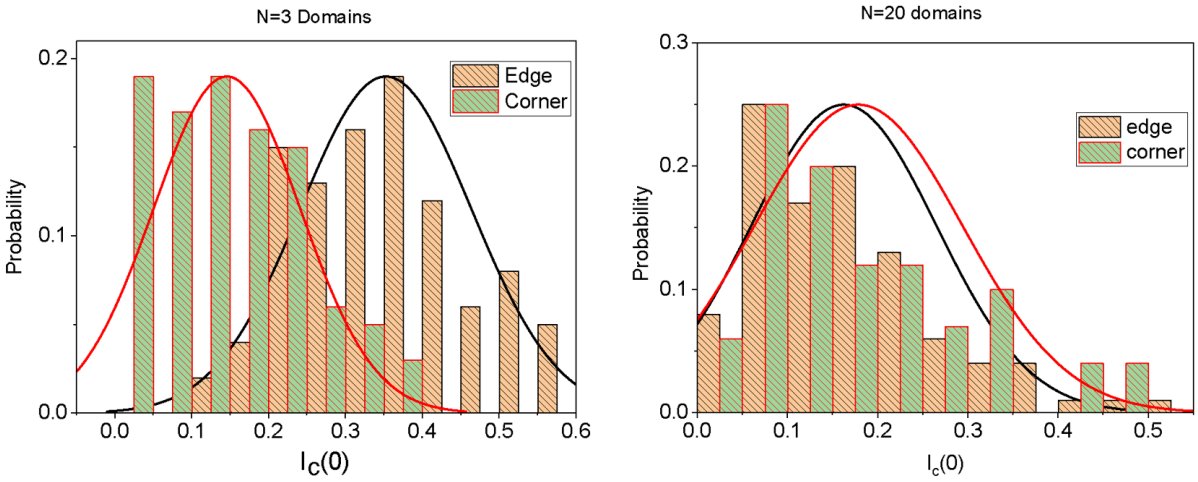

Figure 5.7: Statistical distribution of $I_c(0)$ values generated in the preceding simulations for N=3 (left) and N=20 (right) domains, after 100 simulations each. For N=3, there is a clear offset between the two distributions for corner and edge junctions. At N=20, the distributions converge, centered about a shared mean value.

roughly 0.16. Additionally, as the number of domains increases, the probability of $I_c(0)$ being close to zero increases as well.

5.3 Conclusions

In order to test the prediction in [52] that a disordered d-wave superconductor will appear globally s-wave near criticality, we have used Josephson interferometry techniques to measure the pairing symmetry of LESCO crystals at x=0.25 doping. Instead of observing the characteristic diffraction patterns we would expect to see in junctions with uniform s- or d-wave pairing symmetry, we measured irregular $I_c(\Phi)$ curves in both a corner and an edge junction which oscillate and decay with field, appear asymmetric about zero field, and change significantly upon thermal cycling. We were able to qualitatively reproduce the behavior of $I_c(\Phi)$ in a simulation which considers LSCO as a granular superconductor containing proximity coupled superconducting regions of random size and orientation. In order to explain the field asymmetry, we introduced an inhomogeneous field to our calculation arising due to circulating currents explained by the Wohlleben effect. This in turn would imply the existence of an additional component of the order parameter which does not point along the crystal axis directions, such as a complex id_{xy} term. Variations in the diffraction pattern upon thermal cycling appear to be the result of changing the structure of the superconducting domains across the junction, which also produces significant changes between repeated simulations. These simulations also tell us that for a large number of domains, it becomes difficult to distinguish an edge junction from a corner

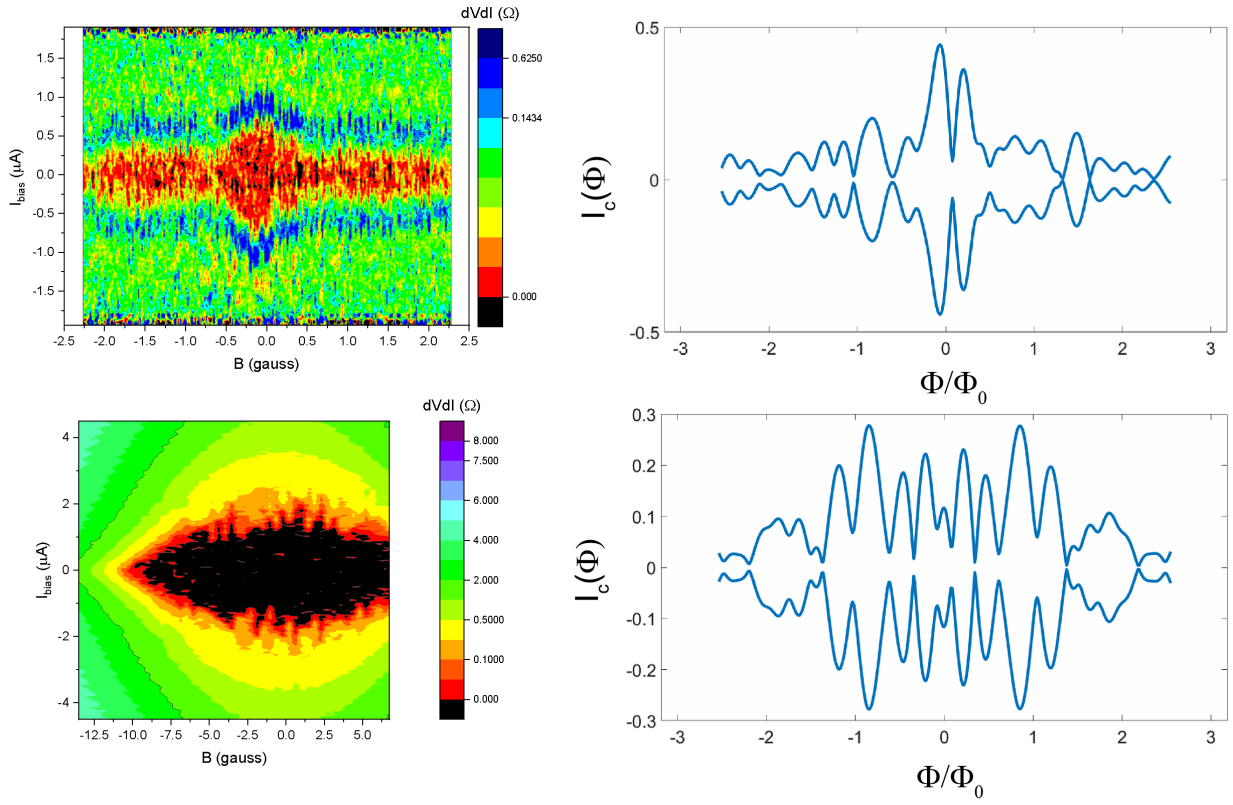

Figure 5.8: Comparison of experimentally measured $I_c(\Phi)$ (left) and similar result generated from a random domain structure (right) for both an edge (top) and corner junction (bottom). Bottom simulated curves in the right-hand figures are found by minimizing I_c wrt ϕ_0, rather than maximizing.

junction. Perhaps this indistinguishability is actually a characteristic of globally s-wave coupling between puddles in the regime, in the sense that diffraction patterns measured on corner and edge junctions on a uniform s-wave superconductor are not distinguishable from one another, either.

Hence, our measurements of LSCO at x=0.25 doping appear to be well described by a granular superconductor model containing circulating currents. However, the question of whether the overall pairing symmetry of the system can be considered s-wave is somewhat inconclusive. It would be useful to compare these Josephson interferometry measurements to equivalent data on crystals at smaller or larger dopings. We would expect junctions on optimally doped (x=0.15) samples to exhibit the field dependence of a typical d-wave superconductor, and for there to be a transition with increasing doping to a diffraction pattern resembling the present grain boundary junction-like behavior. Additionally, dopings even higher than x=0.25 would show us the effect of further diluting the concentration of superconducting grains on $I_c(\Phi)$, and perhaps yield wholly s-wave-like pairing. However, in this regime the superconducting volume fraction of these crystals becomes increasingly suppressed, which would further complicate the fabrication of Josephson junctions with significant I_c. [109]

Chapter 6

Conclusions and Future Work

We have fabricated Josephson junctions and SQUIDs onto single crystals of LBCO and LSCO in order to perform phase-sensitive measurements of the exotic superconducting states predicted to exist in these materials.

In Chapter 4, we measured the current-phase relation of LBCO-Au-Nb Josephson junctions in search of evidence for the pair-density wave state using two separate measurement circuits. At x=1/8 doping, we observe a significant $\sin(2\phi)$ component of the CPR which is strongest at high temperature, at the same time as the conventional $\sin(\phi)$ component is suppressed. The $\sin(2\phi)$ component is an experimental signature of rapid sign changes in the superconducting order parameter across the junction area, which in this case could be the spatially modulated phase predicted by the PDW model. The relative increase of $\frac{I_{c2}}{I_{c1}}$ with temperature is also consistent with the relative robustness of the two-dimensional superconducting transition in LBCO compared to bulk superconductivity.[63] Likewise, at x=0.155 doping, the bulk T_c is at a maximum and stripe order is relatively weak, the proportion of $\sin(2\phi)$ appears to be negligible compared to background noise in the sample we measured. Our x=0.120 sample also showed some evidence of a $\sin(2\phi)$ component, but due to flux trapping and single-junction effects we were not able to draw strong conclusions about its behavior. Together, these Josephson current-phase relation measurements support the conclusion that the anomalous 2D superconducting state in LBCO which persists above the bulk T_c is described by the the pair-density wave model.[65]

In Chapter 5, we fabricated and measured corner and edge Josephson junctions on single crystals of the disordered d-wave superconductor LSCO at x=0.25 doping, in order to learn more about the pairing symmetry of the heavily overdoped regime. Specifically, we sought to test the theory that superconductivity in this material near the d-wave superconductor to normal metal transition would nucleate in spatially separated puddles with d-wave symmetry coupled through the Josephson effect, and when those puddles are sufficiently dilute, the global symmetry of superconductivity in the material would appear s-wave.[52] Our measured $I_c(\Phi)$ of these junctions appeared similar to that of grain-boundary junction, despite the single-crystal nature of the LSCO sample. With the aid of simulations, we determined that these measured diffraction patterns

were consistent with a junction on a material carrying granular superconductivity, in addition to circulating currents between grains arising due to the Wohlleben effect. Changes in the structure of $I_c(\Phi)$ between thermal cycling were attributed to changes in the size, location and orientation of superconducting domains as the sample is warmed and cooled. Neither our measurements or simulations produced the characteristic Fraunhofer pattern that would be indicative of s-wave superconductivity, but our simulations seemed to indicate that in the many-domains regime, the diffraction pattern of a corner and edge junction were no longer easily distinguishable, as opposed to junctions on a uniformly d-wave superconductor. Naturally, we would like to compare the results at x=0.25 doping to a control sample at optimal doping, x=0.15. As of this writing, fabrication is underway on such a sample, to be measured in collaboration with Farzaneh Hoveyda.

To put these results in further context, it could be useful to perform more repeated measurements of these experiments and study these exotic superconducting effects over a wider range of doping. However, because these experiments involved studying superconductivity in the regime where superconductivity is disappearing, producing a junction with significant, modulating I_c often proved to be quite difficult, and the resulting yield was somewhat low. While the fabrication methods detailed in chapter 3 were able to successfully produce Josephson junctions on crystalline materials with arbitrary growth orientation and poorly conducting surface layers, the recipes for steps such as annealing and deposition could most likely be further innovated on to more reliably produce samples with the desired I_c.

Additionally, in terms of our search for PDW order, it would be of significant interest to measure the current-phase relation of the cuprate superconductor LESCO, another candidate for a PDW state. LESCO, like LBCO, sees coexistence of charge order, spin order, superconductivity and low temperature tetragonal crystal structure over part of its phase diagram. Additionally, ultrafast optical measurements of the material indicate a suppression of interlayer coupling in LESCO at x=1/8 doping, which is indicative of two-dimensional PDW superconductivity. [110] This is supported by recent susceptibility measurements by the Macdougall group that indicate stronger diamagnetism in the out-of-plane direction compared to the in-plane direction (Figure 6.1) at x=0.125 doping, and uniform behavior for x=0.15 doping, where stripe order is relatively weak.

To look for a similar anisotropy in resistive transport, we used the fabrication methods described in Chapter 3 to polish a single crystal of LESCO at x=1/8 doping such that the a- and c- axes lay parallel to the plane of the substrate, and compared the four-point resistivity in the in-plane and out-of-plane directions as a function of temperature, analogous to a similar measurement in [63]. Here, we observed that a zero-resistance state arises at T≈5.5K in the in-plane direction, but a finite resistance persists in the out-of-plane direction. ρ_c does drop significantly in this regime, and we believe this to be due to a slight misorientation of

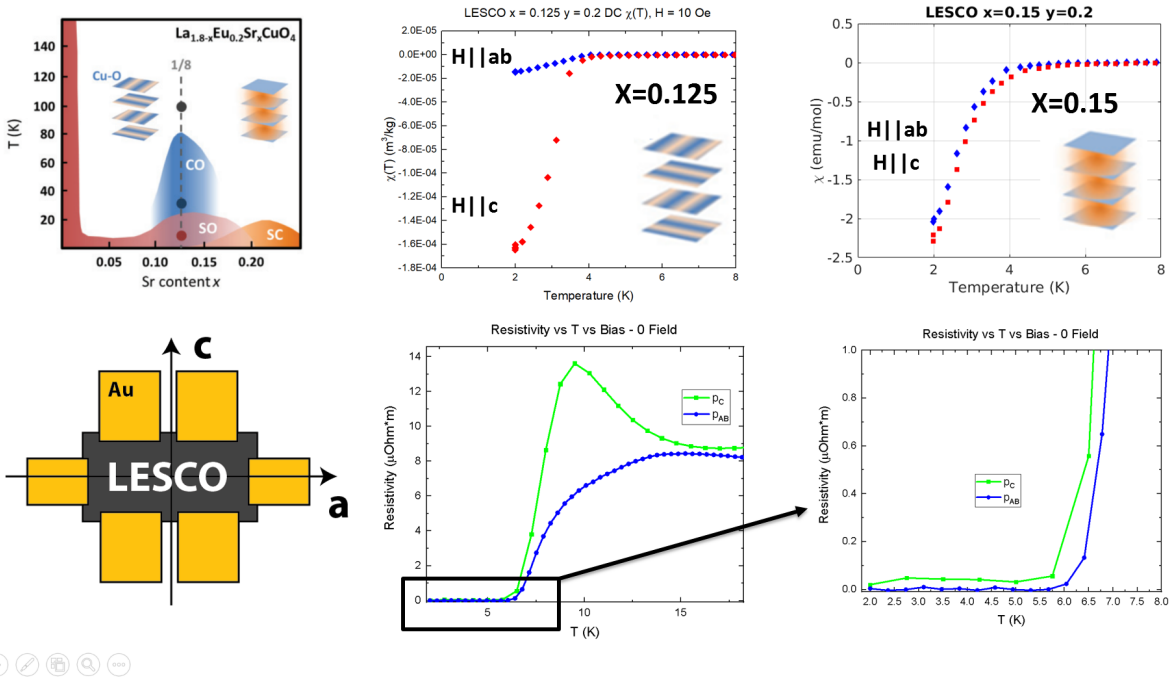

Figure 6.1: Top left: Phase diagram of LESCO from [110], showing onset of superconductivity, charge order and spin order. Top mid, top right: Susceptibility measurements of LESCO crystals at x=0.125 and x=0.15, respectively. Larger diamagnetism in the out-of-plane direction implies superconductivity is primarily taking place within the CuO_2 planes. In the 0.15 sample, the direction of the field no longer has an effect, indicating uniform superconductivity. Bottom left: Diagram of sample used for LESCO resistivity measurements. Choice of leads for 4-point measurement allows either ρ_{ab} or ρ_c to be measured. Bottom mid: Temperature dependence ρ_{ab} and ρ_c. In-plane ρ_{ab} begins dropping at higher T, and reaches approximately zero at T≈5.5K, while ρ_c increases, then drops and levels off to a finite value. Bottom right: Closer zoom of low temperature regime.

the LESCO crystal causing us to measure some partial in-plane transport. These measured anisotropies in susceptibility and resistivity between the in-plane and out-of-plane directions at low T indicate that LESCO appears to be a promising candidate for a system carrying superconductivity described by the pair-density wave state. Measuring the current-phase relation of a Josephson junction on this material near x=1/8 doping would then be likely to yield the characteristic $\sin(2\phi)$ harmonics we observed in this thesis, which would provide further confirmation of the PDW state in materials other than LBCO.

References

[1] Dirk van Delft and Peter Kes. The discovery of superconductivity. *Physics Today*, 63:38–43, 2010.

[2] Heike Onnes. The liquefaction of helium. *KNAW Proceedings*, 11:168–185, 1908.

[3] D. van Delft. The liquefaction of helium. *Europhysics News*, 39(6):23–25, November 2008.

[4] H. Kamerlingh Onnes. Further experiments with Liquid Helium. G. On the Electrical Resistance of Pure Metals, etc. VI. On the Sudden Change in the Rate at which the Resistance of Mercury Disappears. *KNAW Proceedings*, 14 II:818–812, 1911.

[5] W. Meissner and R. Ochsenfeld. Ein neuer Effekt bei Eintritt der Supraleitfhigkeit. *Naturwissenschaften*, 21:787–788, November 1933.

[6] J. Bardeen, L. N. Cooper, and J. R. Schrieffer. Microscopic Theory of Superconductivity. *Physical Review*, 106(1):162–164, April 1957.

[7] J. Bardeen, L. N. Cooper, and J. R. Schrieffer. Theory of Superconductivity. *Physical Review*, 108(5):1175–1204, December 1957.

[8] H. Frhlich. Theory of the Superconducting State. I. The Ground State at the Absolute Zero of Temperature. *Physical Review*, 79(5):845–856, September 1950.

[9] Leon N. Cooper. Bound Electron Pairs in a Degenerate Fermi Gas. *Physical Review*, 104(4):1189–1190, November 1956.

[10] V Ginzburg and L Landau. On the Theory of Superconductivity. *Zh. Eksp. Teor. Fiz.*, 20:1064–1082, 1950.

[11] Michael Marder. *Condensed Matter Physics*. John Wiiley & Sons, Inc, 2010.

[12] M Tinkham. *Introduction to Superconductivity*. Courier Dover Publications, second edition edition, 2012.

[13] L P Gor'kov. Microscopic Derivation of the Ginzburg-Landau Equations in the Theory of Superconductivity. *JETP*, 9(6):1364, 1959.

[14] A Abrikosov. On the Magnetic Properties of Superconductors of the Second Group. *JETP*, 5(6):1174, 1957.

[15] H. F. Hess, R. B. Robinson, R. C. Dynes, J. M. Valles, and J. V. Waszczak. Scanning-Tunneling-Microscope Observation of the Abrikosov Flux Lattice and the Density of States near and inside a Fluxoid. *Physical Review Letters*, 62(2):214–216, January 1989.

[16] J. N. Rjabinin and L. W. Shubnikow. Magnetic Properties and Critical Currents of Supra-conducting Alloys. *Nature*, 135(3415):581–582, April 1935.

[17] U Essmann and H Trauble. Direct Observation of Individual Flux Lines in Type II Superconductors. *Physics Letters,*, 24A:526, 1967.

[18] W. L. McMillan. Transition Temperature of Strong-Coupled Superconductors. *Physical Review*, 167(2):331–344, March 1968.

[19] J. G. Bednorz and K. A. Mller. Possible high Tc superconductivity in the BaLaCuO system. *Zeitschrift fr Physik B Condensed Matter*, 64(2):189–193, June 1986.

[20] M. K. Wu, J. R. Ashburn, C. J. Torng, P. H. Hor, R. L. Meng, L. Gao, Z. J. Huang, Y. Q. Wang, and C. W. Chu. Superconductivity at 93 K in a new mixed-phase Y-Ba-Cu-O compound system at ambient pressure. *Physical Review Letters*, 58(9):908–910, March 1987.

[21] Hiroshi Maeda, Yoshiaki Tanaka, Masao Fukutomi, and Toshihisa Asano. A New High-Tc Oxide Superconductor without a Rare Earth Element. *Japanese Journal of Applied Physics*, 27(2A):L209, February 1988.

[22] A. Schilling, M. Cantoni, J. D. Guo, and H. R. Ott. Superconductivity above 130 K in the HgBaCaCuO system. *Nature*, 363(6424):56, May 1993.

[23] A. P. Drozdov, P. P. Kong, V. S. Minkov, S. P. Besedin, M. A. Kuzovnikov, S. Mozaffari, L. Balicas, F. Balakirev, D. Graf, V. B. Prakapenka, E. Greenberg, D. A. Knyazev, M. Tkacz, and M. I. Eremets. Superconductivity at 250 K in lanthanum hydride under high pressures. *arXiv:1812.01561 [cond-mat]*, December 2018. arXiv: 1812.01561.

[24] Crystal Structures of Cuprate Superconductors. In *Physical Properties of High-Temperature Superconductors*, pages 101–130. John Wiley & Sons, Ltd, 2015.

[25] C. W. Chu, L. Z. Deng, and B. Lv. Hole-doped cuprate high temperature superconductors. *Physica C: Superconductivity and its Applications*, 514:290–313, July 2015.

[26] Louis Taillefer. Scattering and Pairing in Cuprate Superconductors. *Annual Review of Condensed Matter Physics*, 1(1):51–70, 2010.

[27] M. B. J. Meinders, H. Eskes, and G. A. Sawatzky. Spectral-weight transfer: Breakdown of low-energy-scale sum rules in correlated systems. *Physical Review B*, 48(6):3916–3926, August 1993.

[28] Patrick A. Lee, Naoto Nagaosa, and Xiao-Gang Wen. Doping a Mott insulator: Physics of high-temperature superconductivity. *Reviews of Modern Physics*, 78(1):17–85, January 2006.

[29] Sandeep Pathak, Vijay B. Shenoy, Mohit Randeria, and Nandini Trivedi. Competition between Antiferromagnetic and Superconducting States, Electron-Hole Doping Asymmetry, and Fermi-Surface Topology in High Temperature Superconductors. *Physical Review Letters*, 102(2):027002, January 2009.

[30] N. P. Armitage, P. Fournier, and R. L. Greene. Progress and perspectives on electron-doped cuprates. *Reviews of Modern Physics*, 82(3):2421–2487, September 2010.

[31] C Renner and B Revaz. Pseudogap Precursor of the Superconducting Gap in Under- and Overdoped Bi2sr2cacu2o81d. *Physical Review Letters*, 80(1):4, 1998.

[32] K Ishida, K Yoshida, T Mito, Y Tokunaga, Y Kitaoka, K Asayama, Y Nakayama, J Shimoyama, and K Kishio. Pseudogap behavior in single-crystal Bi2sr2cacu2o8 probed by Cu NMR. page 4.

[33] M. R. Norman, D. Pines, and C. Kallin. The pseudogap: friend or foe of high T_c ? *Advances in Physics*, 54(8):715–733, December 2005.

[34] L. C. Hebel and C. P. Slichter. Nuclear Spin Relaxation in Normal and Superconducting Aluminum. *Physical Review*, 113(6):1504–1519, March 1959.

[35] Kei Yosida. Paramagnetic Susceptibility in Superconductors. *Physical Review*, 110(3):769–770, May 1958.

[36] Yayu Wang, Lu Li, and N. P. Ong. Nernst effect in high-Tc superconductors. *Physical Review B*, 73(2):024510, January 2006.

[37] J. E. Hoffman, E. W. Hudson, K. M. Lang, V. Madhavan, H. Eisaki, S. Uchida, and J. C. Davis. A Four Unit Cell Periodic Pattern of Quasi-Particle States Surrounding Vortex Cores in Bi2sr2cacu2o8+. *Science*, 295(5554):466–469, January 2002.

[38] W. D. Wise, M. C. Boyer, Kamalesh Chatterjee, Takeshi Kondo, T. Takeuchi, H. Ikuta, Yayu Wang, and E. W. Hudson. Charge-density-wave origin of cuprate checkerboard visualized by scanning tunnelling microscopy. *Nature Physics*, 4(9):696–699, September 2008.

[39] Kyle M. Shen, F. Ronning, D. H. Lu, F. Baumberger, N. J. C. Ingle, W. S. Lee, W. Meevasana, Y. Kohsaka, M. Azuma, M. Takano, H. Takagi, and Z.-X. Shen. Nodal Quasiparticles and Antinodal Charge Ordering in Ca2-xNaxCuO2cl2. *Science*, 307(5711):901–904, February 2005.

[40] J. Chang, E. Blackburn, A. T. Holmes, N. B. Christensen, J. Larsen, J. Mesot, Ruixing Liang, D. A. Bonn, W. N. Hardy, A. Watenphul, M. v. Zimmermann, E. M. Forgan, and S. M. Hayden. Direct observation of competition between superconductivity and charge density wave order in YBa2cu3o6.67. *Nature Physics*, 8(12):871–876, December 2012.

[41] Carsten Putzke, Jake Ayres, Jonathan Buhot, Salvatore Licciardello, Nigel E. Hussey, Sven Friedemann, and Antony Carrington. Charge Order and Superconductivity in Underdoped YBa 2 Cu 3 O 7 under Pressure. *Physical Review Letters*, 120(11), March 2018.

[42] O. Cyr-Choinire, G. Grissonnanche, S. Badoux, J. Day, D. A. Bonn, W. N. Hardy, R. Liang, N. Doiron-Leyraud, and Louis Taillefer. Two types of nematicity in the phase diagram of the cuprate superconductor YBa2cu3oy. *Physical Review B*, 92(22):224502, December 2015.

[43] Emanuel Maxwell. Isotope Effect in the Superconductivity of Mercury. *Physical Review*, 78(4):477–477, May 1950.

[44] B. Batlogg, R. J. Cava, A. Jayaraman, R. B. van Dover, G. A. Kourouklis, S. Sunshine, D. W. Murphy, L. W. Rupp, H. S. Chen, A. White, K. T. Short, A. M. Mujsce, and E. A. Rietman. Isotope Effect in the High- T c Superconductors Ba 2 Y Cu 3 O 7 and Ba 2 Eu Cu 3 O 7. *Physical Review Letters*, 58(22):2333–2336, June 1987.

[45] Ivan Parinov. *Microstructure and Properties of High-Temperature Superconductors*. Springer-Verlag, Berlin Heidelberg, 2 edition, 2012.

[46] J P Franck. Experimental investigations of the isotope effect in high T_c superconductors. *Physica Scripta*, T66:220–224, January 1996.

[47] H. Ding, M. R. Norman, J. C. Campuzano, M. Randeria, A. F. Bellman, T. Yokoya, T. Takahashi, T. Mochiku, and K. Kadowaki. Angle-resolved photoemission spectroscopy study of the superconducting gap anisotropy in Bi 2 Sr 2 Ca Cu 2 O 8 + x. *Physical Review B*, 54(14):R9678–R9681, October 1996.

[48] C. C. Tsuei, J. R. Kirtley, C. C. Chi, Lock See Yu-Jahnes, A. Gupta, T. Shaw, J. Z. Sun, and M. B. Ketchen. Pairing Symmetry and Flux Quantization in a Tricrystal Superconducting Ring of Y Ba 2 Cu 3 O 7 . *Physical Review Letters*, 73(4):593–596, July 1994.

[49] D. J. Van Harlingen. Phase-sensitive tests of the symmetry of the pairing state in the high-temperature superconductorsEvidence for d x 2 y 2 symmetry. *Reviews of Modern Physics*, 67(2):515–535, April 1995.

[50] B. I. Spivak and S. A. Kivelson. Negative local superfluid densities: The difference between dirty superconductors and dirty Bose liquids. *Physical Review B*, 43(4):3740–3743, February 1991.

[51] Manfred Sigrist and T. M. Rice. Paramagnetic Effect in High T c Superconductors -A Hint for d-Wave Superconductivity. *Journal of the Physical Society of Japan*, 61(12):4283–4286, December 1992.

[52] B. Spivak, P. Oreto, and S. A. Kivelson. Theory of quantum metal to superconductor transitions in highly conducting systems. *Physical Review B*, 77(21):214523, June 2008.

[53] Brian M. Andersen, P. J. Hirschfeld, Arno P. Kampf, and Markus Schmid. Disorder-Induced Static Antiferromagnetism in Cuprate Superconductors. *Physical Review Letters*, 99(14):147002, October 2007.

[54] T. R. Lemberger, I. Hetel, A. Tsukada, M. Naito, and M. Randeria. Superconductor-to-metal quantum phase transition in overdoped La 2 x Sr x CuO 4. *Physical Review B*, 83(14), April 2011.

[55] M. Hcker, M. v. Zimmermann, G. D. Gu, Z. J. Xu, J. S. Wen, Guangyong Xu, H. J. Kang, A. Zheludev, and J. M. Tranquada. Stripe order in superconducting La2-xBaxCuO4 0.095<x<0.155). *Physical Review B*, 83(10):104506, March 2011.

[56] A. R. Moodenbaugh, Youwen Xu, M. Suenaga, T. J. Folkerts, and R. N. Shelton. Superconducting properties of La2-xBaxCuO4. *Physical Review B*, 38(7):4596–4600, September 1988.

[57] V. Sachan, D. J. Buttrey, J. M. Tranquada, J. E. Lorenzo, and G. Shirane. Charge and spin ordering in La 2 x Sr x NiO 4.00 with x =0.135 and 0.20. *Physical Review B*, 51(18):12742–12746, May 1995.

[58] P. Abbamonte, A. Rusydi, S. Smadici, G. D. Gu, G. A. Sawatzky, and D. L. Feng. Spatially modulated 'Mottness' in $La_{2-x}Ba_xCuO_4$. *Nature Physics*, 1(3):155–158, December 2005.

[59] M. Hcker, N. B. Christensen, A. T. Holmes, E. Blackburn, E. M. Forgan, Ruixing Liang, D. A. Bonn, W. N. Hardy, O. Gutowski, M. v. Zimmermann, S. M. Hayden, and J. Chang. Competing charge, spin, and superconducting orders in underdoped YBa 2 Cu 3 O y. *Physical Review B*, 90(5), August 2014.

[60] J. M. Tranquada, B. J. Sternlieb, J. D. Axe, Y. Nakamura, and S. Uchida. Evidence for stripe correlations of spins and holes in copper oxide superconductors. *Nature*, 375(6532):561–563, June 1995.

[61] J. M. Tranquada, D. J. Buttrey, V. Sachan, and J. E. Lorenzo. Simultaneous Ordering of Holes and Spins in La 2 Ni O 4.125. *Physical Review Letters*, 73(7):1003–1006, August 1994.

[62] Jrg Fink, Enrico Schierle, Eugen Weschke, Jochen Geck, David Hawthorn, Viktor Soltwisch, Hiroki Wadati, Hsueh-Hung Wu, Hermann A. Drr, Nadja Wizent, Bernd Bchner, and George A. Sawatzky. Charge ordering in La1.8-xEu0.2srxcuo4 studied by resonant soft x-ray diffraction. *Physical Review B*, 79(10):100502, March 2009.

[63] Q. Li, M. Hcker, G. D. Gu, A. M. Tsvelik, and J. M. Tranquada. Two-Dimensional Superconducting Fluctuations in Stripe-Ordered La 1.875 Ba 0.125 CuO 4. *Physical Review Letters*, 99(6), August 2007.

[64] Eduardo Fradkin, Steven A. Kivelson, and John M. Tranquada. Colloquium: Theory of intertwined orders in high temperature superconductors. *Reviews of Modern Physics*, 87(2):457–482, May 2015.

[65] E. Berg, E. Fradkin, E.-A. Kim, S. A. Kivelson, V. Oganesyan, J. M. Tranquada, and S. C. Zhang. Dynamical Layer Decoupling in a Stripe-Ordered High-${T}_{c}$ Superconductor. *Physical Review Letters*, 99(12):127003, September 2007.

[66] Masaki Fujita, Haruhiro Hiraka, Masaaki Matsuda, Masato Matsuura, John M. Tranquada, Shuichi Wakimoto, Guangyong Xu, and Kazuyoshi Yamada. Progress in Neutron Scattering Studies of Spin Excitations in High-Tc Cuprates. *Journal of the Physical Society of Japan*, 81(1):011007, December 2011.

[67] Erez Berg, Eduardo Fradkin, and Steven A. Kivelson. Charge-4e superconductivity from pair-density-wave order in certain high-temperature superconductors. *Nature Physics*, 5(11):830–833, November 2009.

[68] Erez Berg, Eduardo Fradkin, and Steven A. Kivelson. Theory of the striped superconductor. *Physical Review B*, 79(6):064515, February 2009.

[69] A. Himeda, T. Kato, and M. Ogata. Stripe States with Spatially Oscillating d -Wave Superconductivity in the Two-Dimensional t t J Model. *Physical Review Letters*, 88(11), February 2002.

[70] S. Rajasekaran, J. Okamoto, L. Mathey, M. Fechner, V. Thampy, G. D. Gu, and A. Cavalleri. Probing optically silent superfluid stripes in cuprates. *Science*, 359(6375):575–579, February 2018.

[71] M. H. Hamidian, S. D. Edkins, Sang Hyun Joo, A. Kostin, H. Eisaki, S. Uchida, M. J. Lawler, E.-A. Kim, A. P. Mackenzie, K. Fujita, Jinho Lee, and J. C. Samus Davis. Detection of a Cooper-pair density wave in Bi2sr2cacu2o8+x. *Nature*, 532(7599):343–347, April 2016.

[72] B. D. Josephson. Possible new effects in superconductive tunnelling. *Physics Letters*, 1(7):251–253, July 1962.

[73] M Beasley. Notes on the Ginzburg-Landau Theory, August 2009.

[74] Alex I. Braginski and John Clarke. Introduction. In *The SQUID Handbook*, pages 1–28. John Wiley & Sons, Ltd, 2005.

[75] D. A. Wollman, D. J. Van Harlingen, J. Giapintzakis, and D. M. Ginsberg. Evidence for d x 2 y 2 Pairing from the Magnetic Field Modulation of Y Ba 2 Cu 3 O 7 -Pb Josephson Junctions. *Physical Review Letters*, 74(5):797–800, January 1995.

[76] A. A. Golubov, M. Yu. Kupriyanov, and E. Ilichev. The current-phase relation in Josephson junctions. *Reviews of Modern Physics*, 76(2):411–469, April 2004.

[77] H. Hilgenkamp and J. Mannhart. Grain boundaries in high- T c superconductors. *Reviews of Modern Physics*, 74(2):485–549, May 2002.

[78] E. Il'ichev, M. Grajcar, R. Hlubina, R. P. J. IJsselsteijn, H. E. Hoenig, H.-G. Meyer, A. Golubov, M. H. S. Amin, A. M. Zagoskin, A. N. Omelyanchouk, and M. Yu. Kupriyanov. Degenerate Ground State in a Mesoscopic YBa 2 Cu 3 O 7 x Grain Boundary Josephson Junction. *Physical Review Letters*, 86(23):5369–5372, June 2001.

[79] V. V. Ryazanov, V. A. Oboznov, A. Yu. Rusanov, A. V. Veretennikov, A. A. Golubov, and J. Aarts. Coupling of Two Superconductors through a Ferromagnet: Evidence for a Junction. *Physical Review Letters*, 86(11):2427–2430, March 2001.

[80] S. M. Frolov, D. J. Van Harlingen, V. V. Bolginov, V. A. Oboznov, and V. V. Ryazanov. Josephson interferometry and Shapiro step measurements of superconductor-ferromagnet-superconductor 0 junctions. *Physical Review B*, 74(2), July 2006.

[81] M.J.A. Stoutimore, A.N. Rossolenko, V.V. Bolginov, V.A. Oboznov, A.Y. Rusanov, D.S. Baranov, N. Pugach, S.M. Frolov, V.V. Ryazanov, and D.J. Van Harlingen. Second-Harmonic Current-Phase Relation in Josephson Junctions with Ferromagnetic Barriers. *Physical Review Letters*, 121(17), October 2018.

[82] A. Buzdin and A. E. Koshelev. Periodic alternating 0- and -junction structures as realization of -Josephson junctions. *Physical Review B*, 67(22), June 2003.

[83] M. Moshe and R. G. Mints. Shapiro steps in Josephson junctions with alternating critical current density. *Physical Review B*, 76(5), August 2007.

[84] L. D. Jackel, R. A. Buhrman, and W. W. Webb. Direct measurement of current-phase relations in superconducting weak links. *Physical Review B*, 10(7):2782–2785, October 1974.

[85] J.R. Waldram and J.M. Lumley. Direct measurements of the current-phase relation in superconducting weak links. *Revue de Physique Appliquee*, 10(1):7–10, 1975.

[86] S. M. Frolov, D. J. Van Harlingen, V. A. Oboznov, V. V. Bolginov, and V. V. Ryazanov. Measurement of the current-phase relation of superconductor/ferromagnet/superconductor Josephson junctions. *Physical Review B*, 70(14), October 2004.

[87] C. D. English, D. R. Hamilton, C. Chialvo, I. C. Moraru, N. Mason, and D. J. Van Harlingen. Observation of nonsinusoidal current-phase relation in graphene Josephson junctions. *Physical Review B*, 94(11), September 2016.

[88] SQUID Application Note 1052-202: Coupling Magnetic Signals to a SQUID Amplifier, October 2001.

[89] G. Nanda, J. L. Aguilera-Servin, P. Rakyta, A. Kormnyos, R. Kleiner, D. Koelle, K. Watanabe, T. Taniguchi, L. M. K. Vandersypen, and S. Goswami. Current-Phase Relation of Ballistic Graphene Josephson Junctions. *Nano Letters*, 17(6):3396–3401, June 2017.

[90] M. L. Della Rocca, M. Chauvin, B. Huard, H. Pothier, D. Esteve, and C. Urbina. Measurement of the Current-Phase Relation of Superconducting Atomic Contacts. *Physical Review Letters*, 99(12):127005, September 2007.

[91] Floating Zone Growth of Oxides and Metallic Alloys. In *Handbook of Crystal Growth*, pages 281–329. Elsevier, 2015.

[92] Multiwire Laboratories The Real-Time Laue Camera Company.

[93] R.E. Smallman and A.H.W. Ngan. Characterization and Analysis. In *Modern Physical Metallurgy*, pages 159–250. Elsevier, 2014.

[94] David Bailey, P Krieger, Jason Harlow, Derek Paul, and John Pitre. Laue Back-Reflection of X-Rays, 2016.

[95] T. Hanaguri, T. Fukase, T. Goto, and Y. Iwabuchi. Ultrasonic Studies in La2-x(Ba,Sr)xCuO4. In Yasuhiro Iye and Hiroshi Yasuoka, editors, *The Physics and Chemistry of Oxide Superconductors*, Springer Proceedings in Physics, pages 217–220. Springer Berlin Heidelberg, 1992.

[96] Sanat K. Chatterjee. *Crystallography and the World of Symmetry*. Springer Series in Materials Science. Springer-Verlag, Berlin Heidelberg, 2008.

[97] Richard L. Kurtz, Roger Stockbauer, Theodore E. Madey, Donald Mueller, Arnold Shih, and Louis Toth. Initial stages of degradation of superconductor surfaces: O 2 , H 2 O, CO 2 , and CO chemisorption on La 2 x Sr x CuO 4. *Physical Review B*, 37(13):7936–7939, May 1988.

[98] J. W. Ekin, T. M. Larson, N. F. Bergren, A. J. Nelson, A. B. Swartzlander, L. L. Kazmerski, A. J. Panson, and B. A. Blankenship. High T_c superconductor/noblemetal contacts with surface resistivities in the 10^{10} cm ^{2} range. *Applied Physics Letters*, 52(21):1819–1821, May 1988.

[99] D. R. Lundy, L. J. Swartzendruber, and L. H. Bennett. A Brief Review of Recent Superconductivity Research at NIST. *Journal of Research of the National Institute of Standards and Technology*, 94(3):147–178, 1989.

[100] Joe Hilliard. *Conductivity and Interferometry Experiments on YBCO/PB Ramp-Edge Josephson Junctions*. PhD thesis, University of Illinois at Urbana-Champaign, 2001.

[101] T. Thomson. Magnetic properties of metallic thin films. In *Metallic Films for Electronic, Optical and Magnetic Applications*, pages 454–546. Elsevier, 2014.

[102] Z Guguchia, A Maisuradze, G Ghambashidze, R Khasanov, A Shengelaya, and H Keller. Tuning the static spin-stripe phase and superconductivity in La $_{2\,x}$ Ba $_{x}$ CuO $_{4}$ ($x = 1/8$) by hydrostatic pressure. *New Journal of Physics*, 15(9):093005, September 2013.

[103] Milan D. Fiske. Temperature and Magnetic Field Dependences of the Josephson Tunneling Current. *Reviews of Modern Physics*, 36(1):221–222, January 1964.

[104] P W Forder. A useful simplification of the resistively shunted junction model of a Josephson weak-link. *Journal of Physics D: Applied Physics*, 10(11):1413–1436, August 1977.

[105] Vinay Ambegaokar and Alexis Baratoff. Tunneling Between Superconductors. *Physical Review Letters*, 10(11):486–489, June 1963.

[106] T. P. Croft, C. Lester, M. S. Senn, A. Bombardi, and S. M. Hayden. Charge density wave fluctuations in La 2 x Sr x CuO 4 and their competition with superconductivity. *Physical Review B*, 89(22):224513, June 2014.

[107] William Neils. *Josephson Interferometry Measurements in High-Tc Grain Boundary Junctions*. PhD thesis, University of Illinois at Urbana-Champaign, 2002.

[108] Manfred Sigrist and T. M. Rice. Unusual paramagnetic phenomena in granular high-temperature superconductors—A consequence of d- wave pairing? *Reviews of Modern Physics*, 67(2):503–513, April 1995.

[109] Yoichi Tanabe, Tadashi Adachi, Takashi Noji, and Yoji Koike. Superconducting Volume Fraction in Overdoped Regime of La $_{2-\,x}$ Sr $_{x}$ CuO $_{4}$: Implication for Phase Separation from Magnetic-Susceptibility Measurement. *Journal of the Physical Society of Japan*, 74(11):2893–2896, November 2005.

[110] C. R. Hunt, D. Nicoletti, S. Kaiser, T. Takayama, H. Takagi, and A. Cavalleri. Two distinct kinetic regimes for the relaxation of light-induced superconductivity in L a 1.675 E u 0.2 S r 0.125 Cu O 4. *Physical Review B*, 91(2):020505, January 2015.

Vita

David Hamilton was born in Misawa, Japan to Daniel and Rochelle Hamilton, and grew up in Santee, CA. In 2007, he moved north to study at the University of California, Berkeley, completing a Bachelor of Arts in Physics in 2011 with a minor in Music. While at Berkeley, David became editor-in-chief of the Berkeley Political Review, played mellophone with University of California Marching Band, and conducted research at the Space Sciences Laboratory examining magnetic reconnection at the earth's magnetopause.

In 2011, David enrolled at the University of Illinois at Urbana-Champaign to study experimental condensed matter physics. David began research with Dale Van Harlingen's group during his first year, initially working with fellow student Christopher English to examine the current-phase relation of graphene Josephson junctions, later branching out into the work described in this thesis. In February, David married Christine Peralta, a doctoral candidate at the University of Illinois History department. They live together with their two dogs. Later this year, David will move to the Portland area to begin a position at Intel Corporation.